The Dissertation Committee for Zachary Moorhead-Rosenberg Certifies that this is the approved version of the following dissertation:

Magnetic, Electronic, and Electrochemical Properties of High-voltage Spinel Cathodes for Lithium-ion Batteries

Committee:

Arumugam Manthiram, Supervisor

John B. Goodenough

Jianshi Zhou

Nicole A. Benedek

Gyeong S. Hwang

Magnetic, Electronic, and Electrochemical Properties of High-voltage Spinel Cathodes for Lithium-ion Batteries

by

Zachary Moorhead-Rosenberg, B.S. M.E.

Dissertation

Presented to the Faculty of the Graduate School of

The University of Texas at Austin

in Partial Fulfillment

of the Requirements

for the Degree of

Doctor of Philosophy

The University of Texas at Austin

May 2015

Acknowledgements

I begin by thanking every member of the Manthiram group at the University of Texas at Austin that I have had the pleasure to work with. I would especially like to thank those lab members whom I was able to learn from and work closely with: Dr. Katherine Chemelewski, Dr. Dongwook Shin, Dr. Eunsung Lee, Dr. Jinguang Cheng, Dr. Luke Marshall, Dr. Katherine Harrison, Travis Turner, Dr. "Jack" Kan, Sheng-Heng Chung, and Eric Alcorn. I would also like to thank Dr. Ahsfia Huq for help with neutron diffraction studies at the SNS at the Oak Ridge National Laboratory. Without them, none of my work would have been possible. Katherine Harrison, Sheng-Heng, and Travis contributed valuable information for chapter 7, as did Eric Allcorn for chapter 6. I would also like to specifically thank my office mates James Knight and Dr. Matt West for providing lots of wonderful conversation over the past few years.

Dr. Manthiram has been everything I could have asked for in an advisor; his support and guidance along with his inclination to grant me autonomy were instrumental in shaping me as a graduate student and as a person. For that, I am immensely grateful. I would also like to thank all the members of my dissertation committee, whom, coincidentally, are all members of the Materials Interdisciplinary Research Team (MIRT) at UT which funded my research: Dr. John B. Goodeough, Dr. Jianshi Zhou, Dr. Nicole Benedek, and Dr. Gyeong Hwang. The help and assistance provided by Dr. Zhou and Dr. Goodenough enabled many aspects of my research, including most of the physical properties measurements of my materials.

Financial support was provided through the MIRT grant by the National Science Foundation. I would also like to acknowledge the Cockrell School of Engineering for

granting me an Engineering Doctoral Fellowship. I am eternally grateful to the University of Texas for providing PhD candidates with such strong financial assistance.

Through the MIRT grant, I was also able to take part in several outreach opportunities and worked with several organizations, including Graduates Linked with Undergraduates in Engineering, the Women in Engineering Program, and the Ann Richards School. These experiences opened my eyes as to how important outreach is for the science community and I had a great time teaching and learning. I'd like to thank other MRS members Michael Klein and Alex Rettie for sharing in these experiences as well as the MIRT staff Sarah Campbell and Kristie Aletky for guiding the outreach program.

Finally, I would like to thank my wonderful family for all the love and support they have shown me, not just for the past four years of graduate school, but for my entire life. My parents are the two kindest and wisest people I will ever know and without them I would not be the person I am today.

Magnetic, Electronic, and Electrochemical Properties of High-voltage Spinel Cathodes for Lithium-ion Batteries

Zachary Moorhead-Rosenberg, Ph.D.

The University of Texas at Austin, 2015

Supervisor: Arumugam Manthiram

Lithium-ion technology has revolutionized the electronics and electric vehicle industry in the past two decades. First commercialized by Sony in 1991, the lithium-ion battery is composed of three main components: (i) the cathode, (ii) the anode, and (iii) the electrolyte. Graphitic carbon remains the most widely used anode material due to its low voltage vs. the Li/Li+ redox couple and high specific capacity. However, there are several popular cathode materials, including layered oxides, spinel oxides, and polyanion materials.

In an effort to increase the energy density of lithium-ion batteries, much focus is given to improving the gravimetric charge capacity and the overall cell voltage. The latter must be accomplished by employing high-voltage cathodes, the most promising of which is the lithium manganese nickel oxide spinel with a specific capacity of 146 mAh/g and a redox voltage of 4.7 V vs. Li/Li+. However, there are still several problems with this material that must be understood and overcome in order to develop high-voltage spinel as a viable commercial cathode.

Physical property measurements can reveal the underlying electronic and atomic interactions in the solid in order to better understand high-voltage spinel and its odd behavior. Novel magnetic techniques have been developed, which reliably indicate the

degree of Mn-Ni ordering and quantitative determination of the concentration of the Mn^{3+} ion. Measurements of several physical properties as a function of lithium content were also undertaken to determine the effects of Mn-Ni ordering on the electronic conductivity and the importance of electron-ion interactions.

In addition to understanding the physical properties of high voltage spinel, the understanding of the solid state chemistry and unique structure was utilized to realize a new full cell construction technique. The spinel structure offers a unique way to deal with first cycle irreversible capacity loss in full cells stemming from solid-electrolyte interphase (SEI) layer growth on the anode surface. To that end, a novel microwave-assisted chemical lithiation process was developed using non-toxic and air-stable chemicals. New composite anode chemistry was combined with a pre-lithiated spinel cathode to demonstrate the feasibility of this approach to realizing practical next-generation Li-ion cells.

Table of Contents

List of Tables

List of Figures

Chapter 1: Introduction

1.1 Motivation

The proliferation of portable electronic devices in the last few decades has motivated scientists to develop denser rechargeable energy storage systems. The rechargeable lead-acid, nickel-cadmium, and nickel-metal-hydride batteries have been surpassed by lithium-ion chemistry as the superior rechargeable cell due to its high energy density, low self-discharge, and long usable lifetime. Production costs are higher but the performance advantages are well worth it in many applications.[1]

The mounting global energy crisis has led to an increased interest in utilizing lithium-ion batteries for larger scale applications, namely electric vehicles and stationary energy storage for intermittent power sources like solar and wind.[2] The challenges associated with lowering the cost, improving energy density (gravimetric and volumetric), and increasing cell lifetime are immense, and have spawned a concentrated research effort to meet these objectives.[3,4]

1.2 Lithium-ion Cells

The rechargeable electrochemical cell consists of two electrodes (anode and cathode) that have different chemical potentials, μ, when placed in a conductive electrolyte; the difference in chemical potential produces a voltage, V, which can drive electrons through an external circuit to do useful work. Free electrons are generated at the anode via oxidative chemical reactions and consumed at the cathode via a reduction reaction. Highly reversible chemical reactions are necessary to ensure rechargeability.

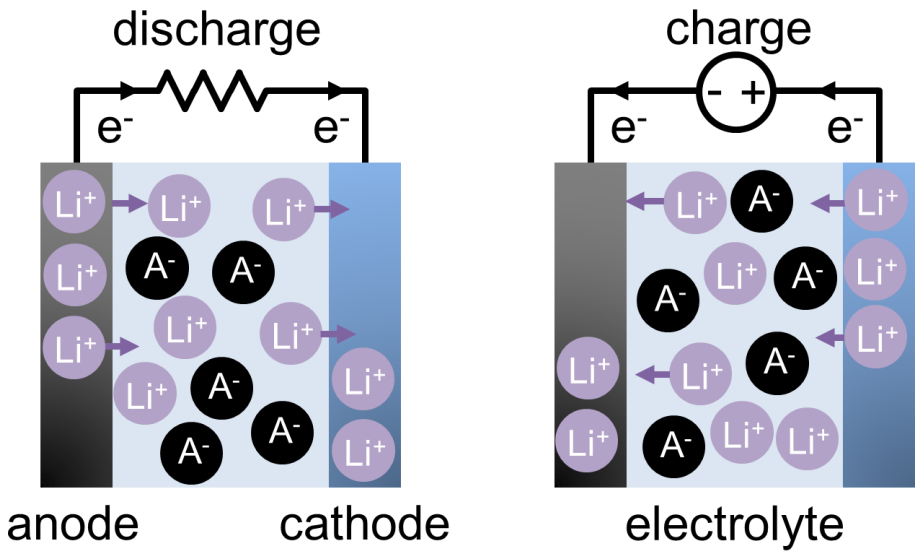

Figure 1.1 Schematic of lithium-ion cell operation.

Lithium-ion batteries offer higher energy density than other rechargeable cells such as lead-acid, NiCd, and NiMH, and provides energy by insertion and de-insertion of lithium ions into host materials. it is common to refer to lithium-ion as a "rocking-chair" cell.[5] A schematic of the discharge and charge process for a lithium-ion cell is shown in Figure 1.1. The non-aqueous electrolyte is essential as it allows for a higher operating voltage than aqueous cells; the organic carbonates used as solvents have a wide bandgap between the highest occupied molecular orbital (HOMO) and the lowest unoccupied molecular orbital (LUMO), so the voltage required to decompose the molecules is high.[6] Lithium insertion and extraction from host structures is a key element to the lithium-ion cell's long lifetime as these reactions are highly reversible and result in low volume expansion.[7] Electrode materials ideally must possess good electronic and ionic conductivity as well as good structural stability during charge/discharge.[8]

The three most successful lithium-ion cathode materials can be grouped into three crystal structures: (i) layered, (ii) spinel, and (iii) olivine.[9] Layered and spinel cathodes

are almost exclusively transition-metal oxides, although S[10] and F[11] anion doping has been explored, while olivine cathodes contain polyanions such as PO_4. The prototypical crystals for each system are: $LiCoO_2$,[12] $LiMn_2O_4$,[13] and $LiFePO_4$,[14] respectively. They all have very good reversibility, or cyclability, but each cathode has certain advantages and disadvantages, which make cathode selection application dependent. For instance, layered oxide has the best energy density but the raw materials cost for Co and Ni increase the overall cost of the battery.[1] $LiMn_2O_4$ is less expensive than the others because of raw materials and processing costs, but has a lower gravimetric energy density.

The anode material ubiquitous to almost all commercialized lithium-ion cells is graphite. Graphite offers excellent practical reversible capacity very close to the theoretical capacity of 372 mAh g^{-1} and a low potential vs. Li/Li^+, resulting in a high overall cell voltage.[15] Graphite operates above the LUMO of common electrolytes, forming a stable solid-electrolyte interphase (SEI) layer. This SEI layer blocks further decomposition of the electrolyte or the graphite[16] in a manner analogous to the protective layer formed by aluminum oxide on aluminum metal, preventing Al from rusting.

Nevertheless, demand still exists to develop new anode materials with higher capacity or better rate capability. Currently, silicon-based nanostructures are being intensely pursued to replace graphite in many applications.[17–19] Other alternative anodes such as $Li_4Ti_5O_{12}$ (LTO)[20] spinel offer excellent rate capability[21] and chemical stability but with higher cost and lower energy density.

1.3 Spinel Cathodes for Lithium-Ion Cells

The $LiMn_2O_4$ crystal structure is shown below in Figure 1.2. It is characterized by a cubic unit cell with *Fd*-3*m* symmetry and face-centered cubic (FCC) oxygen sub-lattice.

Mn ions reside in octahedral sites and Li ions in tetrahedral sites. These lithium ions are removed upon charge to produce λ-MnO_2, which maintains the *Fd*-3*m* cubic structure.

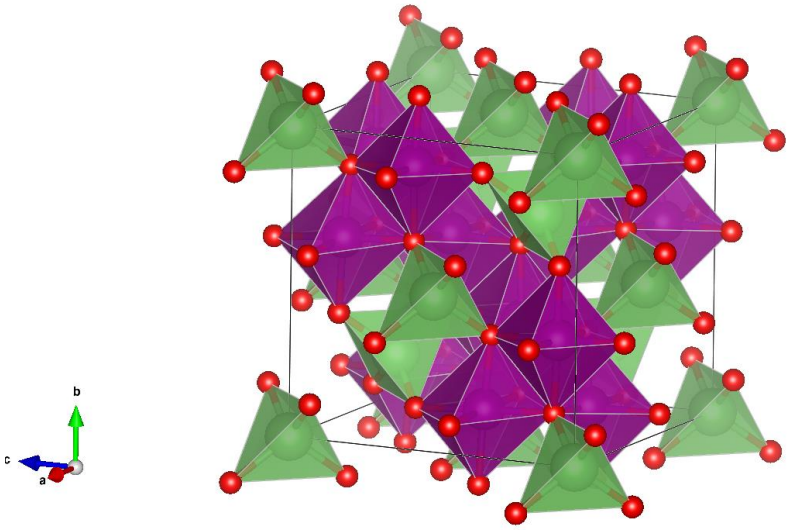

Figure 1.2 $LiMn_2O_4$ unit cell.

Excess lithium ions can also be inserted into the unoccupied octahedral sites, resulting in the reduction of Mn^{4+} to Mn^{3+}. In six-fold coordination with oxygen, Mn^{3+} is a strong Jahn-Teller ion due to the lone electron in twofold degenerate Mn:e_g orbitals (the e_g orbitals are empty in Mn^{4+}). The cooperative Jahn-Teller distortion of the unit cell caused by the Mn^{3+} ions results in a tetragonal unit cell with $c/a > 1$. This distortion, coupled with a traveling two-phase interface during lithium insertion/extraction, produces mechanical stresses which fracture the spinel particles and result in crumbling of the cathode and loss of electrical contact.[22] This kind of cracking has been shown to produce shockwaves throughout the cathode.[23] Therefore, electrochemical cycling of spinel is thus limited to compositions between $LiMn_2O_4$ and λ-MnO_2. However, the insertion of lithium into the empty octahedral sites can be irreversibly utilized as a lithium reservoir[24] to combat first-cycle irreversibility of next-generation alloy anode materials.[25] Chapter 7 explores this concept in depth.

1.4 HIGH-VOLTAGE SPINEL

$LiMn_2O_4$ cycles at 4.0 V vs. Li/Li^+. This corresponds to the $Mn^{3+/4+}$ redox couple, which lies in a metal 3d band at a substantial energy above the O:2p band. The characteristic voltage of the cathode can be increased by lowering the energy of the metal 3d band, concomitantly increasing the voltage difference between the cathode redox couple and the anode (and Li/Li^+) couple. Increased cell voltage results in higher energy density at the cost of increased side reactions, which occur between the cathode and the electrolyte. These side reactions deplete the electrolyte and the lithium salt, leading to decreased coulombic efficiency and significant energy density fade over time. The development of new, high-voltage capable electrolytes is a major research area, and progress is being made in ionic liquids and fluorinated organic electrolytes.

One way to increase the cell voltage is to substitute another transition metal for Mn, such as Fe, Co, or Ni. Ni-substituted spinel has been the most successful in terms of performance due to the $Ni^{2+/3+/4+}$ redox couples.[26] Up to 0.5 Ni per formula unit can be substituted for Mn, yielding the chemical formula $LiMn_{1.5}{}^{4+}Ni_{0.5}{}^{2+}O_4$. Further Ni substitution is not possible, and results in a nickel-rich $Li_xNi_{1-x}O$ disordered rocksalt secondary phase during synthesis.[27] By substituting Ni for Mn, the Mn:e_g band is depleted in order to donate electrons to the lower energy Ni:e_g band, lowering the Fermi energy and increasing the cell voltage. The charge/discharge voltage of $LiMn_{1.5}Ni_{0.5}O_4$ is 4.7 V, approximately 700 mV higher than that of $LiMn_2O_4$. For this reason, $LiMn_{1.5}Ni_{0.5}O_4$ is also called "high-voltage spinel" or "5V spinel" (even though the actual voltage is just shy of 5V vs. Li/Li^+). The 700 mV advantage over $LiMn_2O_4$ gives high-voltage spinel excellent energy density - comparable to layered oxides but with less Ni and Li precursor materials, so the cost per kWh is lower. This makes it an attractive

candidate for next generation lithium-ion cells although several practical challenges must be overcome if it is ever to be commercialized.[28]

A typical high-voltage spinel discharge curve, which displays cell voltage (V) vs. gravimetric charge capacity (mAh g^{-1}), is depicted in Figure 1.3. In this diagram, the voltage plateaus corresponding to the reduction of the transition metal-ions are indicated by dashed lines.

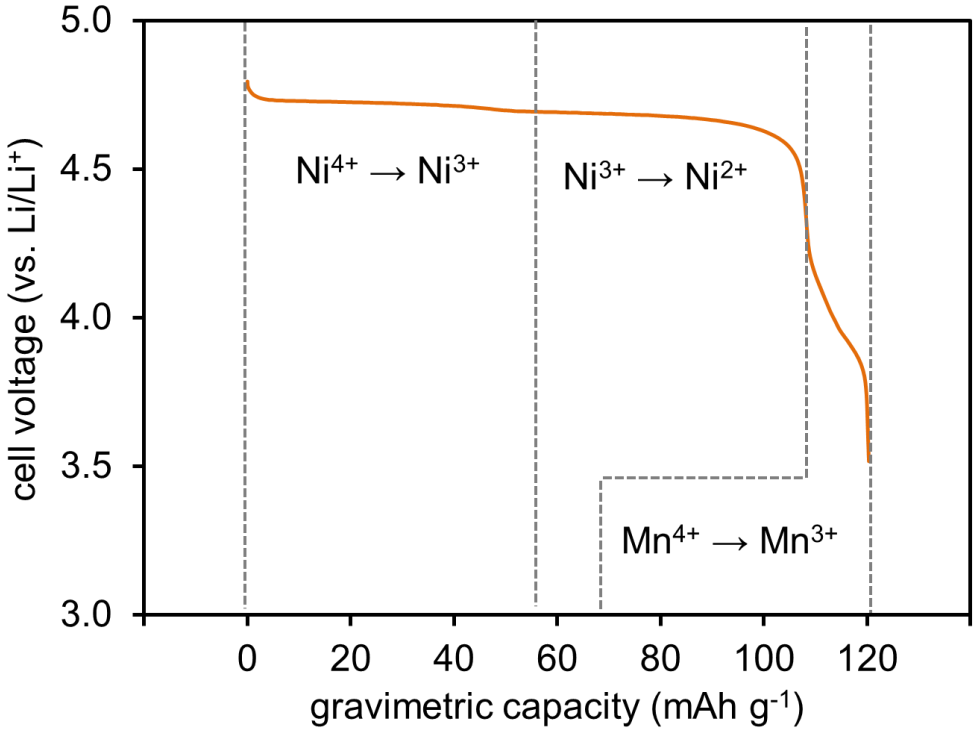

Figure 1.3 Electrochemical discharge curve of $LiMn_{1.5}Ni_{0.5}O_4$.

The theoretical gravimetric charge density (commonly referred to as gravimetric capacity) of high-voltage spinel is 146 mAh g^{-1}, which corresponds to the removal of one Li per formula unit ($LiMn_{1.5}Ni_{0.5}O_4$). On discharge, the practical reversible capacity is usually ~120 mAh g^{-1}. As lithium is inserted into the host structure, Ni^{4+} is the first to be reduced, then Ni^{3+}, and finally, Mn^{4+}. After a small amount of Mn^{4+} has been reduced to

Mn^{3+}, the tetrahedral sites are fully occupied by Li and the insertion potential falls below 3 V vs. Li/Li^{+}. In ideally stoichiometric high-voltage spinel, there should be no Mn^{3+} in the fully lithiated material. However, impurities formed during synthesis often increase the Mn/Ni ratio in the final product, yielding a small amount of Mn^{3+}.[27] Quantification of this initial Mn^{3+} content using magnetic measurements[29] is discussed in chapter 3.

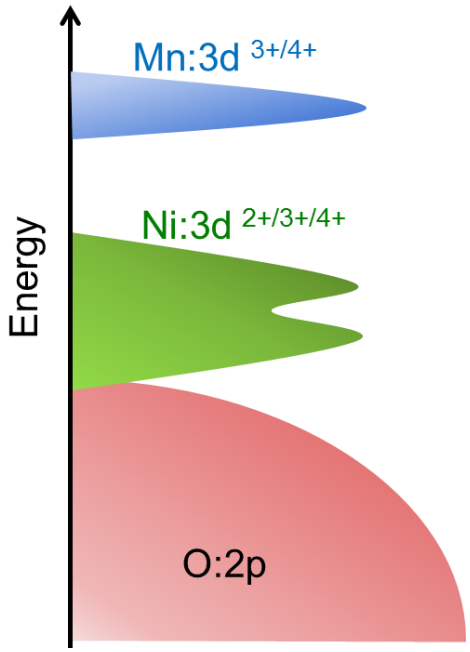

Figure 1.4 Energy and density of states (DOS) in high-voltage spinel.

A cartoon density of states (DOS) diagram illustrating the electronic structure of $LiMn_{1.5}Ni_{0.5}O_4$ is shown in Figure 1.4. The Ni:3d states are drawn below the Mn:3d, with the bottom of the Ni:3d band "pinned" to the top of the O:2p band. The $Ni^{3+/4+}$ and $Ni^{2+/3+}$ redox couples are so close together that they are drawn as a single band.

The most pressing issue facing the development of high-voltage spinel is its incompatibility with low-voltage anode materials such as graphite, Si, and other alloy compounds.[28,30,31] Unwanted moisture in the electrolyte can lead to HF formation, which

greatly accelerates the dissolution of Mn ions from the cathode.[31] There is a well-known disproportionation reaction involving the Mn^{3+} ion, where the Mn^{3+} donates its e_g electron to a neighboring Mn^{4+} resulting in a Mn^{2+} - Mn^{4+} pair.[32] The Mn^{2+} then readily dissolves in the electrolyte and diffuses through the separator to the other side of the cell, where it deposits on the anode.[33] The Mn contacts the graphite (or alternative anode) surface and forms an unstable SEI. The SEI continuously grows, sloughs off, and grows again, irreversibly consuming Li-ions in the process; this phenomenon is known as Mn poisoning[33] and it results in rapid, time-dependent capacity fade; that is, the capacity is a function of time spent at non-zero state-of-charge (SOC) in hours rather than the number of cycles the cell has experienced (cycle number is a common unit for the abscissa when plotting capacity; test time is less common).[34]

One way to avoid this issue is to combine high-voltage spinel with a high-voltage anode, such as $Li_4Ti_5O_{12}$ (LTO), which does not form an SEI layer due to its high redox voltage of ~1.5 V vs. Li/Li^+.[35] Because an SEI cannot form on the anode surface, the Mn poisoning issue is avoided. However, the high voltage and low gravimetric capacity of LTO (~170 mAh g^{-1}) results in a nominal cell voltage of ~ 3.2 V and much lower energy density than cells containing graphite as an anode. LTO is also much more expensive than graphite, driving cost of the cell up. Nonetheless, the $LiMn_{1.5}Ni_{0.5}O_4$ // $Li_4Ti_5O_{12}$ combination has been intensely researched, and displays remarkably fast solid-state diffusion kinetics in both electrodes allowing cells to charge and discharge at very high rates with little overpotential.[36] This cell chemistry may fill a niche role as a super-high-rate lithium-ion battery.

1.4.1 Cation Ordering in High-Voltage Spinel

Although high-voltage spinel faces several challenges including the Mn poisoning issue discusses above, it exhibits remarkably interesting solid state properties as well. A

defining characteristic of $LiMn_{1.5}Ni_{0.5}O_4$ is the tendency for Mn and Ni to display long-range ordering due to the size and charge difference of the Mn^{4+} and Ni^{2+} ions.[37] Disordered high-voltage spinel shares the same symmetry as $LiMn_2O_4$, but ordering of Ni on 4b Wyckoff sites and Mn on the 12d sites lowers the symmetry of the cubic unit cell to a primitive $P4_332$ space group. In this configuration, each Ni ion has six Mn nearest neighbors and zero Ni nearest neighbors. A 2-dimensional cross section of a (111) plane of the $P4_332$ high-voltage spinel is displayed in Figure 1.5 to illustrate this arrangement. Only the transition-metal ions are displayed for clarity. These ions form a pyrochlore sub-lattice with Kagome nets in the (111) planes.

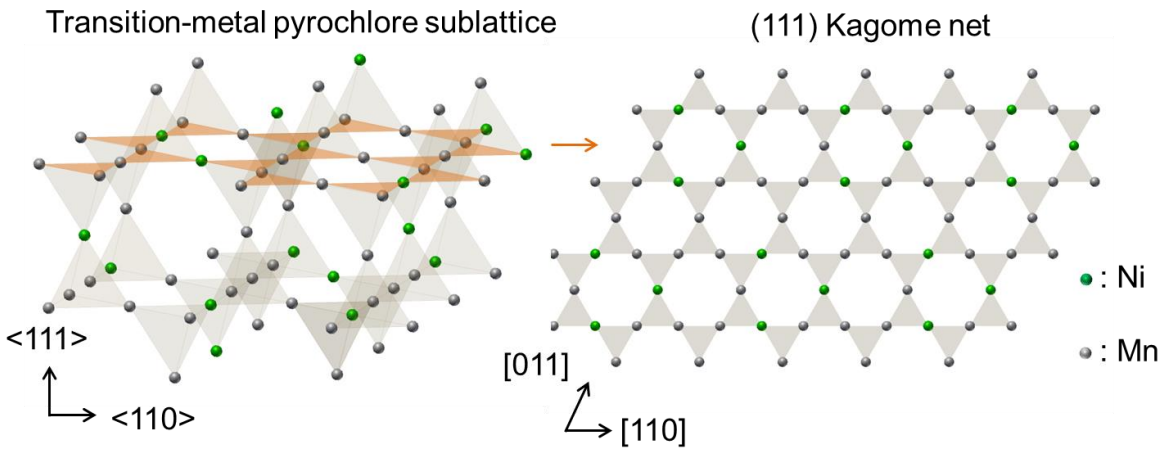

Figure 1.5 Arrangement of the transition-metal ions in cation ordered high-voltage spinel.

Cation disorder is typified by the existence of Ni-Ni nearest neighbors. In a real specimen, the metal-ions will not be perfectly ordered or disordered, but display some kind of intimate mixture of the two phases.[38] Typically, specimens are compared to one another by the "degree of cation ordering," which is a qualitative measure of the phase fraction of $P4_332$:Fd-3m. Quantitative measurement of this fraction is only obtained through Rietveld refinement neutron diffraction patterns using the ^7Li isotope.[38,39]

Therefore, measurements of the vibrational absorption energies via Fourier transform infrared spectroscopy (FTIR)[40] and the magnetic properties using a magnetometer[41,42] are often used to provide insight into the qualitative degree of cation ordering among a sample set without the need for a neutron spallation source. A diagram depicting this concept is shown in Figure 1.6. In this illustration, only the transition-metal sites are shown as corner-sharing cubes. Oxide ions occupy the opposite corners of the cubes. On the left, all 16d sites are represented in gray, while on the right, the Ni 4a and Mn 12b sites are shown in black and white, respectively. The exact configuration of the ordered and disordered domains is unknown at the time of writing.

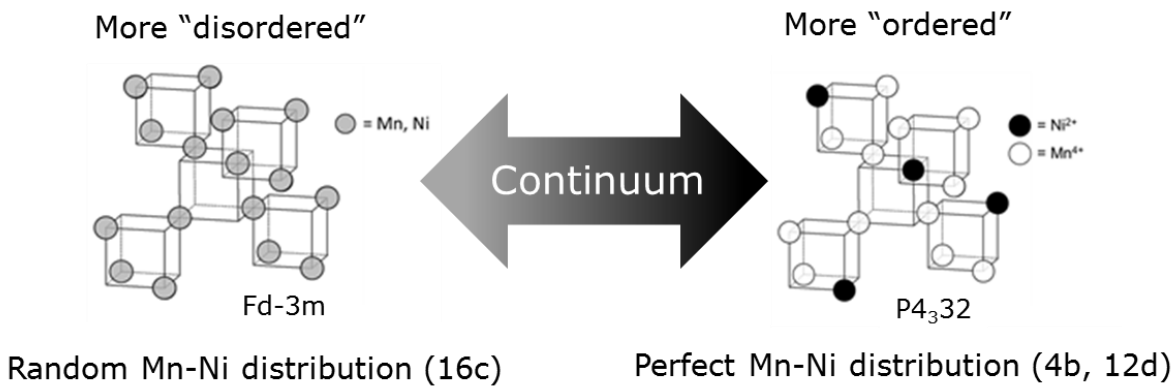

Figure 1.6 Illustration of the degree of cation ordering in high-voltage spinel.

The degree of cation ordering is heavily dependent on the high-temperature synthesis conditions, including temperature, time, and ramp rates. At 700^{o}C, cation ordering is encouraged and longer soak times at that temperature will result in more ordered final products. Above 700 ^{o}C, the high-voltage spinel phase is no longer stable as some Mn^{4+} is reduced to Mn^{3+}. This results in the formation of a Ni-rich rock-salt secondary phase, and the weight percent (wt%) of this phase increases with temperature.[27] To encourage atomic disorder, the synthesis temperature for high-voltage

spinel is 900 ^{o}C, at which a significant fraction of rock-salt phase exists. As the specimen cools through 700 ^{o}C, the rock-salt phase is mostly eliminated and the spinel phase is formed. Quickly cooling the specimen to room temperature will result in a higher amount of rock-salt phase in the product as well as increased cation disorder; quenching the sample will prevent the formation of the spinel phase. For this reason, cooling rates between 1 ^{o}C/min and 5 ^{o}C/min are used in this dissertation.

From a practical standpoint, the degree of cation ordering is important because it has been linked to poor electrochemical performance (rate capability and cyclability).[39,43,44] *i.e.*, for the same precursor, a spinel subjected to a long anneal at 700 ^{o}C will be inferior to the same spinel synthesized at 900 ^{o}C with no annealing step. Possible mechanisms responsible for this phenomenon are discussed in detail in chapter 5.

1.5 Magnetic Interactions in Oxides

The proportion of the induced magnetization of a compound (M) to the flux density of an external magnetic field (H) is called magnetic susceptibility. Compounds are classified as diamagnetic, paramagnetic, ferromagnetic, antiferromagnetic, or ferrimagnetic depending on their response to an applied field. While Fe, Ni, and Co are known for being the most common ferromagnetic metals, other compounds such as intermetallics and oxides display remarkable magnetic behavior. For instance, $Nd_2Fe_{14}B$, commonly referred to as the neodymium magnet, is a much stronger permanent magnet with a higher magnetization and coercivity than any pure metal.[45] Fe_3O_4, also called magnetite or lodestone, is a naturally occurring spinel-oxide ferrimagnet which was the first material discovered to exhibit permanent magnetism.[46]

The chemical formula for magnetite can also be written as: $(Fe^{3+})[Fe^{2+},Fe^{3+}]O_4$, which implies that Fe^{3+} ions occupy the tetrahedral sites and the octahedral sites are filled by a combination of Fe^{3+} and Fe^{2+}. The Fe^{3+} preference for tetrahedral sites over Fe^{2+} is explained by crystal field theory and octahedral site stabilization energy (OSSE).

The Fe^{3+} ion has five electrons in the 3d electron shell. In four or six-fold coordination, the five 3d orbitals are split into twofold degenerate e_g and threefold degenerate t_{2g} orbitals. Six-fold (octahedral) coordination results in a larger crystal field splitting energy with the t_{2g} orbitals lower in energy than the e_g orbitals. For the Fe^{3+} ion, each orbital is half-filled with one of the five 3d electrons according to Hund's rules. As energy of states is conserved, there is no net lowering of the energy of the 3d electrons in Fe^{3+}, regardless of the coordination number. However, the Fe^{2+} ion, with an extra electron in the orbitals of lower energy, is stabilized in six-fold coordination because the energy of the t_{2g} orbitals is lowered more than the energy by which the e_g orbitals are lowered in four-fold coordination. Therefore, if given a "choice" the Fe^{2+} will occupy an octahedral site before the Fe^{3+} ion.

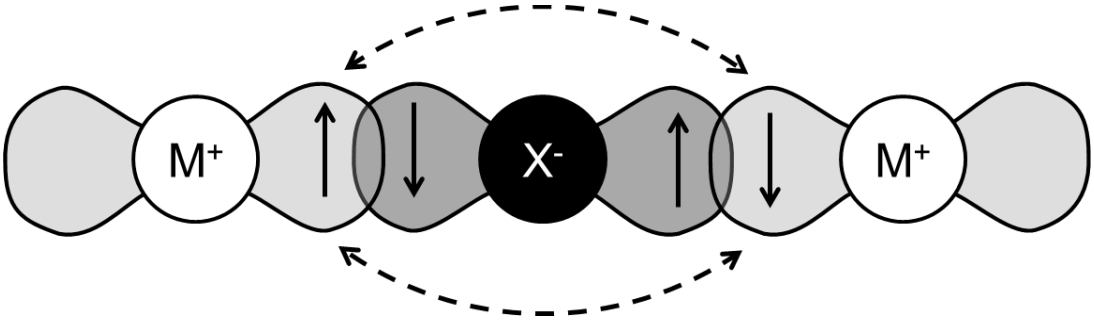

Figure 1.7 Antiferromagnetic superexchange between two half-filled orbitals.

It is the arrangement of Fe^{2+} and Fe^{3+} ions in the spinel lattice which give rise to permanent magnetism in Fe_3O_4. The A site Fe^{3+} ions are coupled antiferromegnetically to the B site Fe^{3+} and Fe^{2+} ions, resulting in a net ferromagnetic moment equivalent to 4

Bohr magnetons (μ_B) per formula unit. The coupling occurs via oxygen-mediated superexchange according to the Goodenough-Kanamori rules.[47,48] These predict whether or not a virtual electron transfer through an oxygen anion will result in ferro- or antiferromagnetic superexchange between two cations depending on their orbital orientations and occupancies. The overarching rule is that superexchange between two non-orthogonal orbitals will be antiferromagnetic if the orbitals are each half-filled, or contain one electron each. These rules also govern the magnetic exchange interactions in $LiMn_{1.5}Ni_{0.5}O_4$ between Mn-Mn, Mn-Ni, and Ni-Ni pairs. Chapter 3 explains these interactions in greater detail, and chapter 4 includes discussion on other interactions with Ni-substituted cations such as Cr^{3+}, Fe^{3+}, and Cu^{2+}. An illustration of an oxygen-mediated superexchange interaction is shown in Figure 1.7. The circles represent ionic nuclei and the teardrops, orbital lobes. The electrons on the M^{n+} ions are antiparallel to one another as a result of antiferromagnetic superexchange.

Many oxides are paramagnetic at room temperature but experience some kind of spontaneous magnetization below the magnetic transition temperature, commonly referred to as the Curie temperature (T_C) for ferromagnetic compounds and the Neèl temperature (T_N) for antiferromagnetic ones. The ferrimagnetic transition temperature is also called T_C in this dissertation. Curie-Weiss paramagnetism is common to ionic compounds with unpaired electron spins and is characterized by linear change in inverse magnetic susceptibility with respect to temperature. This gives rise to the Curie-Weiss law:

$$\chi = \frac{C}{T - T_C}$$

where χ is magnetic susceptibility, C is the Curie constant, and T_C is the transition temperature. From this equation, the oxidation states and electron configurations of various ions in the compound can be extracted. However, at temperatures near T_C, the

law does not hold and inverse magnetic susceptibility will be nonlinear. Other ways exist do determine the electronic and ionic structure of the material from M-H curves at low temperature. Many ferromagnetic or ferrimagnetic materials reach saturation magnetization in low fields near 0 K, where the magnetization reaches a limiting value based on the perfect (0^o canting) alignment of electron spins. It is in this way that the Mn^{3+} content was determined in high-voltage spinel as outlined in chapter 3.

1.6 Solvothermal Synthesis, Microwave Heat Sources, and the Polyol Reduction Method

Hydrothermal and solvothermal synthesis processes replicate natural single-crystal mineral growth in sealed autoclaves or vessels. As a super-saturated salt solution cools from high temperature and pressure, the product crystallizes on the walls of the container - the composition and morphology of the product depends on the elements in the salt, their solubility, and the properties of the solvent. This is a common synthesis method for preparing lithium-ion material precursors,[49,50] and was utilized to produce chloride- and sulfate-based precursors of $LiMn_{1.5}Ni_{0.5}O_4$ for the study in chapter 3.

Microwave based heating for hydro- and solvothermal synthesis has become more popular in laboratory settings in recent years due to increased efficiency.[51,52] The process is highly automated, accurate, can achieve much higher heat transfer rates than traditional heat sources, and can yield products with better morphological control than standard methods. Microwave-assisted solvothermal synthesis of $LiFePO_4$ and other phosphates has been thoroughly studied.[53–55]

Heat transfer to solvents with microwaves is achieved via molecular friction due to absorption of electromagnetic radiation by polar molecules.[56] The alternating electric field of the photons causes the solvent molecules to rotate in resonance with the incident

microwave frequency. Resistance to this rotation is provided by friction between the molecules and the energy is converted to heat. In this manner, much faster and more efficient heating of a solution can be achieved than by conventional methods such as conduction and forced convection.

Solvothermal reduction of solid reactants has been developed as an alternative to conventional atmospherically controlled reduction reactions using argon, hydrogen, CO_2, or combinations of the above.[57,58] The advantages of solution based processes include enhanced safety (no potentially poisonous or explosive gasses are involved) and more facile experimental procedures. The polyol technique has been successfully employed for template reduction of solid oxide reactants[59] and ion insertion reactions.[60] A combination of a microwave heat source and polyol reducing agent was employed in chapters 6 and 7 to develop new efficient chemical techniques for oxide reduction and ion insertion.

1.7 OBJECTIVES

The rapid proliferation and miniaturization of personal electronic devices and the 21st century return of the electric vehicle are having a significant impact on energy storage research and are driving the development of very energy dense batter systems. At present, lithium-ion technology is arguably the most practical solution to personal device and personal vehicle energy storage needs. That being said, the engineering and cost constraints are vastly different for each application, and different lithium-ion chemistries can fulfil different niche roles. For instance, because the battery is a smaller fraction of a cell-phone's overall cost, measures can be taken to improve the volumetric energy density even with a higher cost per kWh; the smaller battery allows manufacturers to produce physically thinner phones.

The same cannot be said for an electric vehicle, where the majority of the car's cost comes from the battery pack. The easiest way to lower the cost of an electric vehicle is to make the battery smaller. This lowers the driving range of the vehicle, which is unacceptable for batteries that demand long charge times. If a high-rate battery could be developed which could withstand high current charging, say 20C (three minutes to full charge) and enough high-power charging stations could be placed along highways and cities (think Tesla™ supercharger), the cost of electric vehicles could be lowered substantially without ever increasing the energy density. The more straightforward solution is to develop a battery with higher energy density (resulting in a lower cost per kWh) or to cram a larger battery in the car. However, the energy density of reliable, long-lasting lithium-ion batteries is not likely to improve significantly in the next few years without a major breakthrough.

Following the above logic, developing the understanding required to fashion a blueprint for a high-rate lithium-ion battery has been my primary research goal throughout my graduate studies. To that end, I have focused most of my effort to understanding the chemistry and physical properties of a promising high-rate cathode material: $LiMn_{1.5}Ni_{0.5}O_4$, which was introduced earlier in this chapter. First proposed as a cathode material in 1996,[26] it has recently been recognized as an excellent high-rate cathode.[61,62] It was proposed several years ago that initial Mn^{3+} content had a significant impact on the rate performance.[37,63] Chapters 3 and 4 introduce a new magnetic technique to measure the Mn^{3+} content in off-stoichiometric high-voltage spinel in the hopes that other researchers could use the technique to correlate Mn^{3+} content with performance. The degree of cation ordering has been convincingly linked to rate performance, so chapter 4 also explores a magnetic technique to qualitatively gauge the degree of cation ordering in several doped high-voltage spinel compounds. Chapter 5 explores the

electronic properties of high-voltage spinels with various degrees of cation ordering in an attempt to determine the impact of conductivity, Mn^{3+} content, and phase-change behavior on the rate performance. The conclusions of this chapter are in line with other recent literature on the subject.

Chapter 6 explains a facile chemical lithiation process for $LiMn_2O_4$ and $LiMn_{1.5}Ni_{0.5}O_4$ spinels. The extra lithium is used as a reservoir to compensate for the irreversible capacity of a nanocomposite anode material, FeSb-TiC, developed by my colleague, Eric Alcorn. The combination of a pre-lithiated spinel cathode and a dense nanostructured anode results in a cell capable of fast charging. The cell chemistry developed in chapter 6 lays the groundwork for other combinations of spinel cathodes and nano-alloy anodes to meet the demands of energetically dense or high-rate batteries. A similar process can be used generally as an approach to synthesize lower-valent transition-metal oxides, and is described in chapter 7.

Chapter 2: Experimental Procedures

2.1 Materials Synthesis

Continuously Stirred Tank Reactor

A continuously-stirred tank reactor (CSTR) with atmospheric, pH, and temperature controls was utilized to produce precursor materials for high-voltage spinel synthesis. The precursor solution was prepared by dissolving the metal sulfate or nitrate salts in deionized water at a 2M concentration and added to the reactor in a slow, drop-wise manner. The base solution consisted of 2 M NaOH and 0.05 M NH_4OH and was added to the tank reactor in a controlled manner to maintain a reaction pH of 10. The mixture was stirred at 1000 rpm in a nitrogen atmosphere at 60 °C for approximately 12 h. The hydroxide precipitate was vacuum-filtered and washed with deionized water before being dried overnight.

Solid State Mixing

The hydroxide precursors from the CSTR only contained Mn and Ni. Li was introduced to the precursor mixture by solid-state grinding. A stoichiometric amount of $LiOH{\cdot}H_2O$ was ground with the $(Mn,Ni)(OH)_2{\cdot}(H_2O)_x$ precursor to produce the final reactant mixture, which was then heated to the appropriate temperature for spinel formation.

Sol-Gel Method

A citrate and ethylenediaminetetraacetic acid (EDTA) sol-gel method was used to produce spinel and perovskite oxides used in chapters 6 and 7. Stoichiometric amounts of nitrate, acetate, or sulfate precursors were dissolved in nitric acid under magnetic stirring on a hot plate. Citric acid or EDTA was added as a chelating agent. Ammonium hydroxide solution was added to the solution to increase the pH to 7. The solution was

then stirred and heated at 95 °C to produce a gel. Stirring was discontinued and the gel was heated to ~ 400 ^{o}C to produce a black powder. The sol-gel product was heated to 600 ^{o}C for 4 h to remove carbonaceous and nitrous products, and then the final heat treatment was applied.

Microwave-Assisted Reduction of Oxides and Chemical Lithiation

An Anton-Paar Monowave 3000 microwave synthesis reactor was used for all microwave-assisted reactions. A tetraethylene glycol (TEG) solution was used as the microwave absorber and reducing agent. In a typical reaction, 0.5 g of reactant powder was suspended in 10 mL of TEG with magnetic stirring in a 30 mL borosilicate glass reaction vessel. The mixture was heated as fast as possible to the hold temperature of 160-300 ^{o}C for the specified hold time. The vessels were then cooled by forced air convection and the samples were washed via centrifugation with acetone and water to remove TEG. For chemical lithiation reactions, excess $LiOH{\cdot}H_2O$ was also removed.

2.2 MATERIALS CHARACTERIZATION

X-ray Diffraction

The majority of the powder X-ray diffraction (PXRD) patterns in this dissertation were collected with a Rigaku Ultima IV diffractometer in the Bragg-Bentano configuration and a Cu Kα X-ray source. Scans were typically taken from 10-80^{o} 2θ at a step size of 2^{o} 2θ with a dwell time of 3s at each step.

Thermogravimetric Analysis (TGA)

TGA was used to determine the water content in hydrated mixed-metal hydroxide precursors produced by the continuously stirred tank reactor process. Approximately 10 mg of precursor placed in an alumina crucible, which was heated in air to 900 ^{o}C and

cooled to room temperature. The hydrated hydroxide was converted completely to Mn-Ni spinel. From the measured weight change the initial water content could be obtained.

Iodometric Titration

Iodometric titration was employed to determine the oxidation state of transition-metal ions in several perovskite oxides in chapter 6. Approximately 50 mg of powder was added to a 15 mL solution of 10 wt% KI and 15 mL of 3.5 M HCl. The solution was titrated against 0.03 M sodium thiosulfate solution. The color of the solution would turn from deep yellow to straw yellow, at which point starch would be added as an indicator. The endpoint was recorded when the deep purple color was replaced with a light pink. The amount of titrant used was directly related to transition-metal oxidation state.

Inductively Coupled Plasma Optical Emission Spectroscopy (ICP-OES)

ICP-OES was heavily used in chapters 5 and 7 to determine the lithium content of chemically lithiated or delithiated samples. 2-3 mg of powder was dissolved in 1.5 mL of a mixture of nitric and hydrochloric acid. The dissolved sample was diluted with 250 mL of water before being fed into the spectrometer. Four standard specimens with known concentrations of Li, Mn, and Ni were used to calibrate the optical emission intensity with respect to solution concentration. The elemental ratios of Li/Mn, Li/Ni, and Mn/Ni could then be determined. The error associated with the process was estimated to be 3% for lithium and <1% for Mn and Ni.

Magnetic Characterization

A Quantum Design MPMS superconducting quantum interference device (SQUID) magnetometer was utilized in chapters 3 and 4 to characterize the magnetic properties of several $LiMn_{1.5}Ni_{0.5}O_4$ spinels. 20-40 mg of powder was loaded into a diamagnetic gelatin or Teflon capsule which was then affixed to the sample holder. In a

typical analysis, field-cooled (FC) magnetic susceptibility was measured in a field of 0.1 T from 5 K to 300 or 400 K, after which M-H curves would be measured at 5 K from 0 to 4 T. For the study in chapter 5, magnetic properties were measured with a vibrating sample magnetometer (VSM) attachment to a Quantum Design PPMS with the same experimental conditions.

AC Impedance Spectroscopy

Electronic conductivity of delithiated high-voltage spinel powders under pressure was measured with two-probe AC impedance. Four-probe measurements were not feasible because of the inability to create sintered pellets. The probe contacts were connected to tungsten carbide anvils which compressed the powder with a heated press. The powder was constrained radially with a compressible cardboard annulus. Measurements of the impedance vs. temperature were collected at 1 Hz to simulate direct current conditions while the plates were gradually heated. The temperature of the sample was measured with a K-type thermocouple and correlated to the impedance. From temperature and impedance measurements, the Arrhenius activation energy was calculated.

Seebeck Coefficient Measurements

With the pressed powder specimens from the AC impedance studies, the Seebeck coefficient was measured from 320 to 220 K with a homemade apparatus which used liquid nitrogen to cool the sample. Two brass plates on either side of the specimen were heated such that the temperature difference across the sample was 4 K while the induced voltage produced by the Seebeck effect was measured.

2.3 ELECTROCHEMICAL CHARACTERIZATION

Electrode Fabrication

Electrodes for lithium-ion cell construction used Al or Cu foil as current collectors for cathodes and anodes, respectively. Slurries were prepared by mixing the active material (spinel or graphite) with conductive carbon and polyvinylidene-fluoride (PVDF) binder in an n-methyl-pyrilidinone (NMP) solution. Mixtures consisted of 80 wt. % active material, 10 wt. % carbon, and 10 wt. % PVDF binder. The slurries were left under magnetic stirring for several hours to ensure thorough mixing. The viscous slurries were then cast onto the foil with a doctor blade and dried in a vacuum oven overnight to eliminate moisture. The electrode was then calendared and punched into 1 cm diameter circles to be used in coin cells.

Coin Cell Assembly

CR2032 stainless steel coin cells were employed to test the electrochemical performance of the prepared electrodes. The cells were assembled in an argon filled glovebox to avoid contamination of the cell with water and to provide an inert atmosphere for handling metallic lithium counter electrodes. The electrode was placed in the cell can followed by two polypropylene separators. Electrolyte was then added to the cell (in most cases, the electrolyte used was a 1:1 mixture of ethylene carbonate (EC) and diethyl carbonate (DEC) and 1 M $LiPF_6$). The counter electrode was then placed in the cell with a nickel foam layer to compress the components and provide an electrical contact for the counter electrode. The cell cap was then placed over the counter electrode and crimped to the cell can. The cells were then removed from the glovebox and tested on an Arbin Instruments battery cycler.

Chapter 3: Quantitative Determination of Mn^{3+} Content in $LiMn_{1.5}Ni_{0.5}O_4$ Spinel Cathodes by Magnetic Measurements

3.1 INTRODUCTION

Advanced rechargeable lithium-ion batteries are being pursued intensively for transportation and stationary energy storage of electricity produced by renewable sources like solar and wind.[4,64] These applications require long life and high charge-discharge rates along with high energy density. In this regard, the spinel $LiMn_{1.5}Ni_{0.5}O_4$ cathode is emerging as an attractive candidate due to its high operating voltage (~ 4.7 V), fast 3-dimensional lithium-ion diffusion, high electronic conductivity, and low cost.[4]

However, the properties and performance of $LiMn_{1.5}Ni_{0.5}O_4$ are sensitive to the synthesis and processing methods and conditions. Conventional solid-state, sol-gel, hydrothermal/solvothermal, and co-precipitation techniques have been pursued to synthesize cathode materials. Each method has a significant influence on the particle morphology, composition/stoichiometry (Ni/Mn ratio and oxygen content), phase purity, and degree of ordering between Mn^{4+} and Ni^{2+} in the 16d sites of the spinel lattice.[65,66] The non-stoichiometry (Ni/Mn ratio < 0.33 or oxygen content < 4.0) is characterized by the presence of Mn^{3+}, which has a significant influence on the voltage profile with capacity in the 4 V region and on other electrochemical performance parameters.[67] Synthesis of $LiMn_{1.5}Ni_{0.5}O_4$ at 900 °C with an ideal Ni/Mn ratio of 0.33 often results in the formation of trace amounts of the rock-salt impurity phase $Li_xNi_{1-x}O$.[68,69] This impurity is electrochemically inactive and tends to decrease the specific capacity of the material. Interestingly, the $Li_xNi_{1-x}O$ impurity phase vanishes on annealing the 900 °C

Z. Moorhead-Rosenberg, D. Shin, K. Chemelewski, J.B. Goodenough, & A. Manthiram. Quantitative determination of Mn^{3+} content in $LiMn_{1.5}Ni_{0.5}O_4$ spinel cathodes by magnetic measurements. *Applied Physics Letters* 100, 213909 (2012). D. Shin and K. Chemelewski provided some materials, XRD, and SEM used in this study. J.B. Goodenough provided insights and A. Manthiram supervised the project.

sample in air at 700 °C, indicating an increase in Ni solubility in the lattice at lower temperatures. Furthermore, annealing at 700 °C increases the cationic ordering between Mn^{4+} and Ni^{2+} and stabilizes the cation-ordered $P4_332$ structure relative to the cation-disordered *Fd*-3*m* structure.[68]

$LiMn_{1.5}Ni_{0.5}O_4$ has a ferrimagnetic ordering below the Curie temperature (T_c) with the Li^+ ions occupying the 8a tetrahedral sites and the Mn^{4+} and Ni^{2+} ions occupying the 16d octahedral sites. Since 180° M−O−M (M = Mn, Ni) superexchange pathways do not exist in the spinel structure, only direct t-t and 90° t-e superexchange mediated by the oxygen p-orbitals are allowed. Each magnetic ion in the 16d sites has 6 neighboring magnetic ions, with two 90° pathways to each.

Since the Mn^{3+} content influences significantly the electrochemical performance and electronic conductivity of $LiMn_{1.5}Ni_{0.5}O_4$,[40] the objective of this study was to use a magnetic measurement to determine quantitatively the Mn^{3+} content in $LiMn_{1.5}Ni_{0.5}O_4$ synthesized by various methods. Mn^{3+} content as determined from the extrapolated magnetization at 0 K correlates well with the electrochemical charge-storage capacity measured in the 4 V region. Based on the particle morphology, the nominal $LiMn_{1.5}Ni_{0.5}O_4$ samples obtained by various synthesis methods are termed polyhedral 1, polyhedral 2, cubic, spherical 1, and spherical 2. The data obtained with the samples of different morphologies are also compared with those of a commercial $LiMn_{1.5}Ni_{0.5}O_4$ sample.

3.2 EXPERIMENTAL

Mixed-metal carbonate and hydroxide precursors of Mn and Ni were prepared by co-precipitation and hydrothermal processes. The precursors for the spherical 1 and polyhedral 1 samples were prepared with a tank reactor by co-precipitating, respectively, the carbonates and hydroxides of Mn and Ni with sodium carbonate and sodium

hydroxide and employing ammonium hydroxide as a complexing agent. The hydroxide precursor for the polyhedral 2 sample was prepared by the traditional co-precipitation method by a drop-wise addition of Mn and Ni acetates to potassium hydroxide. The precursors for the cubic and spherical 2 samples were synthesized by the hydrothermal method. For the cubic precursor, urea and cetyl trimethylammonium bromide (CTMB) surfactant were mixed with stoichiometric amounts of $MnCl_2$ and $NiCl_2$ in deionized water and heated at 150 °C for 15 h in an autoclave. The CTMB to solvent weight ratio was 1 : 3.3. The spherical 2 precursor was prepared in the same manner with $MnSO_4 \cdot H_2O$, $NiSO_4 \cdot 6H_2O$, and urea, but without the CTMB surfactant. The precursors formed were filtered and dried overnight in an air oven at 115 °C. All mixed-metal precursors were then ground with a required amount of $LiOH \cdot H_2O$ and heated at 900 °C in air for 10 – 12 h to produce the final materials.

The samples were characterized by X-ray diffraction (XRD) with Cu Kα radiation. Electrochemical measurements were carried out at C/6 rate with CR2032 coin cells with lithium metal anode and 1 M $LiPF_6$ in 1:1 vol. % ethylene carbonate (EC) / diethyl carbonate (DEC) electrolyte. Cathodes were fabricated by suspending 80 wt. % active material, 10 wt. % conductive carbon, and 10 wt. % polyvinylidene fluoride (PVDF) in n-methyl-2-pyrrolidone (NMP) solvent and casting onto an aluminum foil current collector. Magnetic measurements were carried out with a Quantum Design SQUID magnetometer on powder samples with masses of 15 − 30 mg.

3.3 Results and Discussion

The XRD patterns shown in Figure 3.1 reveal that the samples synthesized at 900 °C have the cation-disordered *Fd*-3*m* cubic spinel structure with a trace amount of the rock-salt $Li_xNi_{1-x}O$ impurity. On the other hand, the samples annealed at 700 °C have no $Li_xNi_{1-x}O$ phase.

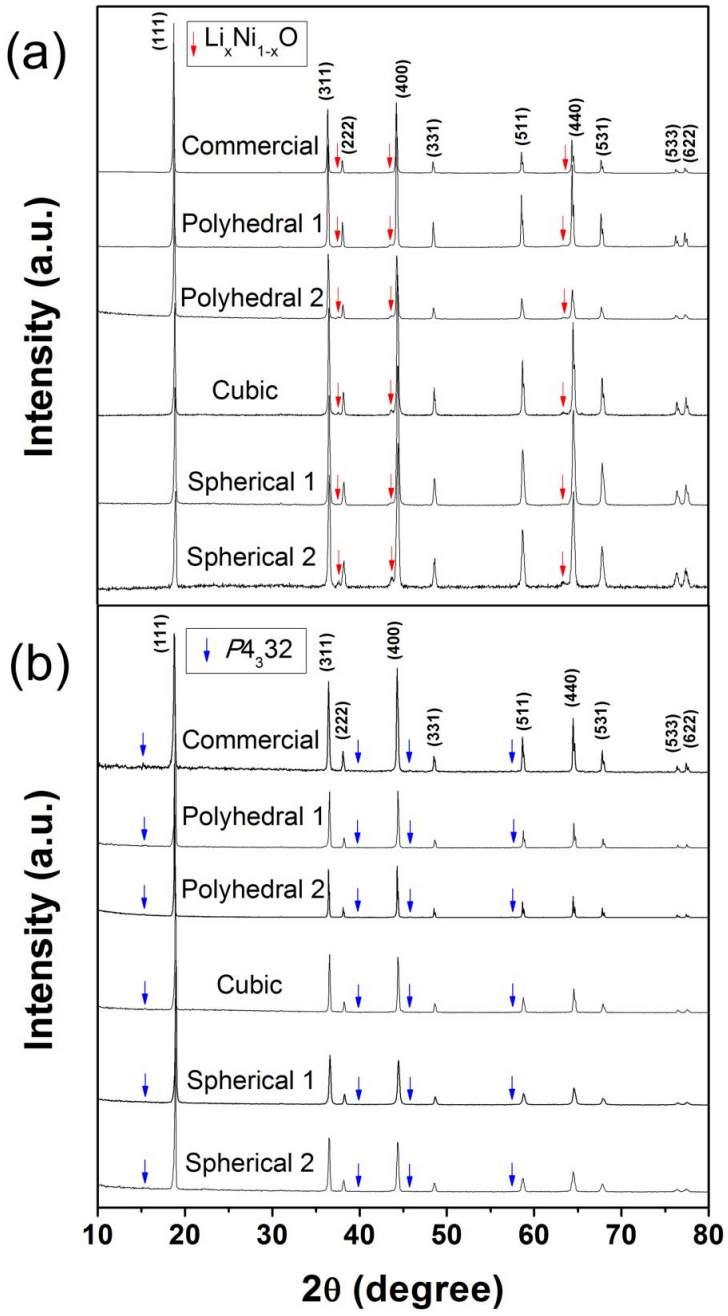

Figure 3.1 XRD patterns of the $LiMn_{1.5}Ni_{0.5}O_4$ spinel samples (a) synthesized at 900 °C and (b) after annealing the 900 °C samples in air at 700 °C.

Figure 3.2 compares the first charge/discharge curves of the 900 °C and 700 °C samples, as well as the particle morphology. The polyhedral 1 sample consists mainly of

octahedral particles of approximately 1 − 3 μm size, while the polyhedral 2 sample is composed of truncated octahedra approximately 2 − 6 μm size. The commercial sample is similar to the polyhedral sample in terms of morphology, but the average particle size is considerably smaller (~ 1 μm). The spherical 1, spherical 2, and cubic samples consist of sub-micron size crystallites arranged in larger spherical or cubic particles of approximately 12 μm size. The voltage profiles are typical of the $LiMn_{1.5}Ni_{0.5}O_4$ spinel. The presence of Mn^{3+} ions in the samples is evidenced by the capacity in the 4 V region,[70] and the Mn^{3+} content calculated from the 4 V capacity values are indicated for each sample in Figure 3.2.

The cation-disordered *Fd*-3*m* samples exhibit a roughly uniform T_c of ~ 125 K, while the cation-ordered $P4_332$ samples exhibit a slightly higher T_c of ~ 129 K, which is in accordance with previous studies.[65] The inverse susceptibility curves exhibit a non-linear slope in the paramagnetic regime, characteristic of ferrimagnetic materials. Despite the significant variations in the Mn^{3+} content among the samples synthesized at the same temperature of 900 °C, the Curie temperature does not vary, implying that T_c is not significantly influenced by the Mn^{3+} content but is influenced slightly by the degree of cation ordering.

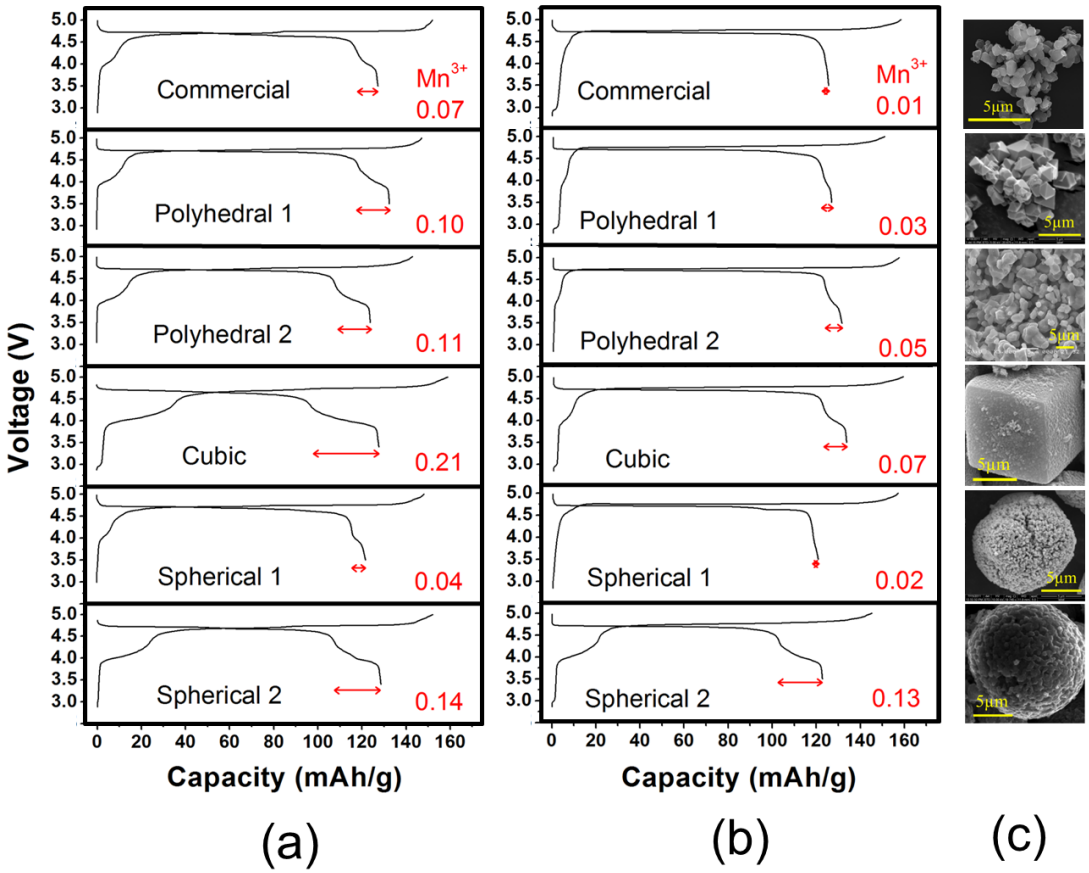

Figure 3.2 Electrochemical first charge/discharge curves at a C/6 rate (1C = 146.7 mA/g) of the $LiMn_{1.5}Ni_{0.5}O_4$ spinel samples (a) synthesized at 900 °C and (b) after annealing the 900 °C samples at 700 °C and (c) SEM images of the spinel particles with different morphologies. The numbers in (a) and (b) represent the Mn^{3+} contents calculated from the capacity in the 4 V region.

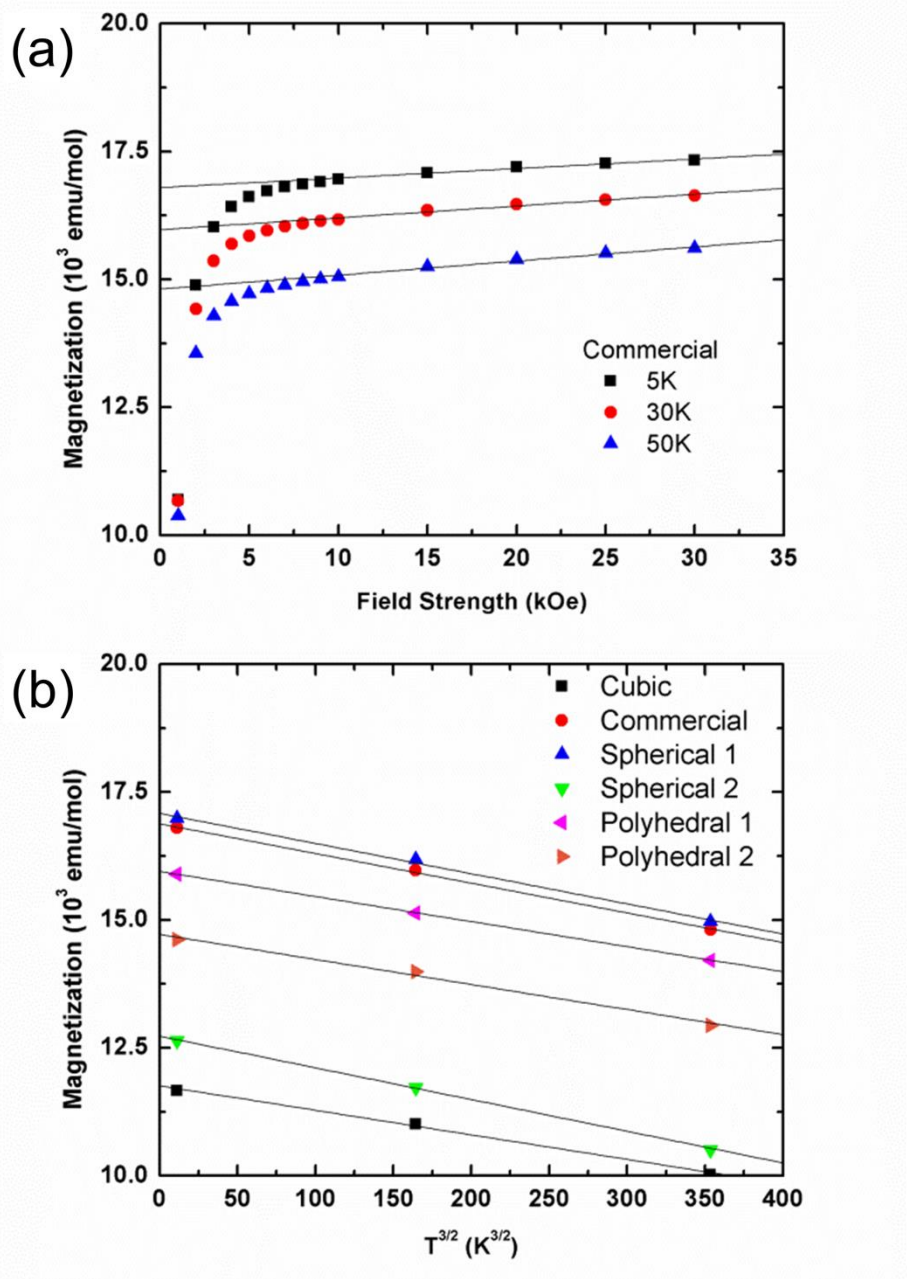

Figure 3.3 (a) Magnetization versus applied field for the 900 °C commercial sample at 5, 30, and 50 K with corresponding linear regression in the 10 – 30 kOe range and (b) the saturation magnetization plotted versus $T^{3/2}$ with linear regression. The saturation magnetization is taken as the y-intercept of the regression lines from (a).

One of the most common methods to estimate the content of various ions in magnetic materials is the Curie-Weiss law. However, this method is not reliable for $LiMn_{1.5}Ni_{0.5}O_4$ since the inverse magnetic susceptibility is characterized by curvature in the paramagnetic region.[71] Measurement at much higher temperatures could eliminate the curvature, but higher temperatures could result in the loss of oxygen from the lattice and variations in the Mn^{3+} content.[40] Another way to estimate the content of various ions in magnetic materials is to estimate the saturation magnetization at 0 K and compare it to the expected value based on the anticipated spin configuration of the magnetic ions. Since the magnetic moment per formula unit at 0 K cannot be directly measured, the magnetization of each sample at 5, 30, and 50 K was measured and extrapolated the data to estimate the moment at 0 K. Accordingly, the saturation magnetization for each temperature was first calculated by a linear regression of the magnetization vs. field strength curves recorded in the 10 – 30 kOe region. This step can be seen in Figure 3.3a for the 900 °C commercial material (the data for only one material is shown for clarity reasons). The saturation magnetization at each temperature is taken as the y-intercept of the regression line. The magnetic moment at 0 K was then estimated by applying a linear regression to the saturation magnetization at 5, 30, and 50 K vs. $T^{3/2}$, where T is temperature. This step is illustrated in Figure 3.3b. The actual magnetic moment per formula unit can be found by scaling this value based on the concentration of impurity (this is an iterative calculation). As can be seen in Figure 3.4, a strong linear correlation exists for all the samples between the 0 K moment per formula unit obtained by this method and the Mn^{3+} content obtained from the capacity values in the 4 V region.

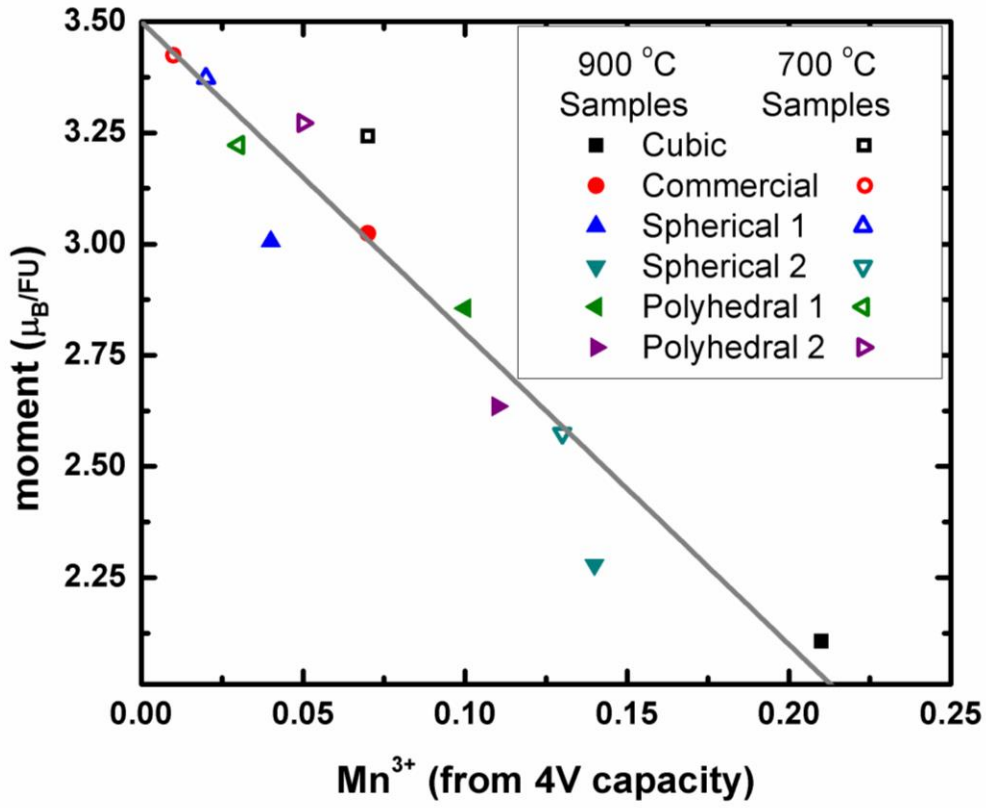

Figure 3.4 Variation of the magnetization extrapolated to 0 K with the Mn^{3+} content obtained from the electrochemical capacity values. The line represents the magnetic moment values based on equation 2 with $N_{Mn} = 1.5$ and $N_{Ni} = 0.5$.

The correlation between the magnetic moment and the Mn^{3+} content arises as a result of the way in which the ions order magnetically below T_c. The $LiMn_{1.5}Ni_{0.5}O_4$ structure fosters a competition between metal-metal and 90° metal-oxygen-metal superexchange interactions. Only two magnetic ions are present in stoichiometric $LiMn_{1.5}Ni_{0.5}O_4$: Mn^{4+} and Ni^{2+}. The Mn^{4+}:t^3e^0 ions have three half-filled π-bonding t orbitals, so the t-t interaction between edge-shared Mn^{4+} ions is antiferromagnetic. This interaction is, for example, dominant in delithiated λ-MnO_2, which displays a complicated antiferromagnetic ordering below the Néel temperature (T_N).[72]

$LiMn_{1.5}Ni_{0.5}O_4$ has a larger lattice parameter than λ-MnO_2, resulting in a smaller t-t overlap integral.[71,72] This reduction in the overlap integral could be large enough to shift the dominant superexchange interactions to those through the 90° pathways. The 90° Mn^{4+}–O–Mn^{4+} π-σ interactions couple a half-filled t orbital and an empty e orbital to give a ferromagnetic interaction, thus reducing the strength of the Mn^{4+}–Mn^{4+} interactions relative to the 90° Mn^{4+}–O–Ni^{2+} interactions. The Ni^{2+}:t^6e^2 ions support no t-t interaction between filled t orbitals and the 90° Ni^{2+}–O–Ni^{2+} π-σ interactions between t^6 and e^2 configurations are ferromagnetic. Direct interactions between orthogonal e orbitals are also ferromagnetic, so the Ni^{2+}–Ni^{2+} interactions are ferromagnetic, as has been demonstrated in the spinel $Ge[Ni_2]O_4$.[73] The Mn^{4+}–Ni^{2+} interactions are dominated by electron transfer from the Ni^{2+} to the Mn^{4+} ions. The π-σ interaction couples half-filled Mn^{4+}:t^3 and Ni^{2+}:e^2 orbitals to give an antiferromagnetic interaction that is stronger than any direct interaction between a half-filled e orbital on Ni^{2+} and an orthogonal empty e orbital on Mn^{4+} ions. The combination of these interactions means that within stoichiometric $LiMn_{1.5}Ni_{0.5}O_4$, the electron spin moments of the Mn^{4+} ions are parallel to each other and antiparallel to those of the Ni^{2+} ions, resulting in a theoretical magnetic moment of 3.5 μ_B per formula unit as given by the relation,

$$\mu = g_e S_{Mn^{4+}} N_{Mn^{4+}} - g_e S_{Ni^{2+}} N_{Ni^{2+}} \qquad (1)$$

where μ is the magnetic moment per formula unit in Bohr magnetons, $g_e = 2$ is the spin only electron g-factor, S is the total spin of the ion, and N is the number of transition metal ions per formula unit (for stoichiometric $LiMn_{1.5}Ni_{0.5}O_4$, $N_{Mn}4+ = 1.5$ and $N_{Ni}2+ = 0.5$).[74]

Some studies have indicated that $LiMn_{1.5}Ni_{0.5}O_4$ exhibits a magnetic moment significantly lower than the theoretical value of 3.5 μ_B.[74,75] In this study, values are measured for the samples synthesized by various methods ranging from 3.42 μ_B for the

sample with the shortest 4 V plateau (cation-ordered sample) to 2.11 μ_B for the sample with the longest 4 V plateau (cation-disordered sample). The observed magnetic moment is lower than the theoretical value of 3.5 μ_B due to the presence of Mn^{3+} in the samples.

The as-synthesized 900 °C samples contain the $Li_xNi_{1-x}O$ impurity phase and show a plateau at ~ 4 V in the charge/discharge profiles, indicating the presence of Mn^{3+}. Therefore, the chemical formula of the spinel phase can be more accurately represented as $LiMn_{1.5+x}Ni_{0.5-x}O_4$, which contains three transition metal ions: Mn^{4+}, Mn^{3+}, and Ni^{2+}. In a highly disordered spinel, interactions between any combination of these ions may exist; thus it is beneficial to examine each possible interaction to predict the total magnetization per formula unit of the spinel phase.

Interactions between high-spin Mn^{3+}:t^3e^1 and Ni^{2+}:t^6e^2 are difficult to predict definitively without the knowledge of the e-orbital order. However, local charge neutrality dictates that the Ni^{2+} will attract Mn^{4+} near neighbors preferentially, so the critical Mn^{3+} interactions are between Mn^{3+} and Mn^{4+} ions. The dominant interaction of this pair is a π-σ 90° interaction between a half-filled Mn^{3+}-e and half-filled Mn^{4+}-t^3 configuration, which is antiferromagnetic. The e orbitals on the interacting Mn cations are orthogonal to one another, but this direct interaction is weak since the Mn^{4+}-e orbital is empty. $LiMn_2O_4$, which contains equal parts of Mn^{3+} and Mn^{4+}, is characterized by antiferromagnetic interactions between ions,[76] which supports the assertion that the dominant Mn^{3+}–Mn^{4+} interaction is antiferromagnetic in $LiMn_{1.5}Ni_{0.5}O_4$ as well. The trend displayed in Figure 3.4 suggests that Mn^{3+} spins align antiparallel to the Mn^{4+} spins (parallel to the Ni^{2+} spins), which indicates that either the dominant Mn^{3+}–Ni^{2+} interaction is ferromagnetic or the Mn^{3+} ions are dominated by a sufficient number of nearby Mn^{4+} ions.

Thus, neglecting any contribution from the rock-salt $Li_xNi_{1-x}O$, the overall magnetic moment of a non-stoichiometric $LiMn_{1.5+x}Ni_{0.5-x}O_4$ sample can be given by a modified version of equation 1 to include the spin moments from the Mn^{3+} ions as

$$\mu = g_e S_{Mn^{4+}} N_{Mn^{4+}} - g_e S_{Mn^{3+}} N_{Mn^{3+}} - g_e S_{Ni^{2+}} N_{Ni^{2+}} \qquad (2)$$

The magnetic moment calculated based on equation 2 is plotted alongside the measured values in Figure 3.4 to show the correlation. For $LiMn_{1.5}Ni_{0.5}O_4$, the moment should be 3.5 μ_B, but when even trace amounts of Mn^{3+} ions are present, the moment is reduced considerably due to the four unpaired electrons on Mn^{3+}. NiO and $Li_xNi_{1-x}O$ have very unusual magnetic properties that vary with composition.[77–79] The magnetization of NiO nanoparticles and rock-salt $Li_xNi_{1-x}O$ are about an order of magnitude lower than that of $LiMn_{1.5}Ni_{0.5}O_4$, rendering the contribution of the impurity to the overall magnetic moment negligible.[77,79] Additionally, the rock-salt $Li_xNi_{1-x}O$ would reveal itself as a deviation from linearity in the magnetization curves at its T_c of ~ 200 K.[77] If an assumption is made that only spinel and $Li_xNi_{1-x}O$ rock-salt phases exist and that Mn^{3+} develops only as a result of $Li_xNi_{1-x}O$ precipitation (not as a result of lattice imperfections), the ion concentrations can be calculated based on the measured magnetic moment and charge neutrality; the results are summarized in Table 3.1.

Table 3.1 Extrapolated moment per formula unit (FU) at 0 K and the Mn^{3+} contents calculated from the electrochemical capacity values and magnetic data for the $LiMn_{1.5}Ni_{0.5}O_4$ spinel samples synthesized at 900 °C and after annealing the 900 °C samples in air at 700 °C.

Sample	900 °C samples			700 °C samples		
	Moment (μ_B/FU)	Mn^{3+} (capacity)	Mn^{3+} (magnetic)	Moment (μ_B/FU)	Mn^{3+} (capacity)	Mn^{3+} (magnetic)
Commercial	3.02	0.07	0.07	3.42	0.01	0.01
Polyhedral 1	2.86	0.10	0.10	3.22	0.03	0.04
Polyhedral 2	2.64	0.11	0.13	3.27	0.05	0.03
Spherical 1	3.06	0.04	0.07	3.37	0.02	0.02
Spherical 2	2.28	0.14	0.19	2.57	0.13	0.14
Cubic	2.11	0.21	0.22	3.24	0.07	0.04

As seen in Table 3.1, the Mn^{3+} contents obtained from the 4 V capacity and the magnetic method agree closely for each sample. It is interesting to note that the spherical 2 sample displays little change in the Mn^{+3} content after annealing at 700 °C.

Equation 2 is an ideal estimate; deviation from the expected value may be caused by a number of parameters, including differences in lithium content that could affect the charge balance and hence the Mn^{3+} content. Also, an assumption is made that the Mn^{3+} concentration is sufficiently low as to preclude the possibility of dominant Mn^{3+}−O−Mn^{3+} interactions, which are neglected in our analysis. Since all the samples measured have a Mn^{3+} content of < 0.25, it is unlikely that there is sufficient interaction between Mn^{3+} ions to produce any significant error.

3.4 CONCLUSION

A strong correlation exists in high-voltage spinel between the magnetic moment value extrapolated at 0 K and the amount of Mn^{3+} content obtained from the measured electrochemical capacity value in the 4 V region. This correlation is due to $LiMn_{1.5+x}Ni_{0.5-x}O_4$ undergoing ferrimagnetic ordering below $T_c \approx 125$ K for the disordered *Fd*-3*m* spinel and $T_c \approx 129$ K for the $P4_332$ ordered spinel in which the Mn^{4+} spin aligns parallel to the magnetic field and the Mn^{3+} and Ni^{2+} spins align antiparallel. This behavior has been explained by the possible superexchange interactions between ions. This magnetic measurement method could become valuable for quantitatively determining the Mn^{3+} content in the high-voltage $LiMn_{1.5+x}Ni_{0.5-x}O_4$ spinel cathodes and thus for developing a better understanding of their electrochemical properties.

Chapter 4: Magnetic Measurements as a Viable Tool to Assess the Relative Degrees of Cation Ordering and Mn^{3+} Content in Doped $LiMn_{1.5}Ni_{0.5-x}M_xO_4$ Spinel Cathodes (M = Al, Cr, Co, Ga, Mn, Fe, Cu)

4.1 INTRODUCTION

One of the most attractive characteristics of $LiMn_{1.5}Ni_{0.5}O_4$ is the high operating voltage of ~ 4.7 V vs. Li/Li^+, ensuring a higher energy density compared to the 4 V spinel $LiMn_2O_4$, which is currently employed as the cathode in production electric vehicles powered by Li-ion batteries.[80] However, several challenges persist, which must be further examined in order to develop an in-depth understanding of the properties of the high-voltage spinel cathodes: role of cation order/disorder on the cyclability and rate capability,[37,81,82] surface segregation of dopant ions,[82] morphological considerations,[83] problems inherent with full-cell construction,[84] and stability with the electrolyte and solid-electrolyte interphase (SEI) layer formation.[84]

The degree of cation ordering is particularly interesting, since no consensus exists on why the ordered $P4_332$ phase is innately inferior to the higher-symmetry $Fd\text{-}3m$ (disordered) phase in terms of electrochemical behavior. The $P4_332$ phase consists of a unit cell in which the Ni^{2+} and Mn^{4+} ions have a 1:3 ratio and they preferentially order, respectively, in the 4b and 12d octahedral sites. There is no such regularity in the disordered structure wherein the Mn^{4+} and Ni^{2+} ions are, to relative degrees, randomly distributed among the 16d octahedral sites.[44] Doping to obtain compositions such as $LiMn_{1.5}Ni_{0.5-x}M_xO_4$ (M = Cr, Mn, Fe, Co, Cu, Al, and Ga) has been employed as a strategy to suppress the cation ordering behavior and enhance the safety and electrochemical performance.[85,86] This improvement has been attributed to factors such as

---

Z. Moorhead-Rosenberg, K. Chemelewski, J.B. Goodenough, & A. Manthiram. Magnetic measurements as a viable tool to assess the relative degrees of cation ordering and Mn^{3+} content in doped $LiMn_{1.5}Ni_{0.5}O_4$ spinel cathodes. *Journal of Materials Chemistry A* 36, 10745-52 (2013). K. Chemelewski provided some material used in this study. J.B. Goodenough provided insights and A. Manthiram supervised the project.

segregation of the dopant ions to the surface, enhanced electronic conductivity, elimination of the rock-salt phase impurity, and effective disruption of Mn^{4+} and Ni^{2+} cation ordering.[87,88]

One of the most effective ways to synthesize a disordered spinel phase is to fire the precursor materials to 900 °C and cool the product to room temperature. An impurity Ni-rich rock-salt phase, identified herein as $Li_xNi_{1-x}O$, typically forms at this temperature; its contribution to the final product can be reduced by cooling the sample at a slow rate.[89] As a result of the formation of the rock-salt phase, some amount of Ni is robbed from the electrochemically active spinel, resulting in a Mn:Ni ratio > 3 in the spinel phase. To maintain electrical charge neutrality, some amount of Mn^{4+} is reduced to Mn^{3+}, the presence of which is clearly identified in the charge/discharge curves of the Li-ion cells as a voltage plateau at ~ 4 V corresponding to the $Mn^{3+/4+}$ redox couple. This plateau is absent or negligible in a well-ordered spinel, indicating a 3:1 ratio of Mn to Ni in the spinel phase with an elimination of the rock-salt impurity. The high-voltage spinel is typically transformed to the ordered phase by annealing the product at 700 °C for an extended amount of time with a slow cooling rate.[89] Depending on the synthesis technique, sample preparation, Mn:Ni stoichiometry, annealing time, and dopant species concentration, it is thought that the relative degree of cation ordering can change drastically, as can the electrochemical performance of the spinel as a cathode material.[81] Thus, it is critical to develop methods by which the relative degree of cation ordering among different samples can be readily determined.

To this end, magnetic susceptibility and magnetization measurements are emerging as a valuable tool to examine the chemistry and physics of the ordered and disordered phases, allowing for the differentiation between the two.[29,38,41,65,74,90] Accordingly, this study is focused on correlating the magnetic properties of doped

$LiMn_{1.5}Ni_{0.42}M_{0.08}O_4$ (M = Cr, Fe, Co, Cu, Al, and Ga) and Mn-rich $LiMn_{1.5+x}Ni_{0.5-x}O_4$ ($0 \leq x \leq 0.1$) to the Mn^{3+} content and relative degree of cation order. The results obtained are compared with the electrochemical charge/discharge curves of lithium-ion cells.

4.2 EXPERIMENTAL

All samples were synthesized with a continuously-stirred tank reactor (CSTR) with two feedstock solutions. The first solution was prepared at 2 M concentration with the appropriate stoichiometric amount of metal salts necessary to produce the hydroxide precursor. The metal salts used in the synthesis were: $MnSO_4 \cdot H_2O$, $NiSO_4 \cdot 6H_2O$, $Cr(NO_3)_3 \cdot 9H_2O$, $FeSO_4 \cdot 7H_2O$, $CoSO_4 \cdot 7H_2O$, $Cu(NO_3)_2 \cdot H_2O$, $Al(NO_3)_3 \cdot 9H_2O$, and $Ga(NO_3)_3 \cdot H_2O$. Another solution with a 2 M concentration of NaOH and 0.05 M concentration of NH_4OH was continuously added to the mixture with the purpose of maintaining a solution pH of 10. The mixture was stirred at 1000 rpm in a sealed nitrogen atmosphere at a temperature of 60 °C for 12 h. The coprecipitate formed was filtered and washed with deionized water and subsequently dried overnight in air at 110 °C. The water content of the metal hydroxide precursor was determined by thermogravimetric analysis (TGA), after which it was ground with a stoichiometric amount of $LiOH \cdot H_2O$. This mixture was then fired at 900 °C for 15 h and cooled at a rate of 1 °C/min to produce the final product. A portion of this material was also annealed at 700 °C for 48 h with a cooling rate of 1 °C/min in an effort to produce a cation-ordered spinel.

X-ray diffraction (XRD) patterns were collected with a Rigaku powder diffractometer with a 0.02 2θ step size and a three second dwell time. Magnetic measurements were carried out with a Quantum Design SQUID magnetometer on powder samples of the raw cathode material (no carbon or binder) encased in glycerin capsules. Field-cooled (FC) measurements were performed by cooling the sample in a field of 0.1 T down to 5 K and then measuring the DC susceptibility as the temperature

was increased to 300 K. Saturation magnetization measurements were conducted at field strengths of 1-4 T at 5 K.

Electrochemical measurements were carried out with Li-ion half-cells. The cathodes were prepared by a PVDF casting method. A slurry was prepared with 80 wt. % active material, 10 wt. % conductive carbon, and 10 wt. % polyvinylidene fluoride (PVDF) in a N-methyl-2-pyrrolidone (NMP) solvent. The slurry was stirred overnight with a magnetic stir bar in a glass vial and was then cast onto an aluminum-foil current collector and dried under vacuum at 100 °C for 12 h. Cathode disks loaded with approximately 4 mg active material were punched from the sheets and assembled in CR2032 coin cells with a lithium metal anode and 1 M $LiPF_6$ in ethylene carbonate (EC) / diethyl carbonate (DEC) (1:1 vol.) as the electrolyte. Deep discharge (below 2 V) tests were conducted at a current density of 10 mA/g.

4.3 Results and Discussion

4.3.1 Crystal Chemistry

The doped $LiMn_{1.5}Ni_{0.42}M_{0.08}O_4$ (M = Cr, Fe, Co, Cu, Al, and Ga) samples will be hereafter referred to by their dopant ion and synthesis temperature (900 °C for the as-prepared samples or 700 °C for the post-annealed samples), *e.g.*, Cr900, Cr700, etc. The XRD patterns of the doped and Mn-rich samples are shown in Figure 4.1. All samples are primarily composed of the cubic spinel phase; a trace amount of the rock-salt impurity $Li_xNi_{1-x}O$ is present in the doped Cu900 and undoped $LiMn_{1.5}Ni_{0.5}O_4$ samples.

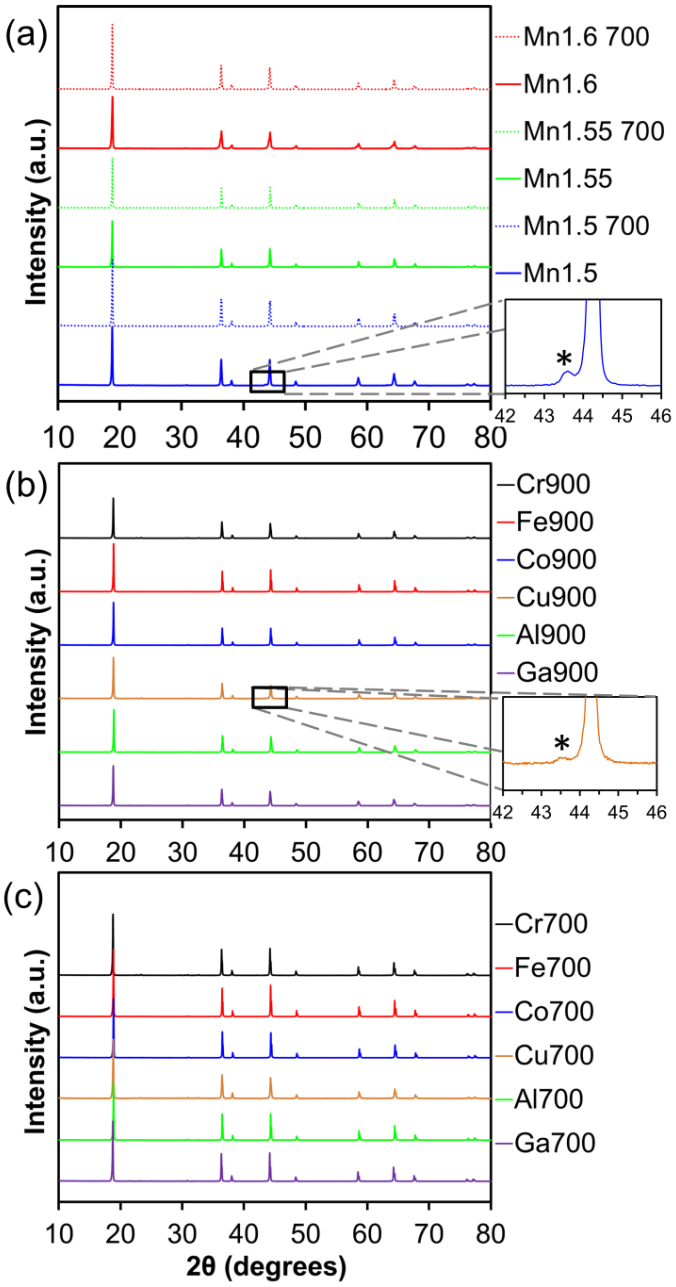

Figure 4.1 XRD Patterns of $LiMn_{1.5}Ni_{0.42}M_{0.08}O_4$ (M = Cr, Fe, Co, Cu, Al, and Ga) (a) synthesized at 900 °C and (b) annealed at 700 °C as well as (c) Mn-rich $LiMn_{1.5+x}Ni_{0.5-x}O_4$ (x = 0, 0.05, and 0.1). Insets show the most prominent rock-salt-phase peak at 43.5° in the undoped $LiMn_{1.5}Ni_{0.5}O_4$ and Cu-doped $LiMn_{1.5}Ni_{0.42}Cu_{0.08}O_4$ samples synthesized at 900 °C.

4.3.2 Magnetic Interactions

Atomically ordered $LiMn_{1.5}Ni_{0.5}O_4$ adopts a ferrimagnetically ordered spin structure below the Curie temperature in which the Mn^{4+} spins align antiparallel to the Ni^{2+} spins, yielding a theoretical net magnetization of 3.5 μ_B for each formula unit.[29] Because Li^+ is not magnetic, but Ni^{2+} and Mn^{4+} are, any magnetic interactions between the 8a tetrahedral sites (A-sites) and the 16d octahedral sites (B-sites) are ignored and the B-B interactions are solely of interest here.

The geometry of the cubic spinel structure creates a competition between interatomic metal-metal interactions through direct overlap of the t_{2g} orbitals and oxygen-mediated superexchange through 90° t_{2g} - O:$2p_{\pi\sigma}$ - e_g pathways. High-spin Ni^{2+} holds two unpaired electrons in the e_g orbitals, while Mn^{4+} has three unpaired electrons in the t_{2g} orbitals. One might expect the interaction between Mn^{4+} ions to favor antiferromagnetic (AF) order due to the direct t_{2g}-t_{2g} interaction between two unpaired electrons, but in fact it appears that the Mn^{4+}:t_{2g}^3 - O:$2p_{\pi\sigma}$ - Mn^{4+}:e_g^0 ferromagnetic (F) interaction dominates, presumably because the overlap integral between the t orbitals is too small to compete with the AF Ni^{2+} - Mn^{4+} interactions.[29] Likewise, the Ni^{2+}:e_g^2 - O:$2p_{\pi\sigma}$ - Mn^{4+}:t_{2g}^3 virtual electron transfer from the Ni^{2+} to the Mn^{4+} dictates that the interaction between the two is antiferromagnetic. The t_{2g}-t_{2g} overlap between the full Ni^{2+}:t_{2g}^6 orbitals and half-filled Mn^{4+}:t_{2g}^3 orbitals are ferromagnetic, but too weak to dominate the stronger antiferromagnetic interaction. Thus, if it is assumed that a structure where Ni^{2+} is primarily coordinated with Mn^{4+} ions, as in the ordered $P4_332$ $LiMn_{1.5}Ni_{0.5}O_4$ spinel, the ferrimagnetic magnetization is characterized by an overall magnetic moment of 3.5μ_B per formula unit (or per Li^+).

If there exists an excess Mn (> 1.5) in the spinel structure or a non-magnetic trivalent cation is substituted for the divalent Ni^{2+}, some Mn^{4+} will be reduced to Mn^{3+} to

maintain charge neutrality. High-spin Mn^{3+} contains a single unpaired electron in the e_g orbital, so the π-σ 90° pathway between Mn^{4+} and Mn^{3+} ions becomes antiferromagnetic, and the antiferromagnetic direct t_{2g} - t_{2g} overlap is retained. As a result, the spins on the Mn^{3+} ions will align antiparallel to the Mn^{4+} spins and parallel to the Ni^{2+} spins. The resulting modification to the overall magnetic moment can be computed as follows:

$$M(\mu_B / fu) = gS_{Mn^{4+}} N_{Mn^{4+}} - gS_{Ni^{2+}} N_{Ni^{2+}} - gS_{Mn^{3+}} N_{Mn^{3+}} \quad (1)$$

where g is the electron gyromagnetic factor (~ 2), S is the total spin of the d-electrons on the ion indicated by the subscript and N_{ion} is the number of such ions in the formula unit (*fu*). In this manner, the Mn^{3+} content of each sample not containing a magnetic dopant ion can be calculated from the saturation magnetization.[29] Certain dopant ions are non-magnetic (Co^{3+}, Al^{3+}, and Ga^{3+}); therefore, their magnetic interactions with Ni^{2+}, Mn^{3+}, and Mn^{4+} are non-existent and may be neglected. Cr^{3+}, Fe^{3+}, and Cu^{2+}, on the other hand, contain at least one unpaired electron and so contribute to the overall magnetization in the ferrimagnetic phase.

Considering the relatively low concentration of the dopant ions (~ 4%), it is reasonable to ignore the dopant-dopant magnetic interactions and to concentrate primarily on the interaction between the dopant and Mn^{4+} ions since Mn^{4+} is the most common ion in the high-voltage spinel. Additionally, the dopant ions are likely to repel each other at high temperature and coordinate primarily with Mn^{4+} ions to lower the electrostatic energy of the lattice. If the assumption is made that the vast majority of the dopant ions will coordinate in this manner in the material, it can also be assumed that all dopant ion spins will be aligned in the same direction below T_C. A modified version of equation 1, which includes the contribution of the magnetic dopants, can then be given as:

$$M(\mu_B / fu) = gS_{Mn^{4+}} N_{Mn^{4+}} - gS_{Ni^{2+}} N_{Ni^{2+}} - gS_{Mn^{3+}} N_{Mn^{3+}} - gS_{M^{n+}} N_{M^{n+}} \quad (2)$$

where M^{n+} is the dopant ion and n is the oxidation state of the dopant ion.

The octahedral Cu^{2+} ion having a $t_{2g}^6e_g^3$ configuration can be expected to substitute for Ni^{2+}, and with one unpaired electron in the e_g orbital, it can be assumed that Cu^{2+} will behave similar to Ni^{2+} and its S = 1/2 spin aligns antiparallel to the spin of the Mn^{4+} ions owing to a π-σ 90° superexchange. On the basis of both direct t_{2g}-t_{2g} and t_{2g} - O:$2p_{\pi\sigma}$ - e_g overlaps, Fe^{3+} should align antiparallel to Mn^{4+} because the virtual charge transfer from Fe^{3+} to Mn^{4+} dominates that from Mn^{4+} to Fe^{3+}.

The Cr^{3+} ion has the same d^3-electron configuration as Mn^{4+}, so one might expect the Cr^{3+} spin to align in the same direction as that of Mn. However, the calculated Mn^{3+} content under this assumption is 0.23, which is larger than the value obtained from the electrochemical data (0.18). A much better fit to the electrochemical data is obtained when the spin on the Cr^{3+} ions is assumed to be antiparallel to that of the Mn^{4+} ions. An antiferromagnetic exchange between Cr^{3+} and Mn^{4+} is reasonable and can be explained as follows: because Cr has a smaller nuclear charge than Mn, the electron orbitals are extended further (alternatively, Cr^{3+} is larger in size than Mn^{4+}). The implication is that the direct t_{2g}-t_{2g} interaction between a Cr^{3+} and Mn^{4+} would have a much larger magnitude than the interaction between two Mn^{4+} ions, large enough to make the antiferromagnetic exchange between the two half-filled t_{2g} orbitals dominant over the t_{2g} - O:$2p_{\pi\sigma}$ - e_g superexchange, as is the case of λ-MnO_2.[72] In this situation the 3/2 spin on the Cr^{3+} would align antiparallel to the majority spin direction of the Mn^{4+} ions. Nevertheless, it is entirely possible that some Cr^{3+} spin may be aligned parallel to the Mn^{4+} spin depending on the number of coordinated Ni ions (the Cr: t_{2g} - O:$2p_{\pi\sigma}$ - Ni:e_g exchange is antiferromagnetic). This uncertainty is recognized and noted in Table 4.1.

Table 4.1 Magnetization, Mn^{3+} content, lattice parameter, 2.7 V capacity, and Curie temperature of $LiMn_{1.5}Ni_{0.42}M_{0.08}O_4$ (M = Cr, Fe, Co, Cu, Al, and Ga) and $LiMn_{1.5+x}Ni_{0.5-x}O_4$ ($0 \leq x \leq 0.1$) samples prepared at 900 °C and after post-annealing at 700 °C. The Curie temperature is taken as the inflection point of the temperature dependent magnetic susceptibility curve.

Sample	Magnetization (μ_B/FU)	Mn^{3+} content (magnetic)	Mn^{3+} content (electrochemical)	Lattice constant (Å)	2.7 V Capacity (mAh/g)	T_c (K)
Cr900	2.26 (3)	0.17 (6)	0.18	8.188 (1)	69	94 (2)
Co900	2.26 (4)	0.20 (1)	0.18	8.178 (2)	51	95 (2)
Fe900	2.46 (2)	0.11 (1)	0.11	8.183 (1)	82	107 (1)
Cu900	2.79 (2)	0.11 (1)	0.09	8.176 (2)	83	111 (4)
Al900	2.06 (4)	0.23 (1)	0.21	8.185 (2)	54	91 (4)
Ga900	2.11 (3)	0.22 (1)	0.24	8.197 (2)	54	91 (4)
Mn1.5	2.85 (3)	0.15 (1)	0.15	8.175 (1)	54	116 (2)
Mn1.55	2.72 (3)	0.17 (1)	0.19	8.178 (1)	62	119 (3)
Mn1.6	1.92 (5)	0.35 (1)	0.32	8.186 (2)	71	106 (4)
Cr700	2.28 (5)	0.16 (6)	0.18	8.190 (1)	69	95 (2)
Co700	2.57 (3)	0.16 (1)	0.16	8.177 (1)	55	101 (2)
Fe700	2.58 (2)	0.10 (1)	0.11	8.183 (1)	82	110 (1)
Cu700	3.01 (3)	0.08 (1)	0.05	8.175 (2)	100	120 (3)
Al700	2.19 (6)	0.21 (1)	0.24	8.183 (1)	49	93 (2)
Ga700	2.10 (5)	0.22 (1)	0.25	8.194 (1)	60	90 (4)
Mn1.5-700	3.45 (1)	0.01 (1)	0.06	8.174 (1)	67	124 (1)
Mn1.55-700	3.00 (2)	0.11 (1)	0.15	8.177 (1)	84	122 (1)
Mn1.6-700	2.22 (5)	0.28 (1)	0.29	8.187 (2)	87	120 (2)

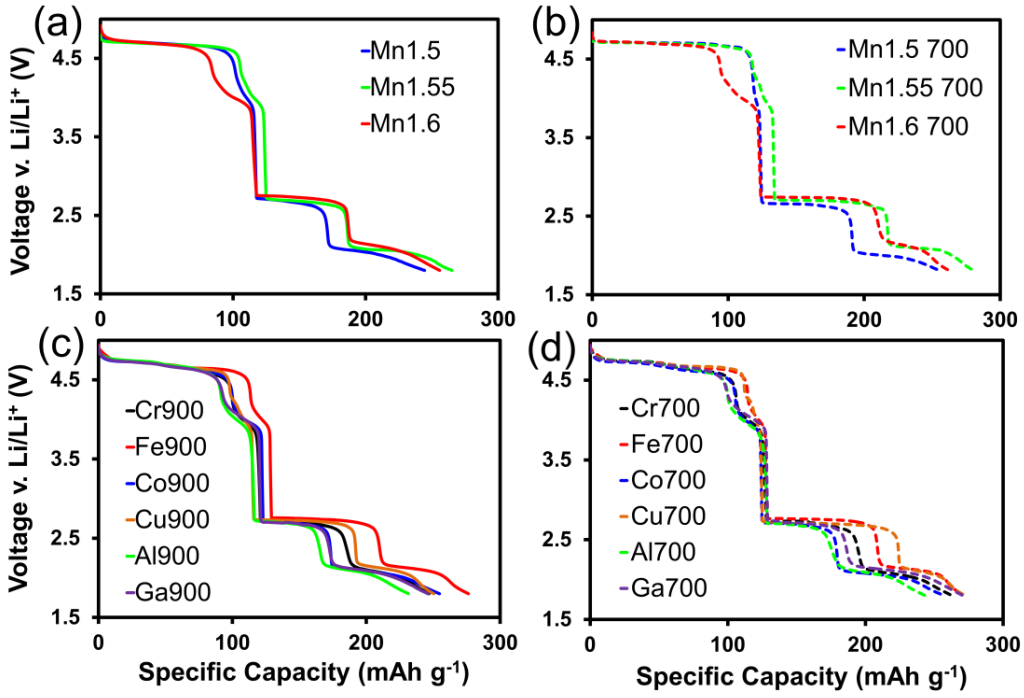

Figure 4.2 First discharge curves of Mn-rich $LiMn_{1.5+x}Ni_{0.5-x}O_4$ (x = 0, 0.05, 0.1) (a) synthesized at 900 °C and (b) annealed at 700 °C and doped $LiMn_{1.5}Ni_{0.42}M_{0.08}O_4$ (M = Cr, Fe, Co, Cu, Al, and Ga) (c) synthesized at 900 °C and (d) annealed at 700 °C.

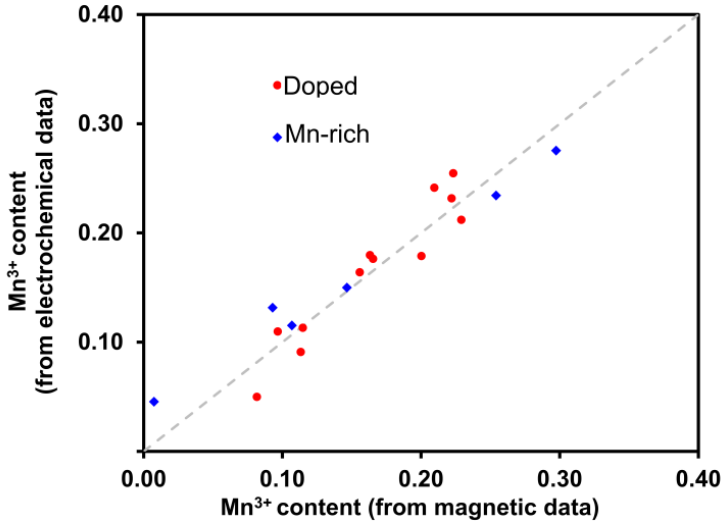

Figure 4.3 Relationship between Mn^{3+} content determined by saturation magnetization (from magnetic data) and Mn^{3+} content determined by the 4 V capacity (from electrochemical data).

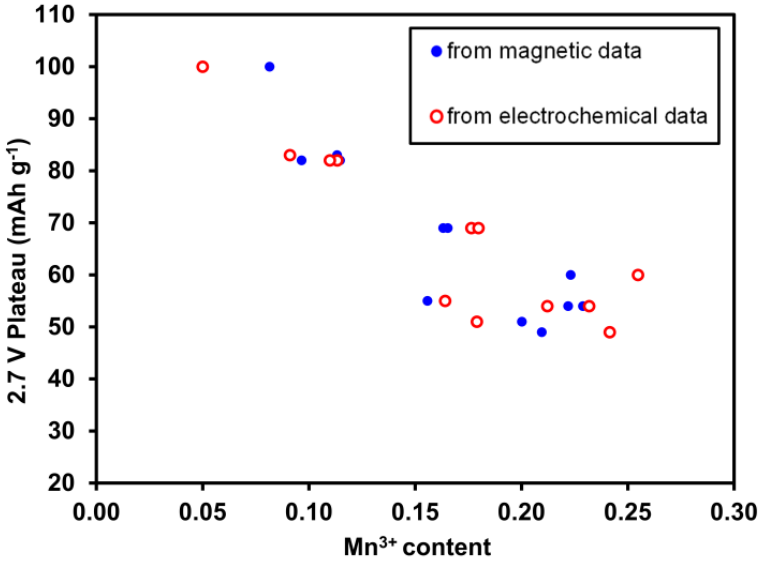

Figure 4.4 Relationship between 2.7 V capacity and Mn^{3+} content for $LiMn_{1.5}Ni_{0.42}M_{0.08}O_4$ (M = Cr, Fe, Co, Cu, Al, and Ga).

Table 4.1 shows the calculated Mn^{3+} contents of all the doped and Mn-rich samples by Equation 2 (where Mn^{3+} content is the stoichiometric amount of Mn^{3+} ions per formula unit). The values of N_{ion} for the doped samples were such that the total amount of Mn was 1.5/*fu*. For the Mn-rich samples, the Mn^{4+} and Mn^{3+} contents would sum to equal 1.5, 1.55, and 1.6. The results from the magnetization study are compared with the electrochemical data of Li-ion cells. Figure 4.2 displays the first discharge of the doped samples down to 1.8 V. Because the $Mn^{3+/4+}$ couple in the high-voltage spinel is centered around 4 V and no other Faradaic process occurs at that potential (except for the $Cu^{2+/3+}$ couple at ~ 4.2 V), the Mn^{3+} content can be estimated by comparing the capacity in the 4 V region to the overall capacity. It can be seen in Figure 4.3 that the Mn^{3+} values match very closely, validating that saturation magnetization is a useful metric for estimating the amount of Mn^{3+} present in a wide variety of doped or undoped high-voltage spinel samples.

4.3.3 Electrochemical Voltage Profiles

Another useful quantity to be derived from the electrochemical discharge curves is the capacity in the ~ 2.7 V region when the cells are subjected to deep discharge. This capacity corresponds to the insertion of an additional lithium ion into the 16c octahedral sites of the spinel lattice, which are normally empty in the $Li[Mn_{1.5}Ni_{0.5}]O_4$ spinel.[91] As lithium is inserted into the 16c octahedral sites, a two-phase reaction proceeds in which Mn^{4+} is reduced to Mn^{3+}, fostering a Jahn-Teller induced tetragonal distortion of the cubic spinel structure. Recently it was shown that a second tetragonal spinel phase forms while under load as a result of an additional distortion associated with Li insertion.[92] When this second tetragonal phase develops, the discharge voltage is decreased from 2.7 V to ~ 2 V vs. Li/Li^+. It so happens that the ordered spinel structure with the $P4_332$ symmetry possesses larger 16c octahedral sites than the *Fd*-3*m* phase owing to the preferential ordering of the Mn^{4+} and Ni^{2+} ions. Because the ordered-spinel regions accommodate Li ions preferentially in their larger 16c sites, isolated ordered regions have the Mn^{3+} concentration needed for a cooperative room-temperature Jahn-Teller distortion before the disordered matrix in which they are embedded. Tetragonal regions in a cubic matrix create a stress on the tetragonal phase that limits the magnitude of its c/a ratio. However, at a certain onset Li concentration, the disordered regions also have a high enough Mn^{3+} concentration to participate in the cooperative Jahn-Teller distortion, thus relieving the stress to allow the larger tetragonal $c/a > 1$ of the Li-rich phase. This onset can be visualized as a sudden change in voltage from 2.7 to 2.0 V in the deep-discharge curves. Therefore, the highly ordered spinel samples with a higher volume of atomically ordered regions exhibit a larger capacity in the 2.7 V region than the disordered samples.[92] This technique has already been used to determine the degree of cation order of a few doped high-voltage spinel samples synthesized in a different manner.[93] Thus, the

2.7 V plateau serves as a means of semi-quantitatively assessing the degree of cation order in high-voltage spinels with similar compositions.

The deep-discharge curves of the series $LiMn_{1.5+x}Ni_{0.5-x}O_4$ with x = 0, 0.05, 0.1, synthesized at 900 °C and also annealed at 700 °C (to promote the ordered phase) are shown in Figure 4.2(b). From here on, the Mn-rich samples will be denoted by the atomic symbol for manganese followed by the manganese content of the sample. If the sample has been annealed at 700 °C, these annotations will be followed by the number 700, *e.g.,* Mn1.6, Mn1.6-700, etc. Two notable trends are visible from these data concerning the 2.7 V capacity: it increases significantly as the Mn content is increased or after the material has been annealed at 700 °C. Another noticeable piece of information is that the Mn1.6 sample has a larger 2.7 V capacity than the Mn1.5-700 sample. In this case, distinguishing the degree of ordering via the 2.7 V method is difficult due to the difference in Mn^{3+} content between the two samples. It is reasonable to assume that this difficulty also applies to the doped samples, which display a wide-ranging variation of Mn^{3+} content, from 0.08 to 0.23.

There are several explanations as to why an increase in the Mn^{3+} content is associated with an increase in the 2.7 V plateau in the Mn-rich samples. The most basic explanation concerns the unit cell volume and the size of the empty octahedral sites. Because the Mn^{3+} ion is much larger than Mn^{4+} ions owing to the extra electron in the e_g orbital, samples with a higher Mn^{3+} content tend to have a larger lattice parameter. This is evident in the data presented in Table 4.1. A more expanded unit cell volume will result in larger octahedral sites, resulting in less stress on the structure during Li insertion and thus delaying the onset of the second tetragonal phase associated with the 2.0 V plateau. It is also possible that mobile Mn^{3+} ions are attracted to the ordered phase upon insertion of lithium into the octahedral sites in an effort to foster cooperative Jahn-Teller distortion.

The ordered phase, with the larger 16c sites, will fill with Li before the disordered phase. The elastic strain energy of a tetragonal phase enclosed by a cubic phase can be reduced if Jahn-Teller ions surround the tetragonal phase and participate in the distortion. In this manner, the strain energy cold be relieved and the 2.7 V plateau extended. Thus, the two parameters that appear to govern the 2.7 V plateau length, Mn^{3+} content and the degree of order, both extend the 2.7 V plateau. However, the contribution of the degree of order to the 2.7 V capacity appears to be more significant than the contribution by the expanded cell volume due to higher Mn^{3+} content. This is evidenced by Figure 4.4, which shows that a reliable trend exists among the doped samples in which the 2.7 V plateau increases with decreasing Mn^{3+} content, indicating that the degree of order may be the dominant factor in determining the 2.7 V capacity.

4.3.4 T_C as an Indicator of Atomic Order

It has been suggested that the DC susceptibility provides a reliable means of investigating magnetic clustering of the high-voltage spinels with the implication that magnetic clustering is directly related to the degree of long-range order.[38,41] While previous work has approached the subject, an in-depth qualitative study of multiple samples comparing the DC susceptibility curve and the degree of cation ordering has not been established. The field-cooled DC susceptibility curves for the doped compositions can be seen in Figure 4.5. The ferrimagnetic ordering temperature (T_C) can be identified easily by the sharp change in susceptibility around 90 – 125 K. Such a large variation in T_C reflects the existence of structural and compositional differences among the samples. The magnetic ordering temperature of a variety of materials can commonly be affected by a range of parameters, including dopant concentration and heat treatment as is the case with Si-doped cobalt ferrite.[94]

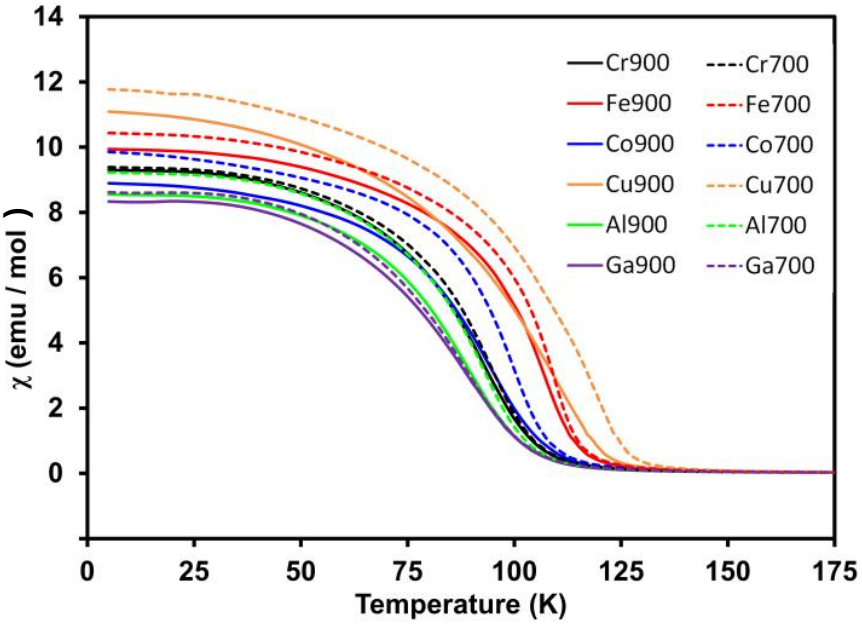

Figure 4.5 Variation of DC magnetic susceptibility with temperature of $LiMn_{1.5}Ni_{0.42}M_{0.08}O_4$ (M = Cr, Fe, Co, Cu, Al, and Ga).

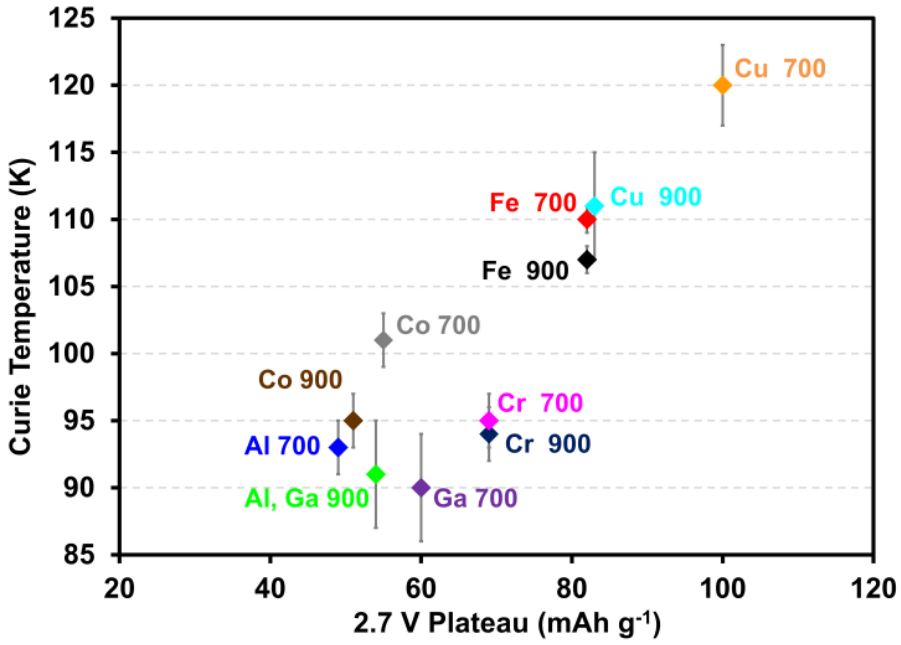

Figure 4.6 Relationship between 2.7 V capacity and the Curie temperature for $LiMn_{1.5}Ni_{0.42}M_{0.08}O_4$ (M = Cr, Fe, Co, Cu, Al, and Ga).

It has already been suggested that the T_C of $LiMn_{1.5}Ni_{0.5}O_4$ is higher when the material possesses a high degree of cation order.[29,38,41] It follows that a more disordered structure, possessing a wide variation in local composition, will have a more gradual magnetic transition with a lower Curie temperature. It has also been suggested that different dopant ions will induce a different amount of cation disorder in high-voltage spinels.[93] Thus, measuring the T_C can be practically applied as a way to determine the relative degree of cation order among a group of materials with similar compositions.

The Curie temperatures of the Mn-rich samples are listed in Table 4.1. All of the annealed samples possess a higher T_C than their unannealed counterparts, consistent with the understanding that annealing promotes cation ordering and that ordered materials maintain higher Curie temperatures. The more uniform distribution of Mn and Ni in the ordered structure prevents excessive Mn^{4+} - Mn^{3+} and Mn^{3+} - Mn^{3+} interactions, which can cause frustration as in the case of $LiMn_2O_4$.[95] By virtue of the fact that T_C is lowered by magnetic frustration and that a more ordered high-voltage spinel is typically less frustrated than the disordered form, a qualitative connection can be made between the degree of cation order in high-voltage spinels and the measured value of the Curie temperature.

Figure 4.6 shows the qualitative relationship between T_C and the 2.7 V capacities of the doped samples. This relationship can be identified based on the correlation between Mn^{3+} and the 2.7 V plateau as previously discussed (Figure 4.4). At first glance, it would seem that the T_C is strictly dependent on the Mn^{3+} content of each sample based on the strong correlation seen in Figure 4.4. However, since Mn^{3+} content and the degree of cation ordering typically go hand-in-hand, sometimes it is difficult to isolate the effects of the two. Figure 4.7 compares the Mn^{3+} content and T_C with the 2.7 V capacity for the Mn-rich samples, but no clear correlation is seen. This is to be expected considering the

wide variation of Mn content in each sample based on the arguments presented earlier. However, it is clear that the annealing process increases the T_C and the 2.7 V capacity while decreasing the Mn^{3+} content in every case. It is important to note that the Mn1.6 sample, while expected to have more disorder than the Mn1.5-700 sample, has a larger 2.7 V capacity. In this case, the T_C provides a much better idea of the relative degree of cation ordering between the two samples.

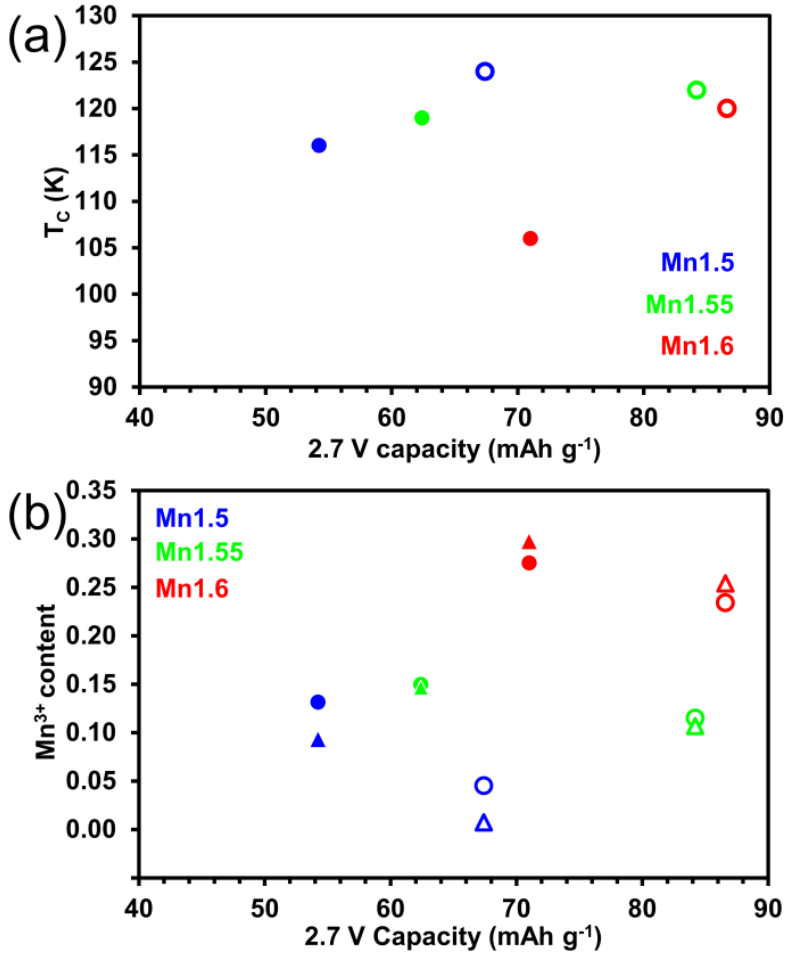

Figure 4.7 Correlation of 2.7 V capacity with (a) Mn^{3+} content and (b)T_C for the Mn-rich $LiMn_{1.5+x}Ni_{0.5-x}O_4$ (x = 0, 0.05, 0.1) samples. Solid and open symbols refer, respectively, to 900 and 700 °C samples. In (b), circles and triangles refer, respectively, to data from electrochemical and magnetic measurements.

As noted earlier among the doped samples, however, a clear trend exists in which the 2.7 V plateau increases as the Mn^{3+} content decreases, a trend which is exactly opposite to that in the Mn-rich samples. In this case it must be assumed that the degree of ordering, which depends heavily on the nature of the dopant ion, has a more pronounced effect on the 2.7 V capacity than the Mn^{3+} content.

Among the doped samples, it is easy to discern that the most ordered sample of the group is Cu-700, having both the highest T_C and largest 2.7 V capacity as well as the smallest amount of Mn^{3+}. The Cu doped compound is in fact the only doped sample to display a change in T_C and 2.7 V capacity upon annealing to a comparable extent as the undoped Mn-rich materials. This result is not surprising, considering the similarity between the valence and ionic radii of Cu^{2+} and Ni^{2+} ions, allowing Cu to behave in much the same manner as Ni. Therefore, the ability of the Cu-doped samples to order atomically at 700 °C is similar to that of the undoped samples.

On the opposite end of the spectrum, the Al and Ga samples are characterized by both the lowest Curie temperatures and the smallest 2.7 V capacities. The fact that neither the 2.7 V capacity nor the T_C change by a significant amount after annealing implies that the Al and Ga dopants provide an effective means of inhibiting cation ordering, with the consequence that these materials are highly disordered.

As in the case of Al and Ga, replacing some Ni with Cr appears to prevent the spinel from ordering; the Cr-900 and Cr-700 samples possess the same T_C, 2.7 V capacity, and Mn^{3+} content. Based on the Curie temperature, one would expect the Cr-doped samples to be less ordered than the Co-doped counterparts. However, the 2.7 V capacities imply just the opposite. Cr900 and Cr700 are characterized by larger lattice parameters (8.188 Å and 8.190 Å, respectively) compared to the Co900 (8.178 Å) and Co700 (8.177 Å) samples, which may explain the discrepancy. The 2.7 V capacities of

the Cr-doped samples may be larger than those of Co900 and Co700 not because of a higher degree of cation order, but because the larger lattice volume of the Cr-doped samples delays the onset of the strain-induced tetragonal distortion. Based on the T_C, it would appear as though the Cr-doped samples are similarly ordered as the Co900 sample.

Among the trivalent doped samples (Cr, Fe, Co, Al, and Ga), the Fe-doped sample stands out as the most ordered, possessing both the highest Curie temperature and 2.7 V plateau length. It is found that upon annealing, the T_C increases slightly implying that the Fe-700 sample is only marginally more ordered than the Fe-900 sample. The saturation magnetization shows the Mn^{3+} concentration also decreases slightly, which may explain why the 2.7 V capacity is nearly identical for the two samples.

Interpretation of the data for the Co-doped sample is made complicated by the following: (i) The Co^{3+}/Co^{2+} redox energy is only a little below the Mn^{4+}/Mn^{3+} energy so that the $Co^{2+} + Mn^{4+} = Co^{3+} + Mn^{3+}$ equilibrium is biased more strongly to the right with increasing temperature. (ii) The low-spin (LS) Co^{3+} state transforms increasingly to an intermediate spin (IS) state with increasing temperature, and this transition is biased in the presence of a cooperative Jahn-Teller distortion on the Mn^{3+} ions because IS Co^{3+} is also a strong Jahn-Teller ion.

4.4 CONCLUSION

With an aim to develop a better understanding of the complex and often confusing roles of cation ordering and Mn^{3+} content on the electrochemical properties of the high-voltage $LiMn_{1.5}Ni_{0.5}O_4$ spinel cathodes, magnetic measurements have been pursued as a viable tool. The saturation magnetization provides a reliable means of calculating the Mn^{3+} content in the doped samples, as confirmed by the electrochemical capacity data. It is found that among the doped samples, the T_C increases with increasing 2.7 V plateau length and decreasing Mn^{3+} content, both of which are indicative of higher degrees of

cation order. Thus, the Curie temperature of doped or Mn-rich high-voltage spinel samples may be a useful metric for qualitatively determining the degree of cation order among samples with very different Mn^{3+} contents. This is important because it has been shown in the literature to be a factor in controlling the performance of the samples as cathodes in Li-ion batteries.

Chapter 5: Electronic and Electrochemical Properties of $Li_{1-x}Mn_{1.5}Ni_{0.5}O_4$ Spinel Cathodes as a Function of Lithium Content and Cation Ordering

5.1 Introduction

A very interesting property of $LiMn_{1.5}Ni_{0.5}O_4$ is that its electrochemical performance, and the rate performance in particular, seems to be governed by the atomic arrangement of Mn and Ni ions in the structure.[39,44,81,96] It comes in two flavors, the so called "disordered" spinel of the *Fd*-3*m* space group and the "ordered" spinel with $P4_332$ symmetry. In the disordered variety, Mn and Ni ions are more or less randomly distributed in the 16d octahedral sites whereas in the ordered unit cell, Mn is assigned to 12b and Ni to 4a octahedral sites.

Several theories have been put forward to explain this phenomenon, the most popular of which are: (i) disordered spinel exhibits a wide range of solid-solution lithium insertion, whereas the ordered spinel displays two-phase behavior; this interphase boundary limits lithium diffusion and is responsible for the poor rate capability;[81,97–99] and (ii) the disordered spinel tends to have some initial Mn^{3+}, leading to higher electronic conductivity and thus greater rate capability.[40]

Both of these theories have been widely accepted by the community, but there are several complications and inconsistencies present in the literature; some authors are challenging these notions. For instance, there exist reports on compounds with two-phase behavior and very good rate capability.[39,100,101] These studies also found no direct correlation between Mn^{3+} content and rate performance.[39,100]

Z. Moorhead-Rosenberg, Ashfia Huq, John B. Goodenough, & A. Manthiram. Electronic and electrochemical properties of $Li_{1-x}Mn_{1.5}Ni_{0.5}O_4$ spinel cathodes as a function of lithium content and cation ordering. *(Submitted, Chemistry of Materials, 2015).* . Ashfia Huq was the neutron beamline operator and helped with refinement. J.B. Goodenough provided insights and A. Manthiram supervised the project.

One of the most cited articles on the conductivity of high-voltage spinel reports only the conductivity of the spinel in the fully lithiated state.[40] This value will be almost entirely dependent on the Mn^{3+} content in the as-prepared sample since Mn^{3+} is the electronic charge carrier. To date, no work has shown the conductivity of $Li_{1-x}Mn_{1.5}Ni_{0.5}O_4$ throughout the entire range of lithium content, although preliminary results show what happens to the conductivity at high lithium contents ((1-x) > 0.8).[102] Understandably, the conductivity drops noticeably when the Mn^{3+} is all oxidized to Mn^{4+}. For most of the charge/discharge cycle, $Ni^{2+/3+}$ and $Ni^{3+/4+}$ ions are the active charge carriers and there is no Mn^{3+} present in the material. Investigation of how the conductivity changes after all Mn^{3+} has been oxidized is the motivation behind this study. The primary focus of this article is the examination of the electronic properties of the high-voltage spinel as a function of lithium content and cation ordering since this landscape has not yet been explored. X-ray diffraction is used to determine the lithiation/delithiation mechanism, *i.e.*, solid solution vs. two-phase, and the rate performance of the high-voltage spinels is correlated with these observed structural and electronic data.

5.2 EXPERIMENTAL

The high-voltage spinel of composition $LiMn_{1.5}Ni_{0.5}O_4$ was synthesized via a continuously stirred tank reactor (CSTR) co-precipitation technique as described previously.[103] Thermogravimetric analysis was used to determine the water content of the metal hydroxide precursors and calculate the required stoichiometric ratio of $LiOH{\cdot}H_2O$. Ground mixtures of the mixed metal hydroxide precursors and $LiOH{\cdot}H_2O$ were fired at 900˚C for 8 h in a tube furnace and cooled to room temperature at a rate of 1.5˚C per minute. For neutron diffraction studies, an identical mixture was made using a $^7LiOH{\cdot}H_2O$ precursor to minimize absorption of neutrons from ^6Li.

The composition $LiMn_{1.5}Ni_{0.5}O_4$ was subjected to four different heat treatments to induce different degrees of cation ordering. The first, called "slow cooled" or hereafter referred to as "SC", was prepared using the heat treatment described above (1.5˚C per minute cooling from 900 ˚C). From the same batch, a "fast cooled sample" (FC) was heated to 900˚C for 8 h and then cooled at 5˚C per minute. The sample labeled A48 was annealed for 48 h at 700˚C while the sample A240 was annealed for 240 h at 700˚C.

Delithiation was carried out chemically with NO_2BF_4 (Matrix Scientific) in anhydrous acetonitrile solution. For each delithiated sample, the proper amount of NO_2BF_4 was weighed out in an argon filled glovebox and added to a round-bottom flask with the spinel powder. The flask was then covered with an air-tight septum and taken to a fume hood, where anhydrous acetonitrile was injected into the flask and stirred overnight. After the delithiation reaction took place, each sample was washed by centrifuge with acetonitrile thrice and acetone once and then dried at 100˚C for approximately 1 h. Lithium contents of the delithiated samples were then measured with a Varian inductively coupled – optical emission spectrometer (ICP-OES).

Conductivity measurements were made with a Solartron AC impedance analyze. For a routine measurement, a small amount of delithiated spinel powder was loaded into the center of a paper annulus approximately 1 mm thick. The annulus, with the powder inside, was then attached to a K-type thermocouple and placed between two cylindrical tungsten carbide dies. Leads to the Solartron were then attached to these dies. The die assembly was then placed in a press with heating plates on each side and compressed to forces of 2, 4, 6, 8, and 10 tons, corresponding to a maximum pressure of ~ 500 MPa. AC impedance spectra were taken at each loading. At the maximum pressure, the heating plates were turned on while the sample temperature and impedance at 1 Hz were measured. A frequency of 1 Hz was chosen to approximate DC conditions.

Powder X-ray diffraction (XRD) was carried out with a Rigaku Ultima IV diffractometer with Cu K-alpha radiation from 2θ = 15˚ to 80˚ and a step size of 0.02˚. Neutron diffraction experiments were performed at the POWGEN diffractometer, beamline 11A, at the Spallation Neutron Source at Oak Ridge National Laboratory. Rietveld refinement was performed with GSAS/EXPGUI and FullProf. Diffraction peak full-width half-maximum values were calculated in Excel using the data from FullProf refinements. FTIR measurements were made with a Thermo Scientific Nicolet iS5 with a KBr window. Magnetic measurements were performed with a Quantum Design Physical Property Measurement System () with vibrating sample magnetometer (VSM) attachment. Seebeck coefficient values were obtained with a homebuilt apparatus with a liquid nitrogen cooling source. Contacts on each side of the specimen were heated such that the temperature difference was 4 K.

Electrode slurries were prepared by mixing 80 wt. % active material, 10 wt. % Super P conductive carbon, and 10 wt. % PVDF binder in an NMP solution by magnetic stirring overnight. Slurries were cast onto an aluminum foil with a doctor blade technique such that the active material loading was ~5 mg cm^{-1} and dried overnight in a vacuum oven at 130˚C. Electrodes were calendared and punched into 1 cm disks and assembled in coin cells in an argon filled glovebox. Celgard polypropylene separators and a 1 M $LiPF_6$ in EC:DEC (1 : 1 by volume) electrolyte (BASF) were used. Lithium foil acted as the counter and reference electrode. Electrochemical cycling and rate performance were analyzed with an Arbin cycler from C/10 to 20C rate (1C = 146 mA g^{-1}).

5.3 Results and Discussion

5.3.1 Rationale

With any material, the most desirable specimens for measuring electronic properties are large single crystals to which leads can be directly attached. So far, growth of a single crystal of $LiMn_{1.5}Ni_{0.5}O_4$ large enough to examine has been elusive; pellets have been the specimen of choice for researchers trying to understand this material. The difficulty with pellets is that they must be sintered at high temperature for the grains to grow together. For materials which are not stable at high temperatures, such as the delithiated spinel, this route is not feasible. Delithiating sintered pellets also poses its own challenges; the pellets tend to crack due to high stress associated with non-uniform lattice contraction from lithium concentration gradients even when delithiation was carried out at very slow rates (C/300 rate).[102]

It is by the above logic that the specimens used for conductivity measurements in this study consist of compacted powder pressed at moderate pressures between two tungsten carbide dies. These kinds of resistivity measurements have been performed on oxide powders before, so this technique is not without precedent.[104,105] Four-probe measurements are thus difficult to accomplish, but 2-probe AC impedance can easily be used. AC impedance spectroscopy offers the advantage over DC measurements that the contribution to resistance from grain boundaries can be easily deduced by looking at the impedance frequency response.[106,107] Spectra of homogenous granular samples are manifest as two arcs in the real/imaginary impedance plane; the high frequency arc represents the bulk internal resistance whereas the lower frequency arc corresponds to the contribution from grain boundary resistance.[107] With a compacted powder sample, one would expect the grain boundary resistivity to be high, but the large micron-sized particles and the intrinsically high measured resistivity of $LiMn_{1.5}Ni_{0.5}O_4$ mean that the

grain boundary resistance is much lower than the bulk resistance, and its contribution to the overall resistivity is very small. This explanation is evidenced by very small or non-observable high-frequency impedance arcs. An example impedance measurement is shown in Figure B1 in Appendix B. The "cold-pressed" powder pellets also allow for the ability to measure the Seebeck coefficient of delithiated spinels, critical to the understanding of electronic properties at various lithium contents. A diagram of the experimental setup is displayed in Figure 5.1.

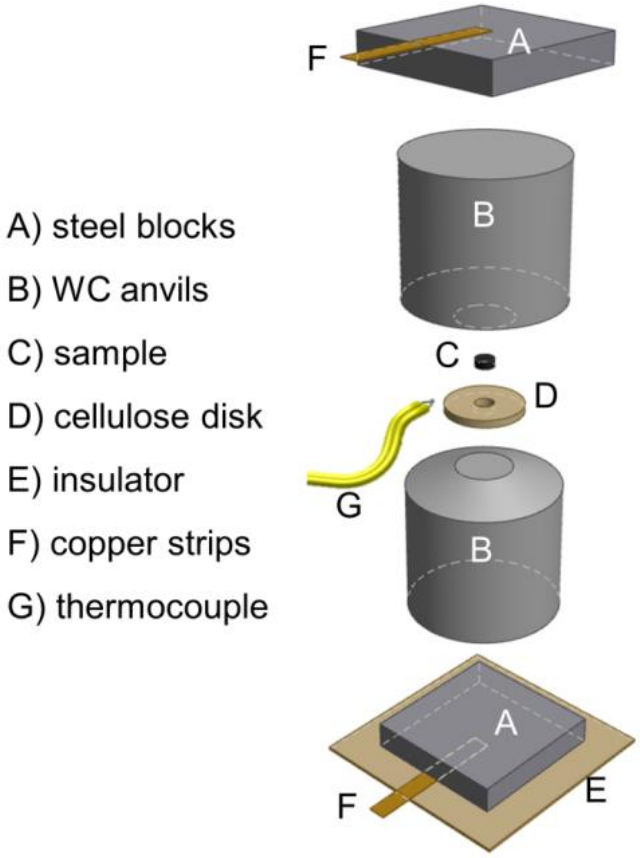

Figure 5.1 Schematic representation of experimental setup for AC impedance measurements.

5.3.2 Cation Ordering

While $LiMn_{1.5}Ni_{0.5}O_4$ spinel takes on two distinct phases, disordered *Fd*-3*m* and ordered $P4_332$, the prepared samples are typically composed of a mixture of the two. This has been shown most reliably with neutron diffraction data since it is difficult to detect Mn/Ni ordering with X-rays.[39] Cation ordering is promoted at 700˚C, and longer annealing times at this temperature result in a spinel sample with a greater fraction of $P4_332$ phase. Kim et al have shown that the fraction of $P4_332$ phase increases significantly in the first 10 hours of annealing, but further increase requires much longer dwell time.[39] It is for this reason that we prepared a sample with a 240 h dwell time at 700˚C. Highly disordered samples can be achieved by heating the powder at 900˚C and cooling the sample quickly through the temperature at which ordering occurs. Although neutron diffraction offers the only quantitative method to determine the ratio of ordered to disordered spinel, other techniques have been employed to look at the degree of cation ordering qualitatively, including FTIR[40,99] and magnetic measurements.[41,42]

Because $P4_332$ and *Fd*-3*m* have slightly different vibrational modes, their infrared absorption spectra will be different. The ratio of the absorption peaks at ~ 588 and 619 cm^{-1} is commonly used as an indicator of atomic order.[99] The more ordered spinel will also have sharper, more clearly defined peaks. The FTIR spectra for the four $LiMn_{1.5}Ni_{0.5}O_4$ samples, FC, SC, A48, and A240, and their delithiated counterparts are shown in Figure 5.2. The black lines represent the spectra of the fully lithiated samples. It is visually clear that the peak at ~ 588 cm^{-1} becomes more pronounced from left to right, indicating that the fast-cooled sample is indeed the most disordered and A240 is the most ordered. The data from the current study are consistent with recently published results.[101] The intensity ratios of 588/619 peaks for each sample are listed in Table 5.1. It is also clear that this cation order is maintained after delithiation – *i.e.*, delithiation does not

encourage rearrangement of the Mn and Ni ions, since peaks at 425, 450, and 475 cm^{-1} become apparent in the annealed samples, presumably from the λ-$Mn_{1.5}Ni_{0.5}O_4$ phase.

Magnetic measurements can also be used to qualitatively determine the degree of cation ordering. Antiferromagnetic superexchange interactions cause $LiMn_{1.5}Ni_{0.5}O_4$ spinel to undergo a ferrimagnetic ordering transition at ~ 120 K. It has been shown that this temperature will be higher for more atomically ordered samples since the Ni^{2+} ions are surrounded completely by Mn^{4+} ions and so there are no antiferromagnetic Ni-Ni exchange interactions - the antiferromagnetic exchange is strictly between Ni-Mn pairs.[42] The inverse magnetic susceptibility of the four $LiMn_{1.5}Ni_{0.5}O_4$ samples is shown in Figure 5.3. The estimated T_C for each sample is listed in Table 5.1. The A240 sample shows the highest T_C and the FC sample shows the lowest, in accordance with the above explanation.

In order to more quantitatively understand the nature of the cation ordering in these spinels, analogues were prepared using ^{7}LiOH precursor material and sent to the 11A SNS beamline at Oak Ridge National Laboratory for neutron diffraction studies. The neutron diffraction patterns of the SC, A48, and A240 samples are shown in Figure 5.4. The gray vertical lines indicate reflections belonging to the $P4_332$ space group. From these data, it can be seen that the SC sample displays no indication of cation ordering, while the A48 and A240 samples clearly possess the $P4_332$ characteristic peaks. It is also clear that these peaks are intensified in the A240 specimen. Rietveld refinement of these patterns indicate that 14% and 8% of the 4b sites (Wyckoff position of Ni in ordered spinel) are occupied by Mn ions in the A48 and A240 spinels, respectively. Details of the refinement in GSAS can be seen in Table B1 and Figure B2 of Appendix B. Analysis of the ordered peak full-width at half-maximum (FWHM) suggest that the ordered-spinel domain size is 44(11)% and 69(10)% of the overall crystallite size, respectively, in A48

and A240 based on selective broadening results from FullProf and the Scherrer formula according to the method of Kim et al.[39] This analysis can be seen in Figure B3 of Appendix B. Based on FTIR, magnetic, and neutron diffraction data, the degree of cation ordering among the samples increases in the order: FC < SC < A48 < A240.

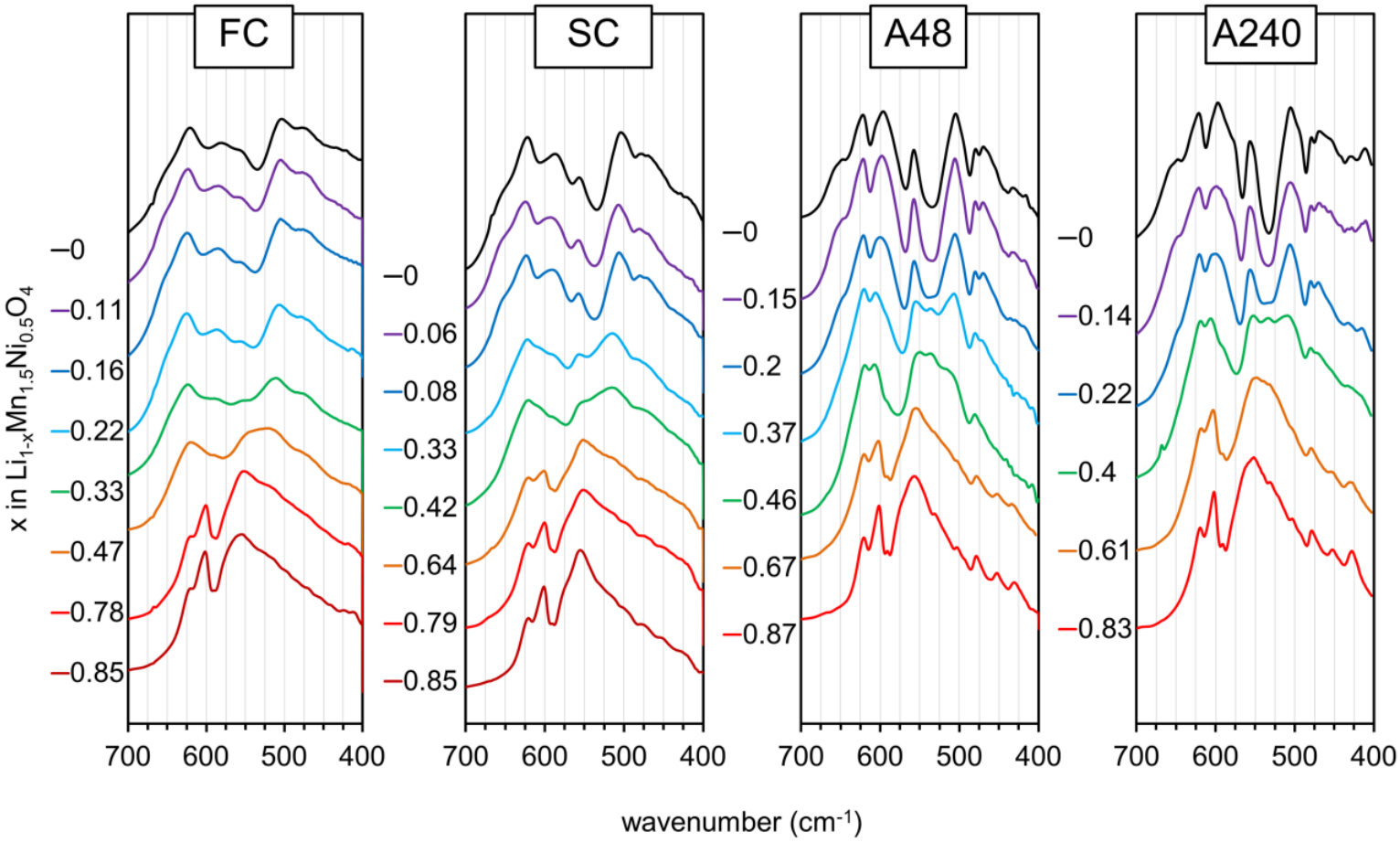

Figure 5.2. FTIR spectra of as-prepared and delithiated spinel specimens. Lithium vacancy content is listed next to each spectrum according to ICP-OES values.

Table 5.1 Properties of $LiMn_{1.5}Ni_{0.5}O_4$ specimens

Sample	Mn^{3+} (electrochemical)	Mn^{3+} (magnetic)	T_C	FTIR 588/619	Mn in Ni site (%)	Ordered domain size (% of crystallite size)
FC	0.18	0.16	97	0.88	--	--
SC	0.12	0.12	112	0.91	--	--
A48	--	0.06	125	1.02	14%	44(11)%
A240	--	0.03	127	1.06	8%	69(10)%

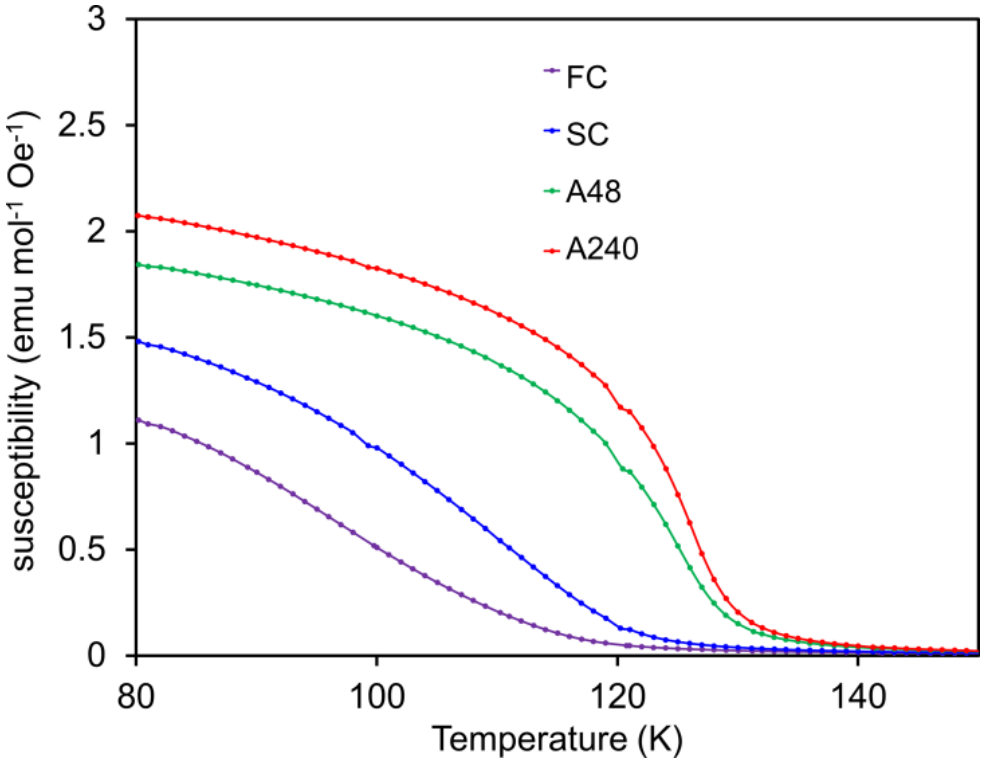

Figure 5.3. Magnetic susceptibility of $LiMn_{1.5}Ni_{0.5}O_4$ spinels, showing the magnetic transition temperatures.

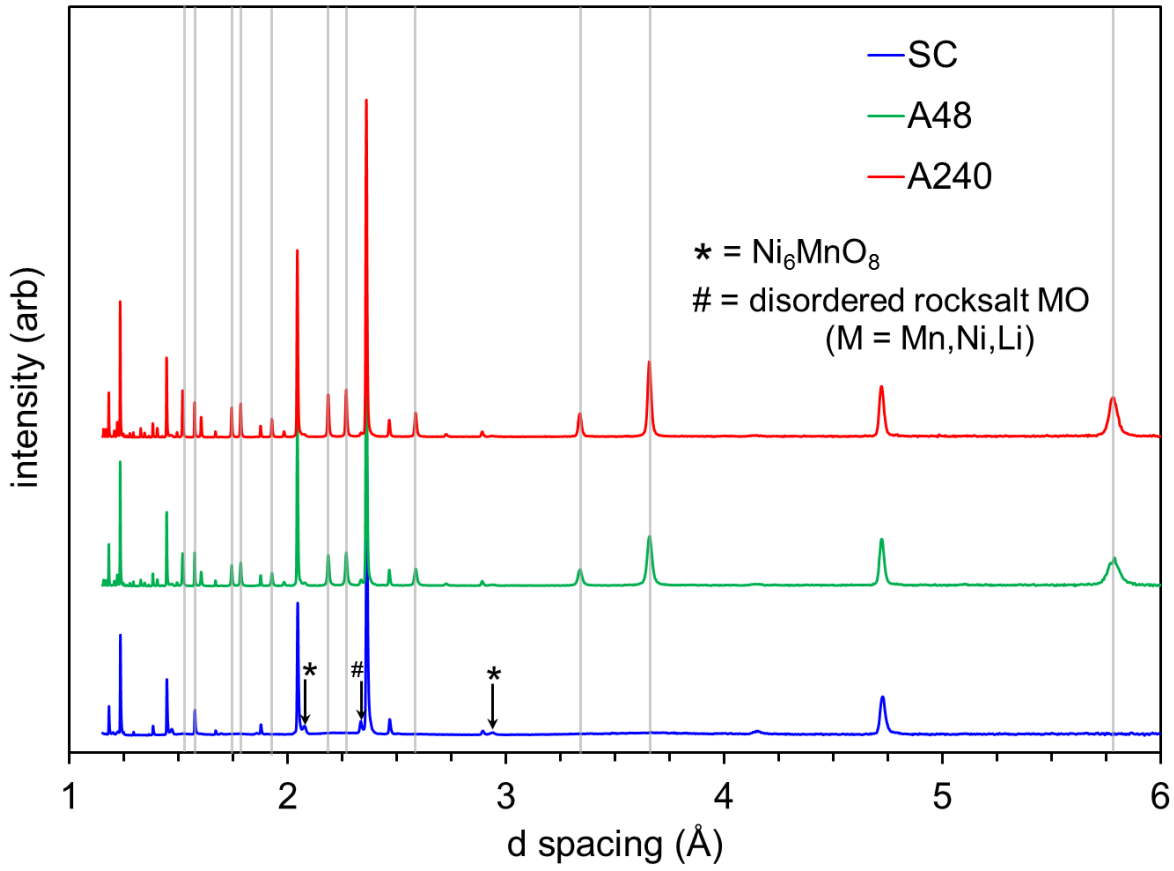

Figure 5.4 Neutron diffraction patterns of SC, A48, and A240. Vertical gray lines denote characteristic peaks of the $P4_332$ symmetry. Rock-salt impurities are indicated by asterisk and hashtag in the disordered SC specimen.

5.3.3 Phase Transformation Behavior

Among lithium-ion intercalation materials, two possibilities exist for phase transformations during lithium insertion/extraction: solid-solution behavior and two-phase behavior, which are dictated by which phases are thermodynamically stable at a given lithium content. The olivine cathode material $LiFePO_4$ showcases marked two-phase reaction behavior, with fully lithiated $LiFePO_4$ and $FePO_4$ being the only stable compositions at room temperature.[108–110] Ordered $LiMn_{1.5}Ni_{0.5}O_4$ develops similar behavior, with stable compositions of $LiMn_{1.5}Ni_{0.5}O_4$, $Li_{0.5}Mn_{1.5}Ni_{0.5}O_4$, and λ-

$Mn_{1.5}Ni_{0.5}O_4$.[97,98,101] Therefore, delithiation proceeds in a two-step two-phase process. It has been shown through simulations that disordered spinel has a higher likelihood to form a solid-solution with various lithium-ion concentrations,[98] and XRD studies have confirmed this.[101]

This critical difference between ordered and disordered $LiMn_{1.5}Ni_{0.5}O_4$ spinel has been theorized to control the rate performance in lithium-ion cells. The rate of the two-phase transformation is limited by the boundary migration between the two phases, which itself is limited by the concentration gradient of lithium ions or vacancies allowed in the two phases. A material which possesses solid-solution behavior with respect to lithium ions can sustain much higher lithium concentration gradients throughout the entire primary particle, and thus by Fick's law will allow for faster lithium diffusion and higher rate capability.

XRD was carried out on all delithiated specimens in order to observe the thermodynamically stable compositions at various lithium contents. Rietveld or LeBail fits to the observed data are detailed in Figures B4-B7 and Table B2 of the supporting information. The reduced data are shown in Figure 5.5. Both the FC and SC samples display solid-solution behavior from $LiMn_{1.5}Ni_{0.5}O_4$ to $Li_{0.5}Mn_{1.5}Ni_{0.5}O_4$, and two-phase behavior with further lithium extraction. Both of the annealed samples, A48 and A240, follow the two-phase behavior characteristic of more ordered high-voltage spinel throughout the full range of lithium contents. It should be noted that these diffraction patterns reveal the thermodynamically stable phases and that it may entirely possible that a high degree of solid-solubility exists under high rate conditions. This idea will be further explored with the discussion of the electrochemical data.

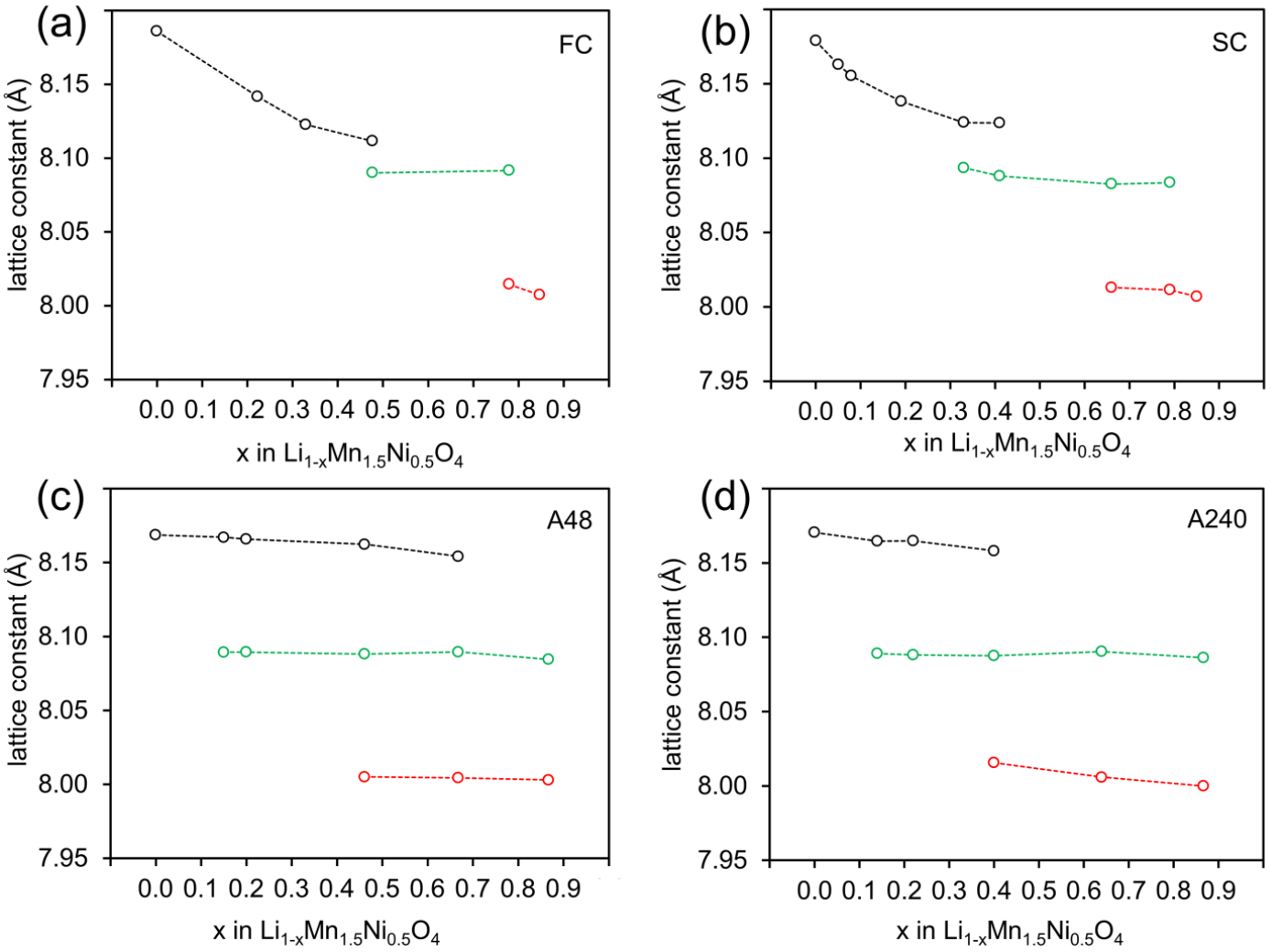

Figure 5.5 Lattice parameters determined from X-ray diffraction patterns of (a) FC, (b) SC, (c) A48, and (d) A240.

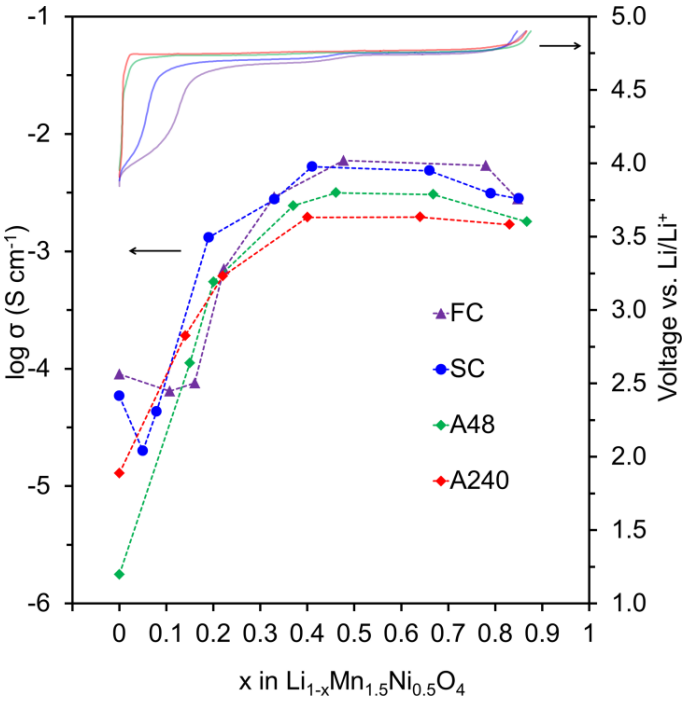

Figure 5.6 Electronic conductivity at 25°C and electrochemical charge profiles for FC, SC, A48, and A240 $LiMn_{1.5}Ni_{0.5}O_4$ spinels.

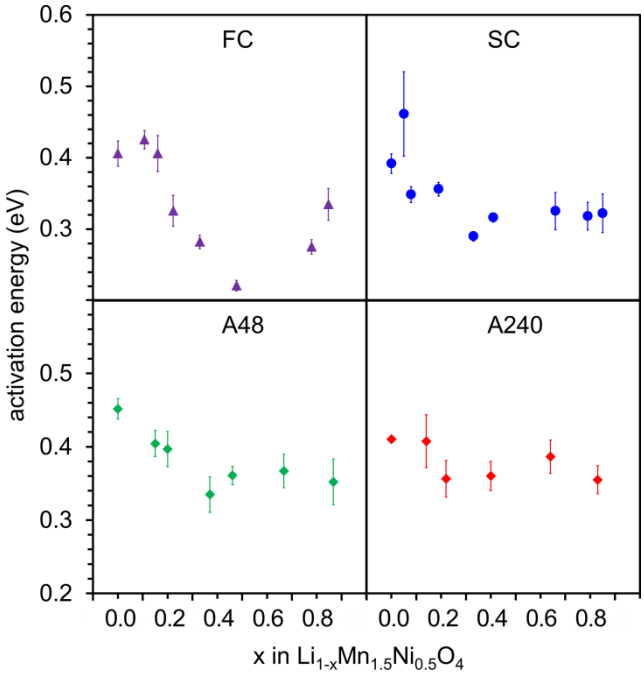

Figure 5.7 Measured activation energies for FC, SC, A48, and A240 $LiMn_{1.5}Ni_{0.5}O_4$ spinels from Arrhenius relation.

5.3.4 Impedance Measurements

The results of the AC impedance measurements at room temperature are depicted in Figures 5.6 and 5.7.The first and most important detail to note is that the conductivity increases by several orders of magnitude when lithium is extracted and the Fermi level crosses the gap between the $Mn^{3+/4+}$ sates to the $Ni^{2+/3+}$ states, or when Ni becomes the redox-active ion. The most likely explanation for this increase in conductivity is that the covalent mixing between Ni:e_g states and O:2p states is stronger than that between Mn:e_g and O:2p, and so oxygen-mediated charge transfer is easier. This behavior has been hinted at before,[102] but a complete picture for samples with varying degrees of cation ordering has not been fully explored. Ransil was only able to extract about ~0.2 Li per formula unit in the disordered material and ~0.5 from the ordered material, and further lithium extraction resulted in cracked pellets.[102]

It is also notable that the measured conductivity reaches a maximum for all samples near x = 0.5 in $Li_{1-x}Mn_{1.5}Ni_{0.5}O_4$, where most of the Ni is present as Ni^{3+} - not as mixed valent $Ni^{2+/3+}$ or $Ni^{3+/4+}$. This implies that the $Ni^{2+/3+}$ and $Ni^{3+/4+}$ couples can be thought of as one continuous, overlapping series of states, and the maximum carrier density is reached when these states are half occupied, or when Ni^{3+} is the average oxidation state. The supposition that mixed valence states are responsible for electronic conduction in oxides does not hold here, similar to that in the perovskite, $LaNiO_3$, which has metal-like conductivity and single-valent Ni^{3+}.[111] From a crystal field theory point of view, the low-spin Ni^{3+} ion possesses one electron in the doubly degenerate lower e_g energy level (separated from the upper e_g level by and intra-atomic exchange energy, Δ_{ex}) resulting in a half-filled state. Charge transfer can occur by hopping between these half-filled e_g orbitals.

Unlike $LaNiO_3$, $Li_{0.5}Mn_{1.5}Ni_{0.5}O_4$ does not display metal-like conductivity or coherent electron transfer. In the perovskite, overlapping and strongly covalent 180° Ni-O-Ni bonds allow for coherent oxygen mediated electron transfer between the e_g orbitals of Ni ions. In the spinel structure, these 180° bonds are absent due to the vacant 16d sites. Direct metal-metal orbital overlaps do exist in spinel, but these overlaps are between t_{2g} orbitals with energies that lie well below the Fermi level and the top of the O:2p band, so they cannot take part in charge transfer. Charge transport is expected to take place in the form of incoherent motion via adiabatic small-polaron hopping between e_g orbitals of the Ni ions; this mechanism is characteristic of many oxides, and has been evidenced in $LiMn_2O_4$.[86,112–115]

A small polaron manifests in an ionic solid as a point charge accompanied by a local distortion of the ions around that charge.[116,117] This distortion creates a self-trapping effect in which the charge carrier is at the bottom of a potential well created by its presence through electron-phonon coupling. This charge carrier hops to neighboring ions when the lattice is favorably distorted. In $LiMn_2O_4$, this is how electrons hop from one Mn^{3+} ion to a Mn^{4+} ion.[112–115,118] Polaron transport becomes more complex in $LiMn_{1.5}Ni_{0.5}O_4$ since there are two kinds of electroactive transition metal ions (Mn and Ni) and charge carriers can be either p- or n-type depending on the oxidation state of the metal ions. The situation is complicated further by the fact that the polarons are centered on Ni ions for the majority of charge/discharge and the Ni are isolated from one another in a matrix of non-conductive Mn^{4+} ions.

It can be seen in Figure 5.6 that as the annealing time and the degree of Mn/Ni ordering increases, the conductivity in the Ni-active region decreases. Correspondingly, Figure 5.7 shows that the minimum measured activation energy also increases on going from FC (0.21(1) eV) to A240 (0.36(3) eV). The corresponding Arrhenius plots can be

found in Figure B8 of Appendix B. This behavior may be explained by the obstacles to polaron hops, which arise from the isolation of Ni ions in the $P4_332$ space group. In this unit cell, every Ni ion has zero Ni and six Mn nearest neighbors, disallowing direct Ni-Ni interactions and inhibiting charge transfer. Transfer of charge to a neighboring Mn ion would have a very high activation energy owing to the ~ 0.7 eV separation between Mn:$3d^4$ and Ni:$3d^8$ states (estimated from the difference in electrochemical plateau voltages).

The change in measured conductivity between the most disordered spinel (FC) and the most ordered spinel (A240) is relatively small compared to the change in conductivity where the Fermi level crosses the gap from $Mn^{3+/4+}$ to $Ni^{2+/3+}$ couple. This small change in conductivity likely has a negligible impact on rate capability in lithium-ion cells.

5.3.5 Seebeck Coefficients

A negative Seebeck coefficient implies that the charge carriers in a material consist mostly of electrons, whereas positive coefficients are characteristic of holes. Since all $LiMn_{1.5}Ni_{0.5}O_4$ specimens in this study possess small amounts of Mn^{3+} initially, the Fermi level is near the bottom of the band corresponding to the $Mn^{3+/4+}$ couple and the Seebeck coefficient appears highly negative, as shown in Figure 5.8. This charge transport is similar to the n-type polaron charge transfer that occurs in $LiMn_2O_4$.[114,115] Measured Seebeck and conductivity values can be matched to the Fermi level at different lithium contents and transition-metal oxidation states. A schematic is depicted in Figure 5.9 using the SC spinel as an example. The density of states cartoon is a visual aid and should not be taken literally; from the arguments presented in the previous section,

$LiMn_{1.5}Ni_{0.5}O_4$ is a polaronic, not a metallic, conductor if the Fermi energy is in the middle of a Mn or Mn redox couple.

The Seebeck data of the as-prepared spinels show an n-type conductivity, which shows the samples are somewhat Mn-rich with a Fermi energy located at the bottom of the $Mn^{3+/4+}$ couple of $Li[Mn_{1.5+x}Ni_{0.5-x}]O_4$ at position #1 of the schematic energy density of electronic states exhibited in Figure 5.9. Upon removal of lithium, the Fermi energy is lowered; initially it falls into the energy gap (position #2) between the $Mn^{3+/4+}$ and $Ni^{2+/3+}$ couples. The scarcity of states in the gap reduces the number of charge carriers and the conductivity drops significantly. On entering the $Ni^{2+/3+}$ / $Ni^{3+/4+}$ band of energies (position #3), the charge carriers become p-type; a Ni^{3+} ion can transfer a hole to a neighboring Ni^{2+} ion. As more lithium is removed, the Fermi energy approaches the middle of the $Ni^{2+/3+}$ / $Ni^{3+/4+}$ band. However, as indicated in Figure 5.9, the crossover to n-type conductivity occurs at $x \approx 0.4$, rather than $x = 0.5$, of Li_{1-x} (position #4). Exact location of this crossover point is dependent on the (unknown) shape of the density of states. As more lithium is extracted, the Fermi energy approaches the bottom of this band and carriers become n-type again as Ni^{3+} ions transfer electrons to Ni^{4+}.

The measured Seebeck coefficients show very little change with temperature in the interval from 320 to 250 K; the low Seebeck characteristic energy is much smaller than the measured hopping activation energy from AC impedance measurements. Therefore, the measured activation energy is almost entirely a result of the thermally-assisted hopping[117] of polarons between Ni ions.

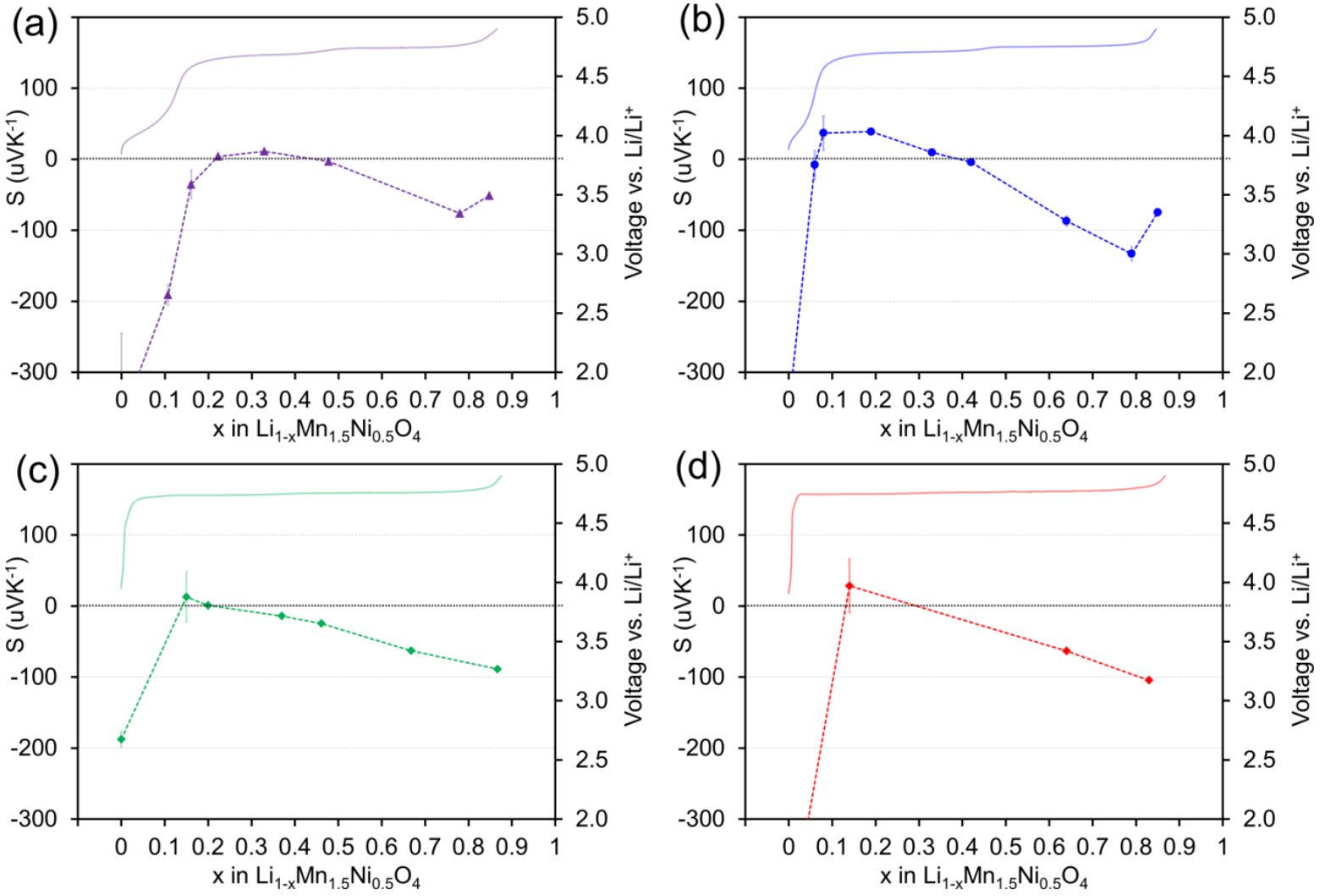

Figure 5.8 Seebeck coefficients vs. Li content for (a) FC, (b) SC, (c) A48, and (d) A240.

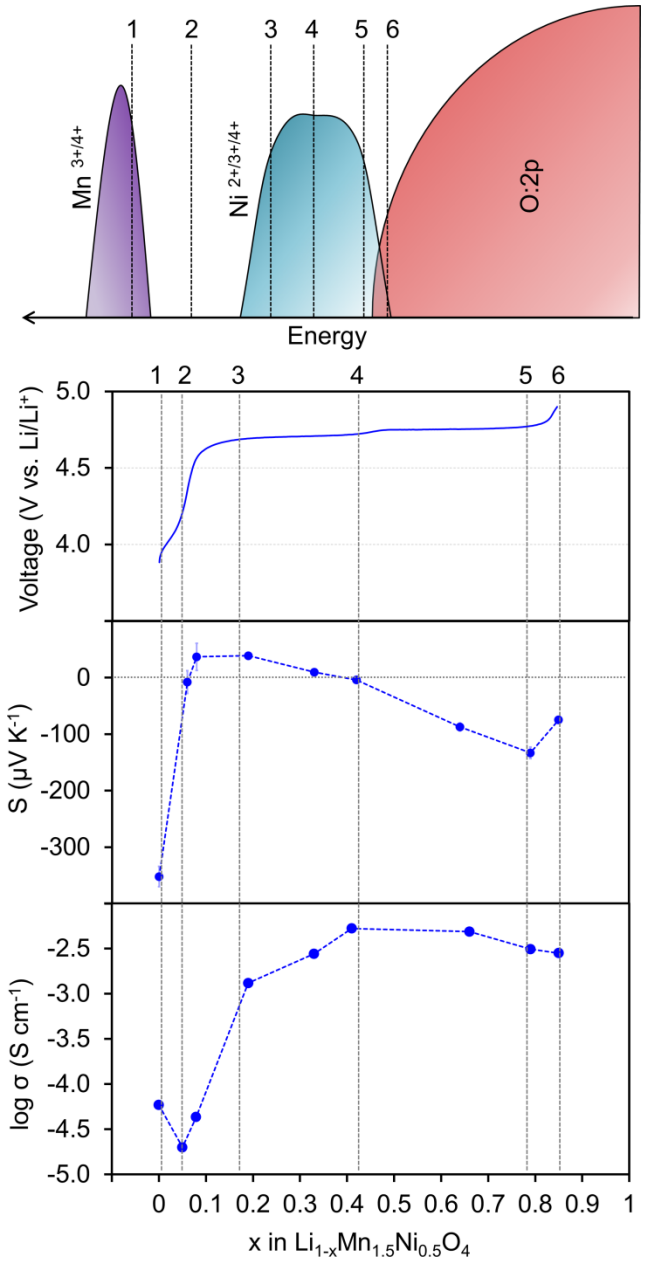

Figure 5.9 Fermi energy and density of states, cell voltage, Seebeck coefficient, and electronic conductivity plotted as a function of lithium content for SC.

5.3.6 Electrochemical Performance

The primary metric of electrochemical performance evaluated in this study is power (rate) capability. The rate capability of high-voltage spinel is one of its most impressive attributes and has been studied in depth.[37,38,40,87,89,119,120] However, to date there has not been a study comparing the rate capability of samples with differing degrees of cation ordering to the bulk electronic conductivity as a function of lithium content. Preliminary work by Amatucci et al.[40] showed that the measured electronic conductivity of a very ordered spinel in the fully lithiated state is several orders of magnitude lower than that of the disordered spinel. This difference is due to the increased Mn^{3+} content present in the disordered spinel as a byproduct of nickel-rich rock-salt formation. That study has been referenced many times to explain the poor rate performance of ordered $LiMn_{1.5}Ni_{0.5}O_4$ spinel. The Mn^{3+} content has long been cited as a necessary ingredient to achieve high rate capability.[63,81,121] However, it is worthwhile to think about what happens to the conductivity when Ni becomes the redox active ion, where all Mn exists in the 4+ oxidation state; i.e. how the rate capability changes as a function of the state-of-charge (SOC).

It has been shown that samples subjected to 700 ^oC heat treatments (which increases the fraction of $P4_332$ phase as confirmed by neutron diffraction data) can possess excellent rate performance even though the Mn oxidation state is higher than that of a disordered spinel and there are fewer Mn^{3+} charge carriers.[39,100] From those studies, one can conclude that Mn^{3+} content is not a critical component of high power density. The data shown in this study supports the notion that initial Mn^{3+} content does not play a significant role, since Mn^{3+} carriers are only generated near the end of discharge.

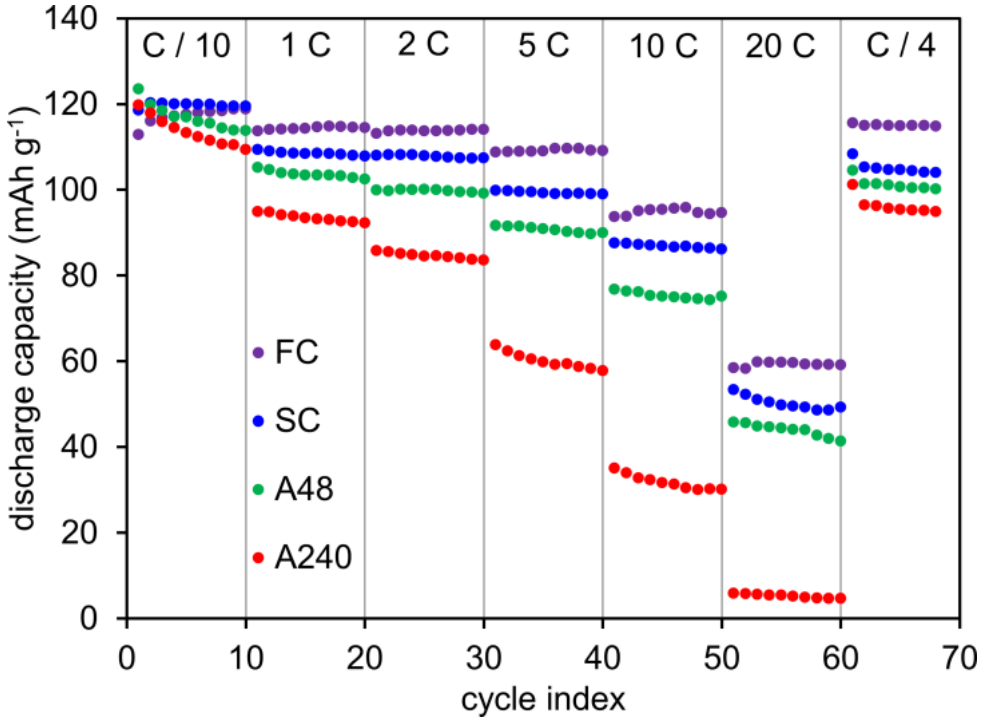

Figure 5.10 Discharge capacity of FC, SC, A48, and A240 at high C-rates. The cutoff voltage is 3.5 V vs. Li/Li^+.

The discharge capacities of the four samples, FC, SC, A48, and A240, at constant C-rates are shown in Figure 5.10. As expected, the more disordered samples perform better than the two ordered samples. However, terminating the rate capability tests at 3.5 V makes it difficult to determine the rate performance at high lithium contents since concentration polarization effects are exacerbated with extended discharges. Therefore, pulse-power rate capability tests with no voltage cutoff were performed to more thoroughly examine the rate capability as a function of SOC. The results of these tests are displayed in Figure 5.11. The pulse-power test consists of 10C discharge pulses every 30 min of C/10 cycling. The cell is allowed to rest for 30 min before and after each pulse.

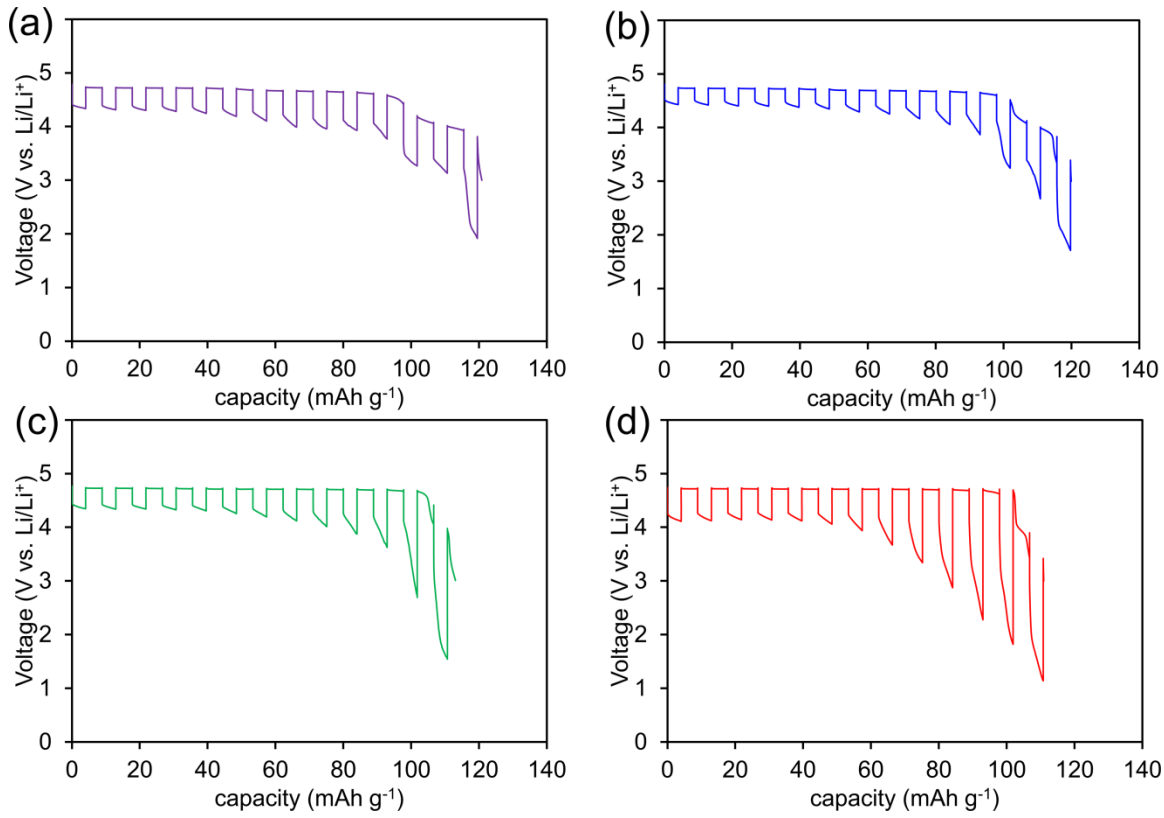

Figure 5.11 Pulse-power capability of (a) FC, (b) SC, (c) A48, (d) A240. 10C pulses are initiated after 30 minutes of C/10 discharge and a 30 minute rest period.

For SOC > 80%, the discharge overpotential is approximately 300 mV for the SC spinel and 400 mV in the case of the FC and A48 spinels. Near the end of discharge, or about 15% SOC, the overpotential increases as the highly-insulating, fully-lithiated $LiMn_{1.5}Ni_{0.5}O_4$ becomes the major phase. From this pulse-power data, one can see that there is very little difference in performance among the FC, SC, and A48 samples. Among the four samples, only A240 stands out as a poor performer, and only below 50% SOC. Above 50% SOC, the overpotential is approximately 500 mV, but this value steadily grows to a value over 2 V as the SOC is decreased. This behavior can be explained by the conductivity data presented earlier: the electronic (and presumably ionic) conductivities are at a maximum in the sample with x = 0.5 ($Li_{0.5}Mn_{1.5}Ni_{0.5}O_4$),

where the tetrahedral sites are half-filled (maximum ionic charge carrier concentration) and the Ni exists almost entirely as Ni^{3+} (maximum electronic charge carrier concentration).

The conductivity of the delithiated phase ($Li_{0.17}Mn_{1.5}Ni_{0.5}O_4$) is also quite good, and is only slightly lower than the maximum measured value. Therefore, for the first half of discharge (SOC > 50%) the only phases present in the cathode are highly conductive and the internal resistance is relatively low even though a two-phase reaction is taking place. This higher rate is because charge carrier concentration and carrier mobility is very high in both $Mn_{1.5}Ni_{0.5}O_4$ and $Li_{0.5}Mn_{1.5}Ni_{0.5}O_4$ phases, compared to $LiMn_{1.5}Ni_{0.5}O_4$. Below 50% SOC, the highly insulating $LiMn_{1.5}Ni_{0.5}O_4$ phase precipitates and grows from conductive $Li_{0.5}Mn_{1.5}Ni_{0.5}O_4$. As the fraction of this phase increases in the cathode, ionic and electronic carriers are diminished and internal resistance rises quickly, producing large overpotentials and limiting the power output of the cell. This problem is avoided in the disordered spinels where a lithium solid solution exists below 50% SOC - this solid solution behavior allows for faster kinetics as carrier concentration gradients across the bulk of the crystallite encourage diffusion.

It is interesting to note that the A48 is more similar to the unannealed spinels in terms of performance than A240. Both annealed samples possess inferior conductivities in the fully lithiated state (because of the low Mn^{3+} content) and XRD confirms that there are three thermodynamically stable phases formed during charge/discharge with clearly defined lithium contents and limited solid-solubility. Nevertheless, the A48 spinel manages to perform almost as well as the slow-cooled and fast-cooled spinels. Based on these observations, we are forced to conclude that: (i) the electronic conductivity of the as-prepared fully-lithiated spinel does not explicitly govern rate capability and (ii) the existence of thermodynamically stable line phases is not necessarily indicative of poor

rate performance. Indeed, other studies on $LiMn_{1.5}Ni_{0.5}O_4$ have shown that this compound is capable of impressive power output without exhibiting equilibrium solid-solubility.[39] Thus the two most popularly cited reasons as to why "ordered" high-voltage spinel is inferior to "disordered" spinel are not as straightforward as they may seem.

A plausible mechanism which can explain the overall behavior observed in the current study is similar to the one which exists in the $LiFePO_4$ / $FePO_4$ system (metastable solid solutions). With *in-situ* synchrotron XRD, it was shown that $LiFePO_4$ can form non-equilibrium solid solutions at high rates, which quickly relax into the characteristic $LiFePO_4$ and $FePO_4$ phases when the load is removed.[109] It is possible that $LiMn_{1.5}Ni_{0.5}O_4$ also exhibits this phenomenon. It has been shown that the degree of cation ordering influences the ease at which solid-solutions can be formed.[98] If this influence extends to the formation of non-equilibrium solid-solutions, this could explain the observed difference in performance of A48 and A240, *i.e.*, A48 may more easily form a kinetic solid-solution. Accordingly, poor rate performance in $LiMn_{1.5}Ni_{0.5}O_4$ spinel cathodes is likely caused by the simultaneous occurrence of the following: (i) the presence of a highly insulating phase with a low tolerance for ionic vacancies and (ii) the inability of the cathode material to form non-equilibrium solid-solutions at high C-rates. Further investigation with *in-situ* XRD may help in this regard.

5.4 CONCLUSION

The electronic properties of the high-voltage spinel $LiMn_{1.5}Ni_{0.5}O_4$ as a function of heat treatment and lithium content were studied and compared to the rate performance in lithium-ion half-cells. Conductivity and activation energy measurements confirm that charge transfer occurs by polaron hopping. Seebeck data revealed that the $Ni^{2+/3+}$ and $Ni^{3+/4+}$ redox couples are part of a single 3d band, and that the electronic charge carrier

concentration is a maximum when the Fermi level is located in the middle of this band. Accordingly, a maximum electronic conductivity was found near a lithium content of 0.5 per formula unit for all samples, corresponding to an average Ni oxidation state of 3+. The minimum electronic conductivity, about three orders of magnitude lower than the maximum, was measured when the Fermi level crossed the gap from the $Mn^{3+/4+}$ to the $Ni^{2+/3+}$ couple. For ordered spinels, this value was measured in the fully lithiated state, $LiMn_{1.5}Ni_{0.5}O_4$. For disordered spinels and spinels with Mn/Ni ratio > 3, this value was measured at a lithium content corresponding to the initial Mn^{3+} in the lithiated material.

XRD was performed on chemically delithiated powders to study the stable phases formed during cycling. For unannealed spinels, a solid-solution region was detected above lithium contents of 0.5 per formula unit, after which a two-phase region was detected. The annealed spinels were characterized by two separate two-phase regions throughout, consistent with previous reports.

The conductivity and phase transformation mechanisms for each of the four samples, FC, SC, A48 and A240, were compared with electrochemical data. Among these samples, only the spinel subjected to a 240-hour anneal showed inferior rate performance; the A48 spinel, although more similar to A240 in terms of electronic properties and phase transformation behavior, displayed rate performance more like the two unannealed specimens. Based on the small difference in electronic conductivity and carrier activation energy between the two samples, we conclude that the poor rate capability of A240 is not related to the intrinsic electronic properties. These results challenge the commonly held beliefs about high-voltage spinel: (i) low Mn^{3+} content is responsible for poor rate performance and (ii) thermodynamically stable solid-solubility is critical for fast kinetics.

Chapter 6: In-situ Mitigation of First-cycle Anode Irreversibility in a New Spinel / FeSb Lithium-ion Cell Enabled via a Microwave-assisted Chemical Lithiation Process

6.1 INTRODUCTION

Lithium-ion batteries have revolutionized the mobile electronics industry and are now starting to have a noticeable impact on the personal transportation sector with the introduction of next-generation electric vehicles.[4,64,122] Most lithium-ion cells utilize the same graphitic-carbon anode which was first employed by Sony in 1990.[123] Graphite offers a gravimetric capacity of 372 mAh g^{-1} and a low potential vs. the Li/Li^+ couple, maximizing the energy density of Li-ion full cells. On the other hand, sluggish insertion kinetics upon fast[124–126] is a significant drawback to the implementation of graphitic carbon anodes in large-scale applications, which demand high power charging such as hybrid and electric vehicles. For these reasons, significant research over the last decade has been dedicated to the search for alternative anode materials with a higher average voltage vs. Li/Li^+ to enhance the safety characteristics of the cell. Notable examples include metal-oxide conversion materials,[127] nano-TiO_2,[128,129] $Li_4Ti_5O_{12}$,[35,36,130] and Sn,[129,131,132] Sb,[133,134] and Si[17–19] alloy electrodes. In addition to the higher potential vs. Li/Li^+, many of these anode materials offer improved gravimetric and volumetric energy density compared to LiC_6.

In terms of stable high-power cycling capability, the spinel $Li_4Ti_5O_{12}$ stands out as a prominent next-generation anode.[36] However, the very high operating voltage vs. Li/Li^+ (1.5 V) and limited gravimetric capacity (170 mAh g^{-1}) reduce the overall energy

---

Z. Moorhead-Rosenberg, K.L. Harrison, T. Turner, & A. Manthiram. A rapid microwave-assisted solvothermal approach to lower-valent transition metal oxides. *Inorganic Chemistry* 52(22) 13087-93 (2013). K.L. Harrison and T. Turner provided some material used in this study. A. Manthiram supervised the project.

density of full cells well below what is competitive with conventional graphite-based anodes.

Recently, composite alloy anodes have emerged as alternative high-rate, high voltage anode materials due to average voltages around ~0.5 V vs. Li/Li^+. Proper integration of the nano-alloy particles in a structural reinforcing matrix such as Al_2O_3 or TiC prevents nanoparticle agglomeration and pulverization.[133–136] These composite anodes, containing active materials such as Sn, FeSb, and Cu_2Sb, offer several advantages to $Li_4Ti_5O_{12}$ including lower voltage and higher capacity (between 200 and 400 mAh g^{-1}), which results in a marked improvement in energy density if employed in a Li-ion full cell.

Implementation of next-generation anode materials including TiO_2, metal-oxides, and metal-alloys is largely inhibited by irreversible capacity loss stemming from first-cycle solid-electrolyte interphase (SEI) layer formation and other side reactions.[137] This irreversible capacity can reach as high as 40-50% of the total gravimetric capacity depending on the anode material and prevents full utilization of the cathode active mass since a large fraction of the lithium ions in the as-prepared cathode are consumed in the irreversible reactions. The result is that the as-assembled full cell without anode pre-treatment has a much reduced energy density. To combat this phenomenon in laboratory-scale testing, several complicated multi-step process can be employed to prime the anodes before they are placed in full cells. Often this process involves mixing the anode with stabilized lithium metal powder (SLMP),[138] Li-metal strips,[17] or cycling the anodes in a half-cell with a lithium counter electrode before being removed and then placed in a full cell.[139] Because any process involving metallic lithium necessitates the use of an inert atmosphere, this process is not conducive to large-scale, economic production and is a major hurdle for commercialization.

The high-voltage spinel cathode, $LiMn_{1.5}Ni_{0.5}O_4$ has received much attention in the past decade due to its promise of high energy density, non-reliance on cobalt, high voltage, and excellent rate capability.[140] Also, the spinel structure offers a unique ability that conventional layered-oxide cathodes lack: the ability to store extra lithium in unoccupied crystallographic sites. If these unoccupied sites could be filled with lithium, and if that excess lithium could be used to account for the SEI layer formation on the anode surface, the remaining lithium would be able to cycle reversibly between the cathode and the anode, resulting in the utilization of the full capacity of both cell components.

The excess lithium stored in the cathode can be termed as the "lithium reservoir." The concept is not new; it was postulated in the early 90's by Tarascon as a way to cope with the irreversibility of graphite anodes using spinel as a cathode.[24] The idea was to over-lithiate the cathode by a chemical process so that the extra lithium is consumed by the graphite SEI formation and the full cathode gravimetric capacity can be utilized. This was achieved by treating the as-prepared $LiMn_2O_4$ spinel with lithium iodide, which was not only time consuming but the cost of LiI made the process prohibitively expensive. Therefore, a more economical process must be developed to attain feasibility. For instance, n-butyllithium[141] is commonly used for laboratory chemical lithiation processes but it is not sustainable for large scale application. Other chemical lithiation processes have been suggested such as Li-alkoxide formation in alcohol by dissolving lithium hydroxide[142] or lithium metal,[143] respectively, in ethanol or pentanol. The first process is rather slow and spinel materials quickly lose their lithium in ethanol over the long reaction period; the use of ethanol limits the reaction temperature to ~ 80 ^oC, so the kinetics is slow.[143] The second process, while more kinetically favorable, still relies on

the use of volatile metallic lithium chips or powder, complicating the process for industrial scalability.

The technique presented in the present study offers a new way to overcome this hurdle using easily scalable processes without hazardous, expensive, or exotic chemicals or metallic lithium which requires an inert atmosphere. Described is a new microwave-assisted chemical lithiation technique using tetraethylene glycol (TEG) as a reducing agent and LiOH salt as a lithium-ion source, both of which are relatively inexpensive compared to the chemicals used in the abovementioned processes. In a related approach, the refluxing of $FePO_4$ with LiOH in TEG has been reported to produce $LiFePO_4$.[60] However, the refluxing temperature of TEG (~ 314 ^oC) is too high for the lithiation of spinel materials used in the current study. Therefore, a microwave heating source was employed to provide precise control over the reaction temperature and conditions. In addition, the process is not moisture sensitive since both the TEG and the hydrated LiOH contain water; a controlled atmosphere is not necessary.

Manganese-based spinels have been heavily researched in the past two decades and offer significant safety and raw materials cost advantages over $LiCoO_2$.[144] $LiMn_2O_4$ type spinels derive their capacity from the extraction/ insertion of Li ions from/into the 8a tetrahedral sites of the crystal, which occurs at ~ 4 V vs. Li/Li^+. This corresponds to a theoretical capacity of 148 mAh g^{-1} for $LiMn_2O_4$ and 146 mAh g^{-1} for $LiMn_{1.5}Ni_{0.5}O_4$. More lithium can be inserted into the empty octahedral sites at ~ 2.7 V, resulting in the tetragonal $Li_2Mn_2O_4$ phase. The same is true of the high-voltage spinel $LiMn_{1.5}Ni_{0.5}O_4$. It was shown that neither $LiMn_2O_4$[145] nor $LiMn_{1.5}Ni_{0.5}O_4$[26] can provide stable cycling when lithium is inserted into these octahedral sites due to the Jahn-Teller distortion caused by Mn^{3+} ions; the phase transition can crack and pulverize the electrode (unless further steps are taken to accommodate the strain caused by the distortion, such as ball-milling[146]).

However, if continued cycling in the 3 V (octahedral site) regime is avoided, both spinel types exhibit very good cyclability. The lithium reservoir approach uses these octahedral sites for only one charge cycle, limiting the degradation of the cathode; only the 8a tetrahedral sites are utilized in subsequent cycles.

To illustrate the concept of pairing an over-lithiated spinel with an alternative anode, the 5 V spinel $LiMn_{1.5}Ni_{0.5}O_4$ and a Ni-stabilized 4 V spinel $Li[Li_{0.05}Ni_{0.05}Mn_{1.9}]O_4$ are combined with the intermetallic alloy FeSb-TiC composite anode to create two advanced lithium-ion cells. The 4 V spinel paired with the FeSb-TiC anode yields a 3.2 V full cell with a specific energy of 190 mWh g^{-1} with respect to the total active material. The 5 V spinel paired with the FeSb-TiC anode discharges at 4 V and has an energy density of 260 mWh g^{-1} (based on total active mass) with excellent rate capability.

The advantages of the 5 V spinel / FeSb-TiC full cell compared to conventional layered-oxide/graphite cells include much higher volumetric energy density[147] owing to the absence of a voluminous graphitic carbon anode, high charge rate capability due to the high voltage and conductive active materials, and reduction of the risk of dendritic lithium formation under fast charge due to the higher intrinsic voltage of the alloy anode.[126] These batteries would be well suited for personal electronic devices which place a premium on volumetric energy density, although the higher voltage of the anode would also make them suitable for hybrid and electric vehicle applications where the capability for fast charge may be desired.

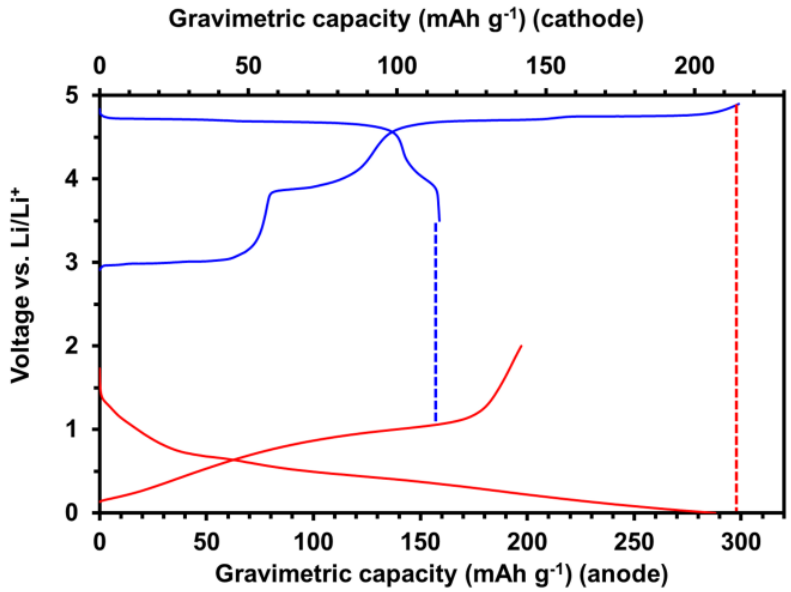

Figure 6.1 Illustration of the lithium reservoir concept with a lithiated 5 V spinel cathode and FeSb-TiC composite intermetallic alloy anode.

The concept of balancing this cell using the lithium reservoir is depicted in Figure 6.1, where the cathode capacity is displayed on the top axis and the anode capacity on the bottom axis. The charge discharge curves in Figure 6.1 are each taken from half-cells with lithium counter electrodes. The excess lithium stored in the 16c sites is extracted at ~ 3-4 V vs. Li/Li^+ and is used up to form the SEI layer on the anode, which has a very large first cycle capacity loss (from ~ 300 mAh g^{-1} on the first charge to ~ 200 mAh g^{-1} after a few cycles).

6.2 EXPERIMENTAL

The high-voltage (5 V) spinel material used in this study was synthesized by a continuously-stirred tank reactor co-precipitation method as described previously.[83] This technique was chosen because it provides the most impressive performance among $LiMn_{1.5}Ni_{0.5}O_4$ spinel synthesized by different methods because of the large particle size and the dominance of the {111} surface planes.[83,148]

The 4 V spinel $Li_{1.05}Ni_{0.05}Mn_{1.9}O_4$ was synthesized by a citrate sol-gel method. Stoichiometric amounts of $C_2H_3LiO_2{\cdot}4H_2O$ (99%, Acros), $Mn(CH_3COO)_2{\cdot}4H_2O$, (99%, Acros), and $Ni(CH_3COO)_2{\cdot}4H_2O$, (99%, Acros) were first mixed in water with citric acid as the chelating agent. The pH of the solution was brought to 7 by adding NH_4OH and the solution was continuously stirred at ~ 90 ^oC on a hot plate until a gel was formed. The magnetic stir bar was removed and the temperature was increased to ~ 300 ^oC to turn the gel into a fine powder. The powder was ground, placed in an alumina crucible, and heated to 850 ^oC for 8 h in a tube furnace.

Undoped lithium manganese spinel, $LiMn_2O_4$, was also prepared via the solid-state route to examine the achievable extend of chemical lithiation. The stoichiometric amounts of Li_2CO_3 and MnO_2 were ground together and then subjected to the same heat treatment procedure as described elsewhere.[146]

The FeSb-TiC anode was synthesized by a two-step process. First, metallic powders of Fe (99.9 %, Alfa Aesar), Sb, (99.5 %, Sigma Aldrich), and Ti (99.5 % Alfa Aesar) were mixed and heated under argon to 600°C for 8 h in a tube furnace. The raw-material powder amounts were calculated to provide a 1 : 1 atomic ratio of Fe : Sb and a final TiC content of 60 wt. %. The resulting powder was combined with a stoichiometric amount of acetylene black carbon to fully convert to TiC and then underwent high-energy

ball-milling at room temperature in an inert argon atmosphere. The free energy change for TiC formation provided the driving force for the mechanochemical reaction.

The microwave-assisted chemical lithiation was carried out in the following manner: 0.5 g of active spinel material, 0.2 g of $LiOH{\cdot}H_2O$ (99%, Acros), and 15 mL of tetraethylene glycol (TEG) were stirred in a borosilicate glass reaction vessel for 5 minutes before being placed in an Anton Paar Monowave 300 microwave synthesis reactor. The mixture was heated to 200 ^{o}C or 190 ^{o}C for the 5 V and 4 V spinels, respectively, and held for a time between 20 and 45 min. The time variable was used to control the amount of Li inserted into the host spinel structure. After the hold time limit was reached, the mixture was cooled and then centrifuged twice with water and three times with acetone to remove any remaining free ions or TEG. The powder was dried in an air oven at 100 ^{o}C resulting in the final excess-lithium spinel product.

Cathode slurries were prepared with 80 wt. % active material, 10 wt. % conductive carbon (Super P), and 10 wt. % binder (polyvinylidene fluoride) in a *N*-methyl-2-pyrrolidone (NMP) solvent. The slurries were stirred overnight to ensure a homogenous distribution of spinel and carbon and then cast onto an aluminum foil current collector with a doctor blade. The electrodes were dried in a vacuum oven at 100 ^{o}C overnight to remove moisture.

Graphite (Conoco Phillips, CPreme G8) anodes were prepared in a similar manner using the same ratio of active material, conductive carbon, and binder. Slurries of the FeSb-TiC anode were prepared in a similar manner, but with 70 wt. % active material (FeSb *and* TiC reinforcing matrix were considered as active mass), 15 wt. % conductive carbon, and 15 wt. % PVDF binder. The slurries were cast onto copper foil current collectors and dried in the same manner.

Electrodes were punched into 1 cm diameter circles and placed into CR2032 coin cells in both the half-cell and full cell configurations. The electrolyte consisted of 1 M $LiPF_6$ in ethylene carbonate (EC) /diethyl carbonate (DEC) (1:1 vol) from BASF. Celgard polypropylene separators were used. Electrochemical testing was carried out on Arbin cyclers at various C-rates. For the full cell tests, the first charge and discharge were carried out at C/6 rate while the remaining cycles were increased to C/4 rates (1C = 146 mA/g by cathode mass). Full cells were balanced primarily by controlling the electrode thickness. The mass loadings of the 5 V and 4 V spinel cathodes were ~ 5.1 mg cm^{-2} when paired with FeSb-TiC anodes and ~ 6.4 mg cm^{-2} when paired with graphite anodes. FeSb-TiC loading was ~ 3.6 mg cm^{-2} and that of the graphite was ~ 2.3 mg cm^{-2}. These loadings were chosen such that the total areal charge capacity of the anodes was similar. An approximately 20% excess anode active material (by capacity) was added to full cells with the FeSb-TiC anode to increase the average voltage of the cell (FeSb-TiC has a sloping voltage). In full cells with graphite, the electrodes were balanced such that the anode capacity matched the cathode capacity, since graphite and high-voltage spinel possess similar first cycle coulombic efficiency (~85%). To ensure identical cathode/anode mass ratios among the multiple cells tested in this study, cathodes were manually trimmed a little, if needed, to reach the intended ratio.

X-ray diffraction (XRD) patterns were collected with a Rigaku Ultima powder diffractometer with Cu-Kα radiation. SEM images were taken with a Quanta FEG 650 scanning electron microscope. The extra lithium inserted during the microwave-assisted chemical lithiation was confirmed by inductively coupled plasma optical emission spectroscopy (ICP-OES) with a Varian 715-ES ICP-OES spectrometer.

6.3 RESULTS AND DISCUSSION

6.3.1 Microwave-assisted chemical lithiation

The microwave-assisted chemical lithiation technique introduced in this chapter is similar to the microwave-assisted solvothermal reduction of transition-metal oxides reported previously.[149] In the previous investigation, it was found that when heated to temperatures around 200-300^{o}C, a TEG solution is capable of reducing metal ions in oxides that have a redox couple energy at or below that of $Mn^{3+/2+}$ (in a six-fold oxygen coordinated environment), which was estimated to be near the highest occupied molecular orbital (HOMO) of TEG. This obviously includes the $Mn^{4+/3+}$ redox couple, which is active during Li insertion into the 16c octahedral sites of the 5 V and 4 V spinels. By adding a lithium source to the mixture, in this case LiOH, when the metal ions are reduced by the TEG the Li^{+} ions in solution are inserted into the host structure to provide charge compensation. When the Li source is not present, charge neutrality is maintained by oxygen loss. This was observed when MnO_2 was subjected to microwave-assisted reduction in TEG, it was reduced to MnO.

The XRD patterns of the as-prepared $LiMn_2O_4$ and $Li_2Mn_2O_4$ obtained after lithiating for 60 min at 190^{o}C are shown in Figure 6.2. It can be seen that the cubic spinel peaks have completely disappeared and are replaced with peaks corresponding to the tetragonal phase with the space group $I4_1/amd$. ICP analysis confirms a Li/Mn ratio of 1.04(2), suggesting complete lithiation of $LiMn_2O_4$ to $Li_2Mn_2O_4$ where all Mn exists as Mn^{3+}.

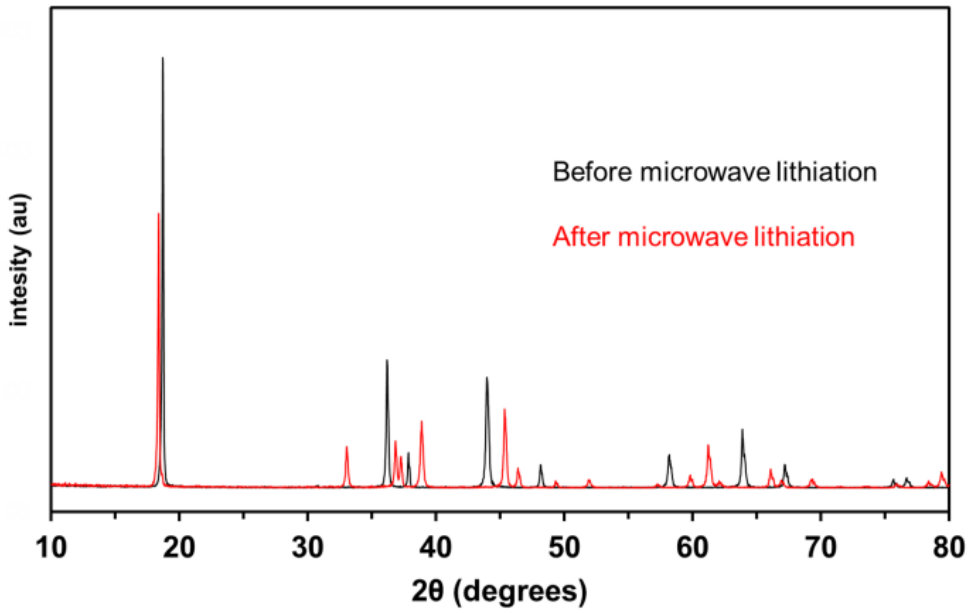

Figure 6.2 XRD of $LiMn_2O_4$ before (black) and after (red) microwave-assisted chemical lithiation for 60 min at 190 ^oC.

In theory, this technique could be used to lithiate any material where lithium insertion occurs above ~ 2.5 V vs. Li/Li^+, since this is approximately the cutoff voltage for the insertion of Li into spinel to create $Li_2Mn_2O_4$. Attempts to lithiate α-$LiVOPO_4$ using this method failed because the insertion potential for extra lithium into it is ~ 2.3 V[150] vs. Li/Li^+ and, therefore, is too low for the TEG to reduce the host structure. For materials which have insertion potentials below 2.5 V vs. Li/Li^+ such as silicon, TiO_2, Li_4Ti_5O12, and other anodes, this technique cannot work and a chemical such as *n*-butyllithium must be used. As long as the energy of the HOMO of the reducing agent is higher than the energy of the redox couple (alternatively, lower than the redox potential vs. Li/Li^+ as in Figure 3), insertion of Li^+ will be energetically favorable. A schematic representation of the TEG HOMO in relation to the insertion potential vs. Li/Li^+ of spinel and other common electrode materials is displayed in Figure 6.3.

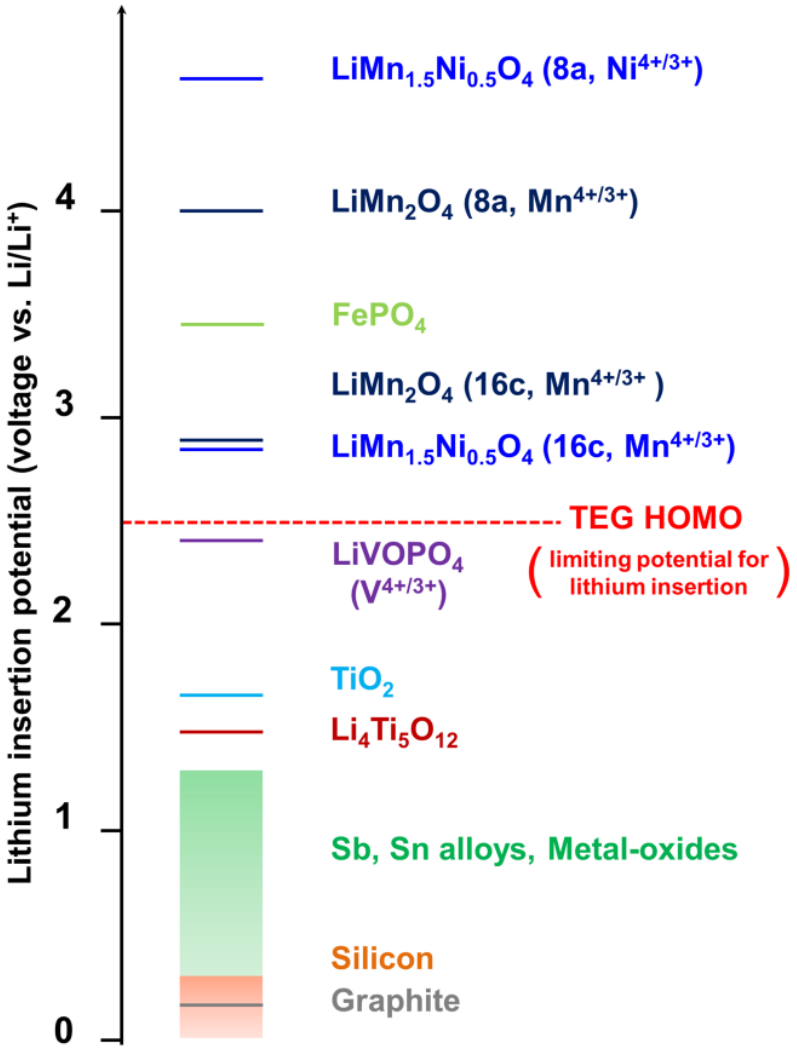

Figure 6.3 Representation of various lithium insertion potentials compared to the highest occupied molecular orbital of TEG with respect to the voltage of the Li/Li^+ couple. Lithium can be inserted into all compounds above the red line with the microwave-assisted chemical lithiation with TEG, but not below.

Table 6.1 Verification of the extent of excess lithium insertion in 4 V and 5 V spinels

spinel	hold time (min)	ICP stoichiometry			1st cycle discharge/ charge ratio	tetragonal spinel % composition
		Li	Mn	Ni		
$Li_{1.05}Ni_{0.05}Mn_{1.9}O_4$	as prepared	1.05 (3)	1.90 (1)	0.05 (1)	0.94	--
	20	1.30 (3)	1.90 (1)	0.05 (1)	0.63	20
	30	1.65 (3)	1.90 (1)	0.05 (1)	0.54	70
	45	1.83 (3)	1.90 (1)	0.05 (1)	0.43	85
$LiMn_{1.5}Ni_{0.5}O_4$	as prepared	1.05 (3)	1.50 (1)	0.49 (1)	0.85	--
	20	1.42 (3)	1.50 (1)	0.49 (1)	0.65	47
	30	1.69 (3)	1.50 (1)	0.50 (1)	0.54	63
	45	1.80 (3)	1.50 (1)	0.49 (1)	0.44	76

Insertion of lithium into the host spinel structure was confirmed by ICP, XRD, and electrochemical testing. The metal contents according to ICP are shown in Table 6.1. It can be seen that with increasing hold time at the specified temperature (200 ^oC for the 5 V spinel and 190 ^oC for the 4 V spinel), more lithium is inserted, up to ~ 2 Li / formula unit at the longest reaction time of 45 min. Examination of the XRD data reveals that Li is indeed inserted into the 16c octahedral sites. It can be seen in Figure 6.4 that as the reaction hold time is increased, the appearance of the tetragonal peaks associated with the tetragonal $Li_2M_2O_4$ (M = Mn, Ni) spinel-type phase becomes more pronounced (Mn^{4+} is reduced to Mn^{3+} and the Jahn-Teller distortion takes place). Rietveld refinement results using GSAS confirm that the tetragonal spinel fraction (Table 6.1) increases with longer hold times. Details of the refinements can be found in Figure C1 in Appendix C. In addition to ICP and XRD, electrochemical tests were used to verify the insertion of extra lithium. Displayed in Table 6.1, the first cycle coulombic efficiency decreased (first

charge capacity increased) as the reaction hold time was increased. The first charge and discharge curves of the as-prepared and pre-lithiated spinels are shown in Figure 6.5. As expected, the samples that were subjected to longer hold times exhibit higher capacity in the first charge cycle because of the extra lithium in the 16c sites. This shows that the microwave-assisted lithiation technique can provide precise control over the amount of lithium added to the spinel. This data is also reflected in Table 6.1. This is important when matching the excess lithium in the cathode with the first-cycle irreversibility of the anode in full cells.

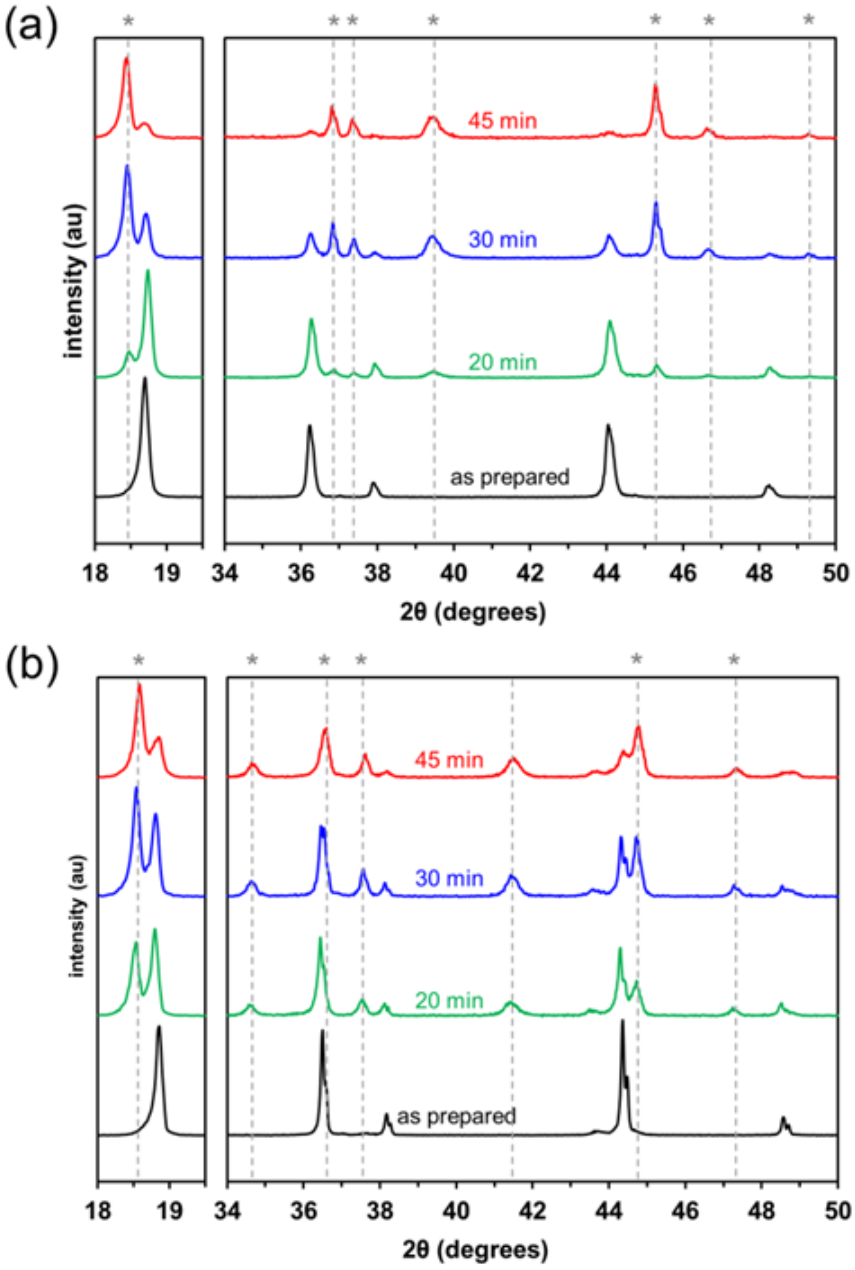

Figure 6.4 XRD patterns of (a) 4 V $Li_{1.05}Ni_{0.05}Mn_{1.9}O_4$ and (b) 5 V $LiMn_{1.5}Ni_{0.5}O_4$ as-prepared and after microwave-assisted lithiation with a given hold time. The reaction temperature was 190 ˚C for 4 V spinel and 200 ˚C for 5 V spinel. Asterisks denote the location of tetragonal $Li_2M_2O_4$ (M= Mn, Ni) diffraction peaks.

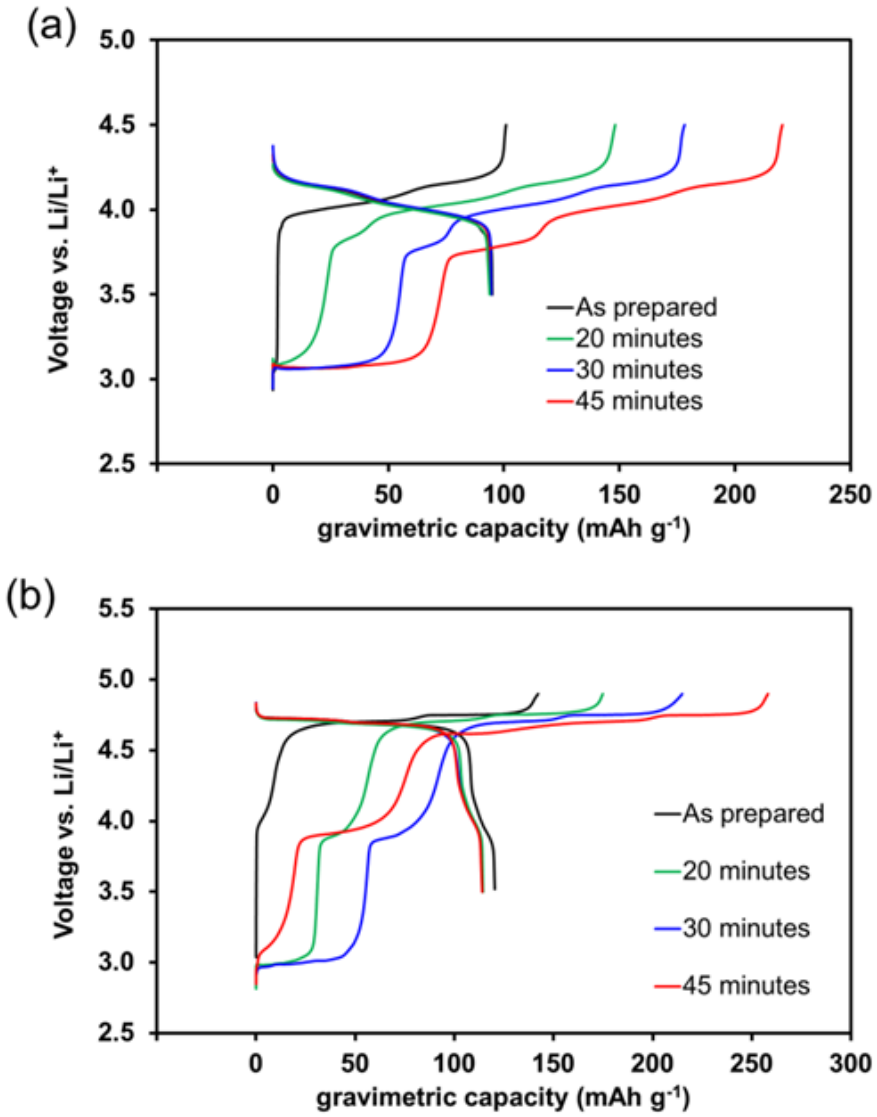

Figure 6.5 First charge/discharge curves of (a) 4 V $Li_{1.05}Ni_{0.05}Mn_{1.9}O_4$ and (b) 5 V $LiMn_{1.5}Ni_{0.5}O_4$ as-prepared and after being subjected to microwave-assisted lithiation.

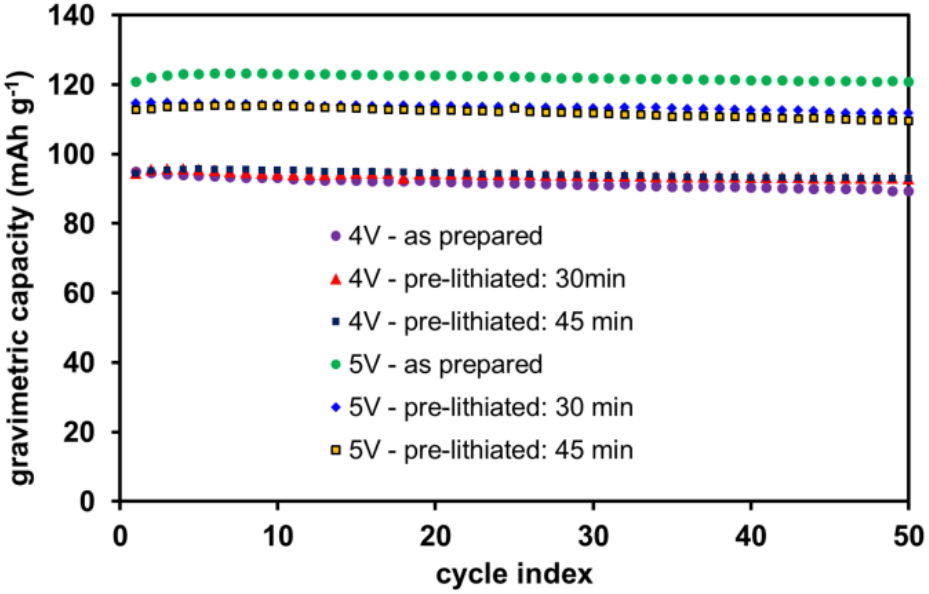

Figure 6.6 Discharge capacity and coulombic efficiency of 4 V and 5 V spinel cathodes in half-cells with Li as the counter electrode.

Cyclability tests were also used to determine whether or not the prelithiation adversely affects the performance of the cathode material. The cooperative Jahn-Teller distortion caused by the presence of Mn^{3+} in the $Li_2M_2O_4$ phase is responsible for severe capacity fade when spinel is cycled below 3 V vs. Li/Li^+.[145] The anticipation was that enduring this distortion only once on the initial charge, and not during repeated cycling, would lead to stable capacity retention comparable to that of the as-prepared spinel materials (without extra lithium). To this end, the as-prepared and prelithiated spinels (30 min and 45 min lithiation) were tested to compare their cycle stability at C/4 rate (1C = 146 mAh g^{-1}). These data are displayed in Figure 6.6. While the capacity of the 5 V $LiMn_{1.5}Ni_{0.5}O_4$ is slightly decreased after the microwave-assisted lithiation process the cycling stability remains on-par with the as-prepared 5 V spinel sample. For the 4 V spinel, there is no marked change in capacity or cycle stability.

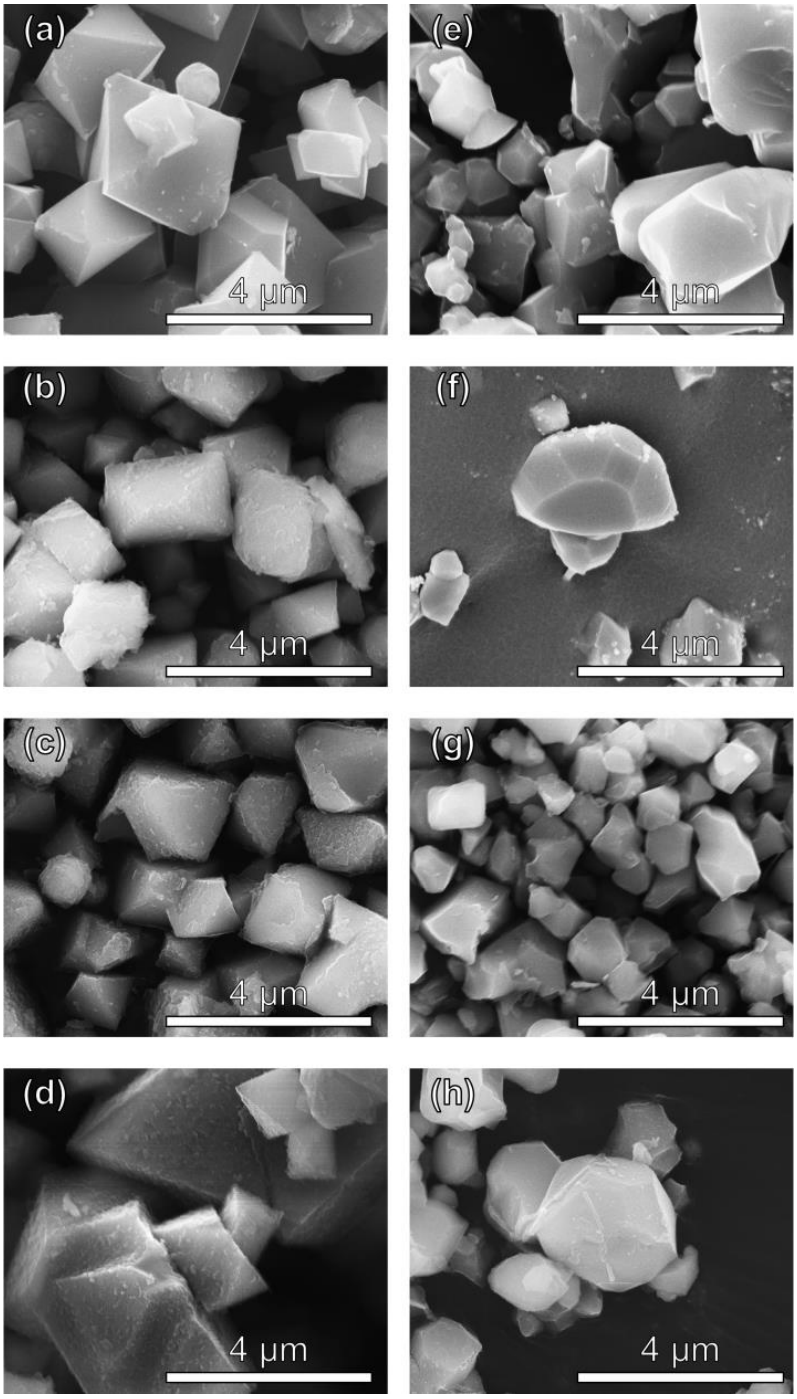

Figure 6.7 SEM images of 5 V spinel: (a) as-prepared and subjected to microwaved-assisted lithiation for (b) 20 min, (c) 30 min, and (d) 45 min. SEM images of 4 V spinel: (e) as-prepared and subjected to microwaved-assisted lithiation for (f) 20 min, (g) 30 min, and (h) 45 min.

Because the lithiation process is mild enough and performed at a low enough temperature, the overall structure and morphology of the as-prepared samples remain unchanged. SEM images taken of the spinel particles before and after the lithiation process are displayed in Figure 6.7. The overall shape and morphology of the powders remain the same all the way up to a hold time of 45 min, as seen in (d) and (h). However, it is interesting to note that the surface of the particles had become rougher on the 5 V samples. High-magnification SEM and EDX suggest that the roughness is not due to a carbonaceous coating left over from the chemical lithiation process but to the precipitation and growth of the tetragonal phase $Li_2Mn_{1.5}Ni_{0.5}O_4$. According to Figure 6.6, this change seems to have no effect on the cyclability of the spinel cathodes although the capacity is decreased by ~ 4%, possibly due to mechanical degradation of some active material incurred during the lithiation process. Contrastingly, the 4 V samples appear to retain their smooth surface - they also show no decrease in capacity or cyclability as a result of the chemical lithiation.

6.3.2 Full Cell Characterization

The overall aim of the microwave-assisted chemical lithiation technique described earlier is to provide an inexpensive, scalable approach to incorporate excess lithium to spinel materials in order to effectively mitigate the first-cycle irreversibility inherent to many next-generation anode materials. Some of these materials have excellent rate capability, and with a Li-insertion voltage well above that of graphite, this makes them ideal candidates for fast-charging. The higher voltage of these anodes allows for the application of a high overpotential without reaching the Li/Li^+ redox couple, and therefore has a lower risk of plating metallic lithium on the anode surface at high C-rates.[126]

One of the more promising anode materials to recently gain attention is the family of intermetallic anodes M_xSb and M_xSn (M = Cu, Fe, Ni). These intermetallics can be imbedded in a structurally supporting matrix such as Al_2O_3[133,134] or TiC[135] to prevent nanoparticle agglomeration and to constrain the large volume expansion of the alloy during lithium incorporation. Previous work on nano-Sn incorporation into a TiC[135] matrix has shown promising performance advantages compared to a non-composite structure. Al_2O_3 is very insulating and limits the rate capability of the anode, but TiC is metallic. When FeSb is embedded in a TiC supporting matrix, the alloy nanoparticles provide very good rate capability and a moderate capacity of 200 mAh g^{-1} at an average voltage of ~ 0.65 V vs. Li/Li^+. The volume expansion upon lithiation of the FeSb alloy is approximately 119% with a theoretical capacity of 453 mAh g^{-1}. This volume expansion is quite large compared to that of graphite (~ 6 -10 %). When embedded in a TiC matrix so that the electrode active mass is 60 wt. % TiC, the theoretical capacity drops to 205 mAh g^{-1} (after accounting for the capacity from TiC). A detailed study of this anode architecture is published elsewhere.[151]

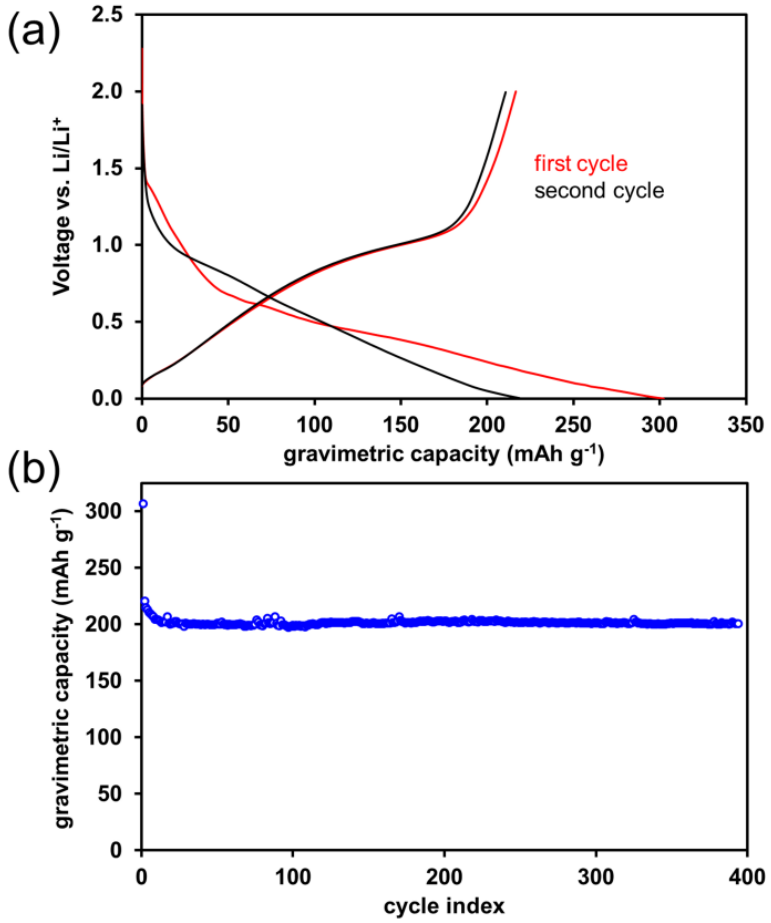

Figure 6.8 (a) First and second charge/discharge curves of FeSb-TiC and (b) long term cycle stability.

The first and second charge/discharge curves and long term cyclability of this composite in a half-cell are displayed in Figure 6.8. This makes it a good candidate for an anode material in a high power cell, perhaps as a substitute for $Li_4Ti_5O_{12}$. While $Li_4Ti_5O_{12}$ has excellent rate capability and stability with many electrolytes, the high voltage of ~ 1.5 V vs. Li/Li^+ and limited practical capacity of ~ 170 mAh g^{-1} limits the energy density of full cell lithium-ion batteries.[35,36] Use of the FeSb-TiC anode, with its higher capacity and lower voltage, would result in an increased energy density. However, FeSb-TiC has a very high first cycle capacity loss (71% 1st cycle coulombic efficiency,

with increasing coulombic efficiency over subsequent cycles) due to complex SEI layer formation, which makes it hard to implement the anode in full cells. The steady capacity is 200 mAh g^{-1}, which is 66% of the initial charge capacity.

The FeSb-TiC anode offers other advantages associated with having a graphite-free electrode - propylene carbonate (PC) can be used as the base electrolyte instead of the standard ethylene carbonate (EC) which is a solid at room temperature and can limit cell performance in mixed-solvent electrolytes at very cold temperatures.[152] The cyclability for FeSb-TiC in a PC-DEC electrolyte can be seen in Figure 6.9. PC cannot be used in lithium-ion batteries with graphite anodes without further modification because of intercalation of the PC molecules into the graphite and the subsequent exfoliation of the active anode material.[153]

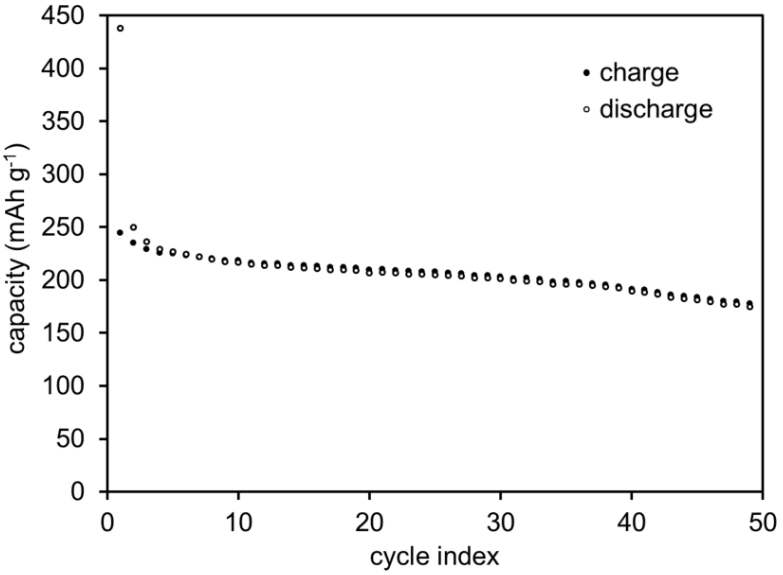

Figure 6.9. Cyclability of FeSb-TiC anode in PC-based electrolyte.

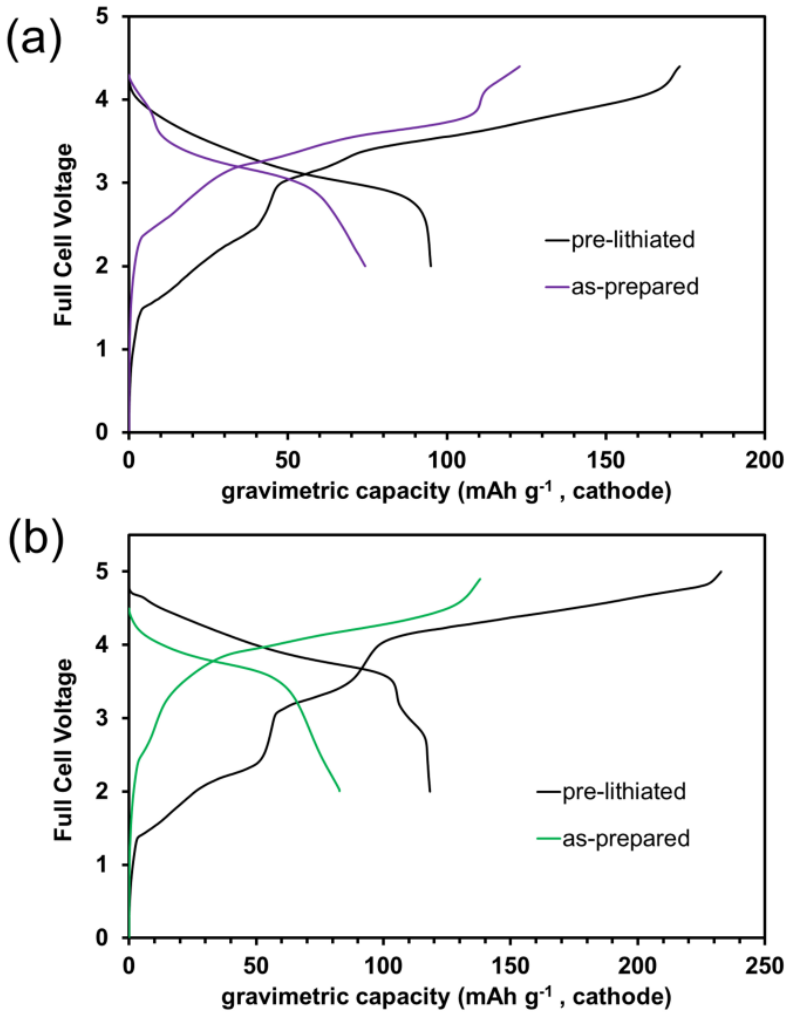

Figure 6.10 First charge/discharge curves of spinel / FeSb-TiC full cells utilizing (a) 4 V spinel cathode and (b) 5 V spinel cathode.

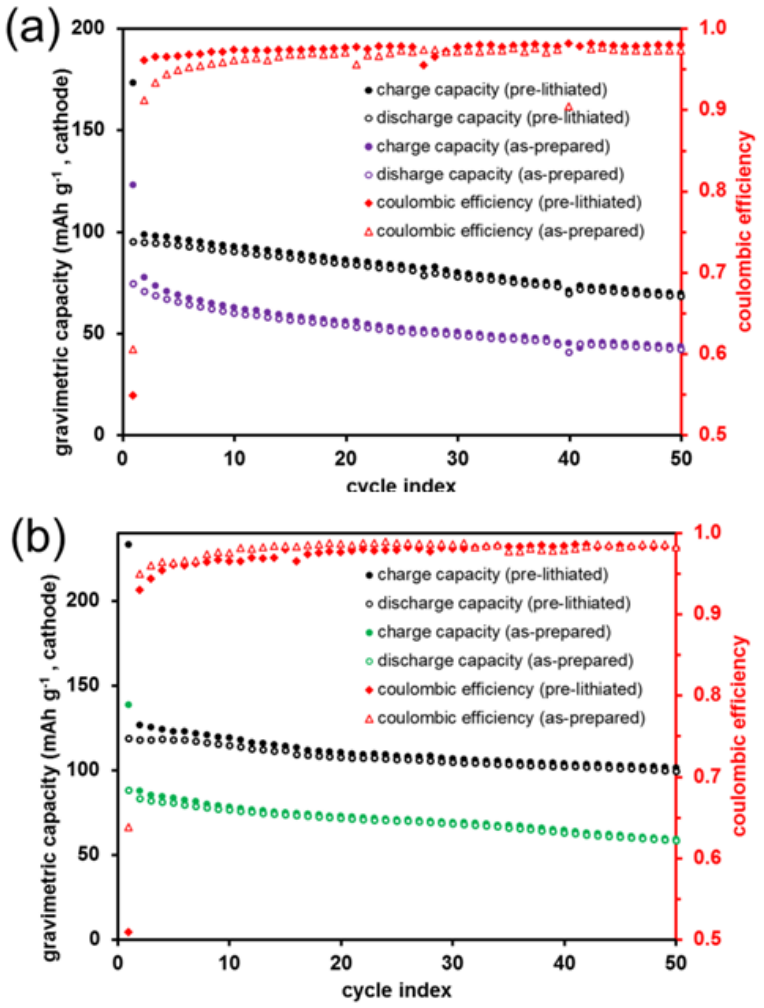

Figure 6.11 (a) Cyclability of the 4 V $Li_{1.05}Ni_{0.05}Mn_{1.9}O_4$ spinel / FeSb-TiC full cells and (b) of the 5 V $LiMn_{1.5}Ni_{0.5}O_4$ / FeSb-TiC full cells (as-prepared and pre-lithiated).

For these reasons, FeSb-TiC is an ideal anode to pair with pre-lithiated $LiMn_{1.5}Ni_{0.5}O_4$ or $Li_{1.05}Ni_{0.05}Mn_{1.9}O_4$ spinel cathodes in an effort to make a high powered lithium-ion battery. The microwave-assisted chemical lithiation process was used to add enough excess lithium to the spinel cathodes to combat the first-cycle losses associated with the FeSb-TiC composite and facilitate its use as an anode in a full cell. The 4 V and

5 V spinels chosen as the cathodes in these full cells were the samples subjected to microwave-assisted lithiation for 30 min. These cathodes displayed first cycle capacities of 178 mAh g^{-1} and 214 mAh g^{-1}, respectively, for the 4 V and 5 V spinels, both corresponding to a 1st cycle coulombic efficiency of 54%. Excess anode material (20% by capacity) was allowed to increase the overall cell voltage and to match the 1st cycle capacity of the cathodes. In subsequent cycles, only 80% of the anode practical capacity (~160 mAh g^{-1}) was then utilized.

For a comparison, full cells were also constructed with the as-prepared spinel samples to show the necessity of the extra lithium reservoir. The first charge/discharge curves of these cells are displayed in Figure 6.10. These curves categorically illustrate the effectiveness of storing extra lithium in a spinel cathode to combat the first cycle irreversibility of the FeSb anode. In the cells with the as-prepared spinels, almost half of the lithium ions initially stored in the cathode are robbed by the anode during its first cycle SEI layer formation. This is exhibited as reduced capacity of the entire cell. When the cathode is pre-lithiated by the microwave-assisted chemical lithiation, the extra lithium ions in the 16c sites are used during the first charge and the full cathode capacity can be utilized on subsequent discharge cycles (95 mAh g^{-1} or 118 mAh g^{-1}, respectively, for the 4 V and 5 V spinels). This is compared to the theoretical specific capacity of 112 mAh g^{-1} for $Li_{1.05}Ni_{0.05}Mn_{1.9}O_4$ and 146 mAh g^{-1} for $LiMn_{1.5}Ni_{0.5}O_4$. The energy densities of these cells by active material mass are: 193 mWh g^{-1} for the 4 V spinel and 263 mWh g^{-1} for the 5 V spinel. As a comparison, a full cell comprised of 5 V spinel and graphite (0% excess graphite by capacity) yields an energy density of 349 mWh g^{-1}. While the higher voltage vs. Li/Li^+ and lower specific capacity of the FeSb-TiC anode contributes to lower overall cell energy density compared to graphite, there are other aspects of

FeSb-TiC that make it attractive as an anode to pair with the $LiMn_{1.5}Ni_{0.5}O_4$ spinel cathode.

A chart displaying the cyclability of the spinel / FeSb-TiC cells at C/4 rate (C = 146 mA g^{-1} based on cathode active mass) over 50 cycles is shown in Figure 6.11. It is interesting to note that the full cell employing the 5 V spinel as the cathode, even with its higher voltage, exhibits better long-term stability than the full cell with the 4 V spinel cathode. Nonetheless, the necessity of the extra lithium in the pre-lithiated samples is evident - the cells comprised of cathodes which were not subjected to microwave-lithiation possess much lower capacity and energy density. This is expected and occurs whenever an anode with high first-cycle irreversibility is paired with a lithiated cathode. The data in Figure 6.11 also show that the capacity fade rates in these full cells are similar for the pre-lithiated and the as-prepared spinel cathodes. This demonstrates that the lithiation step has no adverse effect on the long-term cyclability of the spinel in full cells.

That being said, both of these cells (4 V and 5 V) suffer from the same problem experienced by high-voltage spinel / graphite full cells - that is, time dependent capacity fade stemming from Mn dissolution.[34,140,154] The dissolved Mn^{2+} is reduced onto the anode surface where a continuous SEI layer formation occurs, robbing lithium which would otherwise participate in reversible charge and discharge.[34] The fade rate of the 4 V $Li_{1.05}Ni_{0.05}Mn_{1.9}O_4$ / FeSb-TiC cell is 2.3% per day and that of the 5 V $LiMn_{1.5}Ni_{0.5}O_4$ / FeSb-TiC cell is 1.4 % per day.

This time dependent capacity fade is a major problem facing the implementation of high-voltage spinel in many full cells, so a side-by-side comparison of the fade rate of $LiMn_{1.5}Ni_{0.5}O_4$ / graphite and $LiMn_{1.5}Ni_{0.5}O_4$ / FeSb-TiC cells was performed. In Figure 6.12a, it can clearly be seen that the fade rate is significantly improved by substituting

FeSb-TiC for graphite. The fade rate of the graphite full cell is 2.3% per day, which is much higher than that of the FeSb-TiC full cell (only 1.4% per day). While this is a definite improvement, this problem would still need to be solved either by coating the cathode surface,[155] employing alternative electrolytes and additives,[154] or introducing an advanced separator.[156]

The FeSb-TiC anode offers another important advantage over graphite in full cells with a 5 V spinel cathode, namely faster charge rate capability. These data can be seen in Figure 6.12b. At a constant current 2C charge rate, the full cell with FeSb-TiC maintains 84% capacity retention. At 10C rate, the retention drops to 55%. After 10 cycles at 10C charge, the cell maintains good capacity retention upon cycling at C/4 rate with 93% of the initial capacity, demonstrating the cell's ability to maintain high capacity after being subjected to very fast charge cycles. The discharge rate capability of the $LiMn_{1.5}Ni_{0.5}O_4$ full cell can be seen in Figure 6.12c, with 84% capacity retention at 2C and 62% retention at 10C discharge rates. In comparison, as seen in Figure 6.12b, the 5 V spinel / graphite cell only retains 62% of its capacity at a 2C charge rate and a meager 22% at a 10C charge rate.

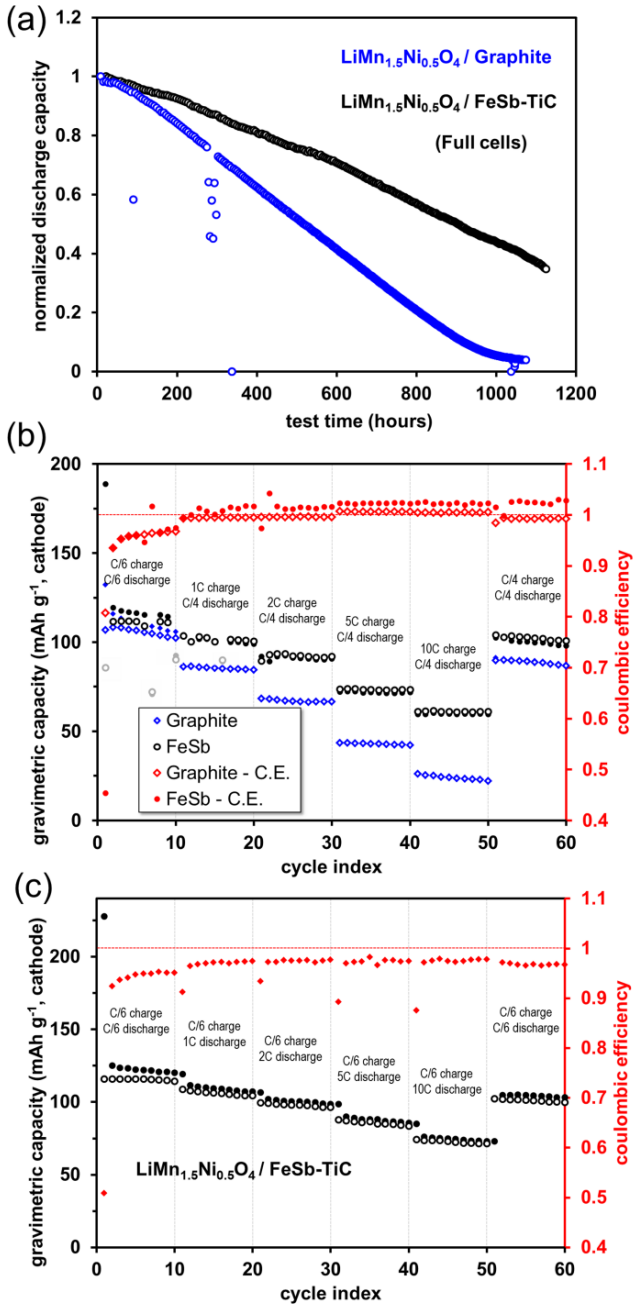

Figure 6.12 (a) Long-term time dependent capacity fade and (b) charge rate capability of $LiMn_{1.5}Ni_{0.5}O_4$ / FeSb-TiC and $LiMn_{1.5}Ni_{0.5}O_4$ / Graphite full cells and (c) discharge rate capability of $LiMn_{1.5}Ni_{0.5}O_4$ / FeSb-TiC full cell. Closed black and blue markers refer to charge capacity while open markers denote discharge capacity. Red markers denote coulombic efficiency (C.E.).

Based on the data presented here, of the two cathode varieties (4 V and 5 V) the 5 V spinel is a much better match for the FeSb-TiC anode because of its higher voltage vs. Li/Li^+ (leading to a significantly increased energy density) and superior long-term cycling stability. The $LiMn_{1.5}Ni_{0.5}O_4$ / FeSb-TiC lithium-ion cell shows promise and merits further investigation into electrolyte combinations and additives, perhaps PC and DMC based electrolytes, and different cathode doping schemes, *i.e.* Cr, Fe, or Co doped spinels, which have been shown in some cases to improve the cyclability, especially at high temperature.[82,157] Ways to solve the time-dependent capacity fade problem must also be addressed. This full cell manages to store more energy than a LMNO/LTO lithium-ion cell yet maintains good charge rate capability.

6.4 CONCLUSION

In lithium-ion batteries with large first cycle irreversibility problems stemming from significant SEI layer formation on the anode surface, excess lithium stored in the cathode can be used as a reservoir to supply the ions needed for SEI layer formation.

A facile approach to building a lithium reservoir in a spinel cathode without the use of metallic lithium or exotic or expensive chemicals has been described. Using a microwave-assisted chemical lithiation technique, lithium was inserted into the 16c octahedral sites of the 4 V $Li_{1.05}Ni_{0.05}Mn_{1.9}O_4$ and 5 V $LiMn_{1.5}Ni_{0.5}O_4$ spinel host structures which could then be used as cathodes in lithium-ion full cells. The full cells could be assembled without addition of metallic lithium or anode preconditioning. The current synthesis technique does not require an inert atmosphere or moisture control.

In the case of the anode used in this study, the composite intermetallic alloy FeSb-TiC, the irreversible capacity was approximately 65-69% of the stable capacity. In order to provide a good match to the anode, cathodes with similar first cycle efficiencies were

chosen. The full cells explored here, utilizing a combination of lithiated 4 V or 5 V spinel cathodes and the FeSb-TiC anode, demonstrated their ability to compensate for the first-cycle anode irreversibility. When the as-prepared spinel cathodes were used without the lithiation step, the reversible capacity was reduced by almost half. The full cells with the 5 V spinel cathode performed much better than their 4 V counterparts but still suffer from the same problems that plague high-voltage spinel / graphite full cells. Optimization of the electrolyte and additives, introduction of a novel separator, or coating the active material could provide enhancements to performance and stabilize the capacity fade. In theory, this technique presented here could be used to pair 4 V or 5 V spinel with any anode with irreversible capacity up to 50% such as nanostructured TiO_2, Si, metal-oxides, and other metal alloys.

Chapter 7: A Rapid Microwave-assisted Solvothermal Approach to Lower-valent Transition-metal Oxides

7.1 Introduction

With the recent global interest in renewable energy and energy efficiency, "green" synthesis techniques are being explored in an effort to curb industrial energy usage and waste.[158] Conventional inorganic synthesis procedures, particularly reduction of transition-metal oxides to obtain lower-valent oxides, often require high temperatures with long dwell times in hydrogen atmospheres, consuming large amounts of energy. Moreover, these high-temperature procedures are prohibitive to the formation of metastable phases having atypical valence states that may exhibit unique chemical and physical properties of interest to chemists and physicists.[159] With an aim to overcome this limitation, soft chemistry methods employing borohydride,[159] polyol,[57] sol-gel,[160] and alcohols[161] have been explored to obtain transition-metal oxides with reduced valence states. An alternative approach to obtain reduced transition-metal oxides and metal powders is microwave-assisted hydrothermal/solvothermal processing. Utilized extensively in organic syntheses, microwave-assisted techniques offer a variety of advantages over traditional high-temperature methods: lower reaction temperatures, shorter reaction times, and more efficient energy usage.[51,52,162–164] The polyol reduction technique has been a popular method to combine with microwave synthesis because of the high boiling point of dihydroxy alcohols and their ability to absorb microwave radiation due to the polar nature of the molecules.[52,163] Microwave irradiation allows the polyol solution to reach the steady-state hold temperature much faster, more efficiently,

---

Z. Moorhead-Rosenberg, E. Allcorn, & A. Manthiram. *In-situ* mitigation of first-cycle anode irreversibility in a new spinel / composite alloy lithium-ion battery enabled via a microwave-assisted chemical lithiation process. *Chemistry of Materials. DOI: 10.1021/cm5024426* (2014). E. Allcorn provided the anode materials and A. Manthiram supervised the project.

and more evenly than conventional heating because of the direct dielectric heating and forced convection of the liquid.

While the microwave-assisted polyol method has been investigated as a route to produce transition-metals and transition-metal oxide nanoparticles (especially those composed of Cu) from solvated metal ion precursors,[52,163,165–169] the reduction of solid transition-metal oxide particles in a liquid medium under microwave radiation has not been explored. However, reductions of solid oxides in a liquid medium using conventional heating methods have been studied in the past. For example, one method utilizing a glycerol aqueous solution was employed by Tuysuz *et al.*[59] to obtain mesoporous CoO from a template Co_3O_4 precursor. This reaction took place over a course of 15 h and required a continuous flow of solution. Another related technique employed NaH as a reducing agent to extract oxygen from $La_4Ni_3O_{10}$ in a heated liquid environment for up to 10 days.[170]

In an effort to decrease the reduction reaction time, presented in this chapter is a green, ultra-fast microwave-assisted method for the reduction of a variety of binary and ternary transition-metal oxides using tetraethylene glycol as a reducing agent. Starting with powders of V_2O_5, MnO_2, Co_3O_4, and CuO, the respective reduced products V_4O_9, Mn_3O_4 or MnO, CoO, and Cu_2O or Cu metal were formed in 30 minutes at temperatures < 300 °C. Additionally, oxygen was extracted from powders of $SrMnO_3$, $SrFeO_{3-\delta}$, $LaCoO_3$, $LaNiO_3$, and $La_4Ni_3O_{10}$ by controlling the reaction temperature. The method presented here is a promising facile way of tuning the oxidation state of metal ions in oxides that may possess interesting variations in physical properties as a function of oxygen content; various rare earth nickelates such as $RNiO_{3-\delta}$ and $R_2NiO_{4+\delta}$ show changes in resistivity[111,171] and Neèl temperature[172] as a strong function of oxygen

nonstoichiometry. The giant magnetoresistance (GMR) effect in $SrFeO_{3-\delta}$ has been reported to be sensitive to the value of δ.[173]

7.2 EXPERIMENTAL

The starting materials V_2O_5, MnO_2, Co_3O_4, and CuO were purchased from Acros Organics (V_2O_5, 98%+), Alfa Aesar (MnO_2, 99.9%), and GFS Chemicals (Co_3O_4, 99.6% and CuO, 99.6%) and used without further purification. $SrMnO_3$, $LaCoO_3$, and $LaNiO_3$ were synthesized by a citrate-based sol-gel method as follows: stoichiometric amounts of $Mn(CH_3COO)_2$, $Co(NO_3)_2 \cdot 6H_2O$, $Ni(NO_3)_2 \cdot 6H_2O$, $La(NO_3)_3 \cdot 6H_2O$ or La_2O_3, and $Sr(NO_3)_2$ were dissolved in a small amount of deionized water and nitric acid under magnetic stirring on a hot plate. Citric acid was added in the ratio of 1:1 for each metal ion and then ammonium hydroxide solution was poured into the mixture to attain a pH value near 7. For the $SrMnO_3$ reaction, 1 mol of ethylenediaminetetraacetic acid (EDTA) was added per metal ion as a chelating agent in concert with the citric acid. The solution was stirred continuously and heated at ~ 95 °C until a gel was formed, at which point the stir bar was removed and the temperature was increased until the gel began to decompose into a powder. The resulting black powder was ground and heated in air at 600 °C for 4 h to remove unwanted carbonaceous products. The resulting powders were then fired at 1000 °C for 24 h, 700 °C for 6 h, and 700 °C for 4 h, respectively, to produce $SrMnO_3$, $LaCoO_3$, and $LaNiO_3$. $SrFeO_{3-\delta}$ was prepared by a previously reported oxalate coprecipitation method by firing at 900 ^oC for 5 h.[174] $La_4Ni_3O_{10}$ was synthesized by firing a co-precipitated hydroxide-carbonate at 1100 ^oC for 24 h as reported before.[175]

Reductions of the transition-metal oxides were carried out at various temperatures up to 300 °C for up to 30 minutes in an Anton-Paar Monowave 3000 microwave synthesis reactor. Specimens consisting of 0.5 g of oxide powder and 10 mL of TEG

were enclosed in a thick-walled 30 mL glass vessel and sealed by a hermetic membrane. The mixture was spun at 1200 rpm with a magnetic stir bar to keep the solid particles suspended uniformly in the TEG. Specimens were heated as fast as possible with a maximum power draw of 850 W during initial heating (steady state power was considerably lower). In all cases, the holding temperature as recorded by an infrared temperature sensor (between 160 and 300 °C) was reached in less than three minutes. The autogeneous pressure varied depending on the severity of the reaction conditions; in general higher temperatures produced higher pressures and the pressure was maintained throughout the hold cycle. Because the boiling point of TEG is above the highest temperature allowed by the microwave (300 °C), the pressure was usually only between 1 and 5 bar. After the 30 minute reaction time at the specified temperature (except for the $SrFeO_{3-\delta}$ specimens, which were held for only 10 minutes), the specimens were cooled to 55 °C and the product was centrifuged to remove the spent TEG. The samples were then washed twice with deionized water and thrice with acetone and then dried in air at 100 °C for 20 minutes.

X-ray diffraction (XRD) patterns were collected with a Rigaku Ultima powder diffractometer utilizing Cu *Kα* radiation with a 0.02° 2θ step size and a three second dwell time. Compositional analysis was accomplished using Rigaku's proprietary software, PDXL, and a whole powder pattern fit (WPPF) technique. PowderCell was used to perform Reitveld refinement of the V_4O_9 sample. Field-cooled magnetic susceptibility data of V_4O_9 were obtained with a Quantum Design SQUID magnetometer under a field of 1000 Oe as the sample was heated from 5 to 300 K.

Iodometric titration was employed to determine the oxidation state of the metal ions in the ternary oxides $SrMnO_3$, $SrFeO_{3-\delta}$, $LaNiO_3$, and their reduced analogues. Approximately 50 mg of the powder was dissolved by adding 15 mL of 10 wt% KI and

15 mL of 3.5 M HCl, and the solution was titrated against 0.03 M sodium thiosulfate solution employing starch as the indicator.

SEM images were acquired using a Quanta FEG 650 scanning electron microscope.

7.3 Results and Discussion

7.3.1 Binary Oxides

Binary oxides of the first-row transition series from Ti to Cu were subjected to the microwave solvothermal treatment in TEG, excluding Cr and Ni. Of these oxides, TiO_2 and Fe_2O_3 were not affected by the process, even at the most extreme reaction condition of 300 °C held for 30 minutes. The oxides Cr_2O_3 and NiO were not included because Cr^{3+} cannot be reduced to Cr^{2+} in an oxide and the redox potential of $Ni^{2+/1+}$ is far too high. Because the transition metal 3d electron energies decrease from left to right across the periodic table, the $Ti^{3+/2+}$, $Cr^{3+/2+}$, $Fe^{3+/2+}$, and $Ni^{2+/1+}$ redox couples lie above the highest occupied molecular orbital (HOMO) of TEG, whereas the redox couples of $V^{5+/4+}$, $Mn^{4+/3+}$, $Mn^{3+/2+}$, $Co^{3+/2+}$, $Cu^{2+/1+}$, and $Cu^{1+/(m)}$ lie below the HOMO. Hence, the oxides V_2O_5, MnO_2, Co_3O_4, and CuO are able to be reduced by TEG and TiO_2, Cr_2O_3, Fe_2O_3, and NiO are not.

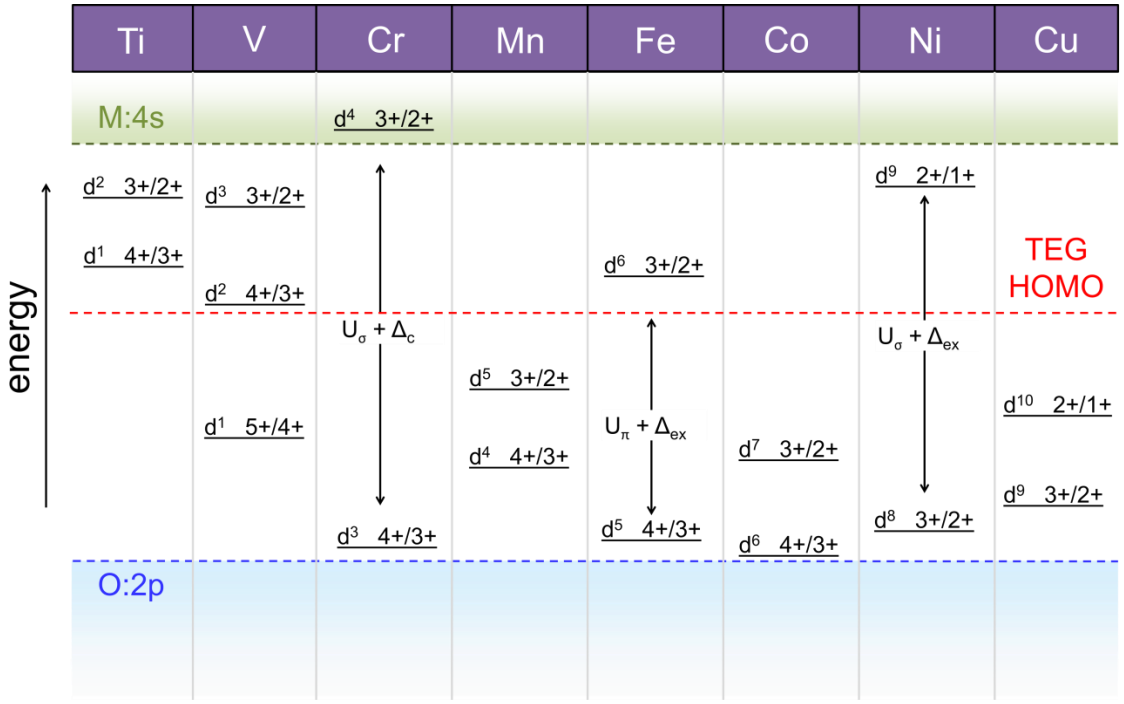

Figure 7.1 Qualitative redox couple energies of the 3d transition metals in octahedral coordination. All oxides with couples below the red dotted line are able to be reduced by TEG. Uπ and Uσ represent, respectively, the electrostatic potential energy U required to place an electron in a π-bonding t orbital and a σ-bonding e orbital. Δ_c and Δ_{ex} represent, respectively, the crystal field splitting and the intra-atomic exchange interaction associated with electron pairing.

A qualitative diagram of the transition metal redox couple energies in octahedral coordination with oxygen is displayed in Figure 7.1. Ti^{4+} in TiO_2 is d^0 with no 3d electrons. Because Ti is the first transition element and the intra-atomic exchange stabilization is low, the $Ti^{4+/3+}$ and $Ti^{3+/2+}$ redox couples lie very high in the gap between the full O:2p and empty Ti:4s states. These states are higher than the HOMO of TEG, and so TiO_2 is not reduced. V^{5+} in V_2O_5 is also d^0, but the stabilization from the extra proton in the V nucleus pulls the d electron energies down sufficiently that the $V^{5+/4+}$ couple is low enough that TEG can partially reduce V^{5+} to V^{4+}. In Cr_2O_3, the crystal field splitting and electrostatic repulsion term, U_σ, associated with placing an electron in an *e* orbital

which forms a σ-bond with oxygen are so high that the $Cr^{3+/2+}$ couple is pushed well above the metal 4s band edge so Cr^{2+} is not stable. The $Mn^{3+/2+}$ couple is lower than $Cr^{3+/2+}$ because of the higher nuclear charge of Mn and the intra-atomic exchange stabilization associated with a high-spin d^5 state. Because $Mn^{4+}O_2$ is reducible to $Mn^{2+}O$ in TEG, these two stabilizations must be enough to pull the $Mn^{3+/2+}$ couple below the HOMO of TEG. The $Fe^{3+/2+}$ couple is slightly higher than $Mn^{3+/2+}$ due to intra-atomic exchange associated with adding an electron with opposite spin, and is pushed too high for Fe^{3+} to be reduced by TEG. For the same reason, the $Ni^{2+/1+}$ couple is too high so NiO remains unaffected by the reaction. Co and Cu are far enough right on the periodic table that their d^7 and d^{10} states, respectively, are sufficiently stabilized as to be lower in energy than the TEG HOMO.

The XRD patterns of the starting V_2O_5 and the products formed from it are shown in Figure 7.2a. The reduction of V_2O_5 to the reduced product V_4O_9 was complete in 30 minutes of microwave irradiation at 180 °C. This is particularly interesting because V_4O_9 has proven difficult or impossible to synthesize by conventional means, and has only recently been obtained and characterized in single-phase form by Yamazaki *et al*[176] by a sulfur powder reduction technique.

The ICDD database lists V_4O_9 as a tetragonal phase based on the work of Theòbald *et al*.[177] However, the peak indexing of our obtained powder pattern to the tetragonal symmetry was unsatisfactory. In addition, the peak at 10.5° could not be accounted for based on the tetragonal symmetry. It has been reported previously that V_4O_9 is in fact orthorhombic and not tetragonal as confirmed by electron diffraction (ED).[176,178,179] The orthorhombic *Cmcm* structure proposed by Yamazaki *et al*[176] proved to be much more reliable and all peaks could be indexed based on orthorhombic symmetry. A Reitveld analysis resulted in a satisfactory calculation as displayed in

Figure 7.3a with a slightly high Rwp of 16.19% owing to the poor crystallinity of the sample. The lattice parameters reported in this work are compared to previous calculations in table 7.1.

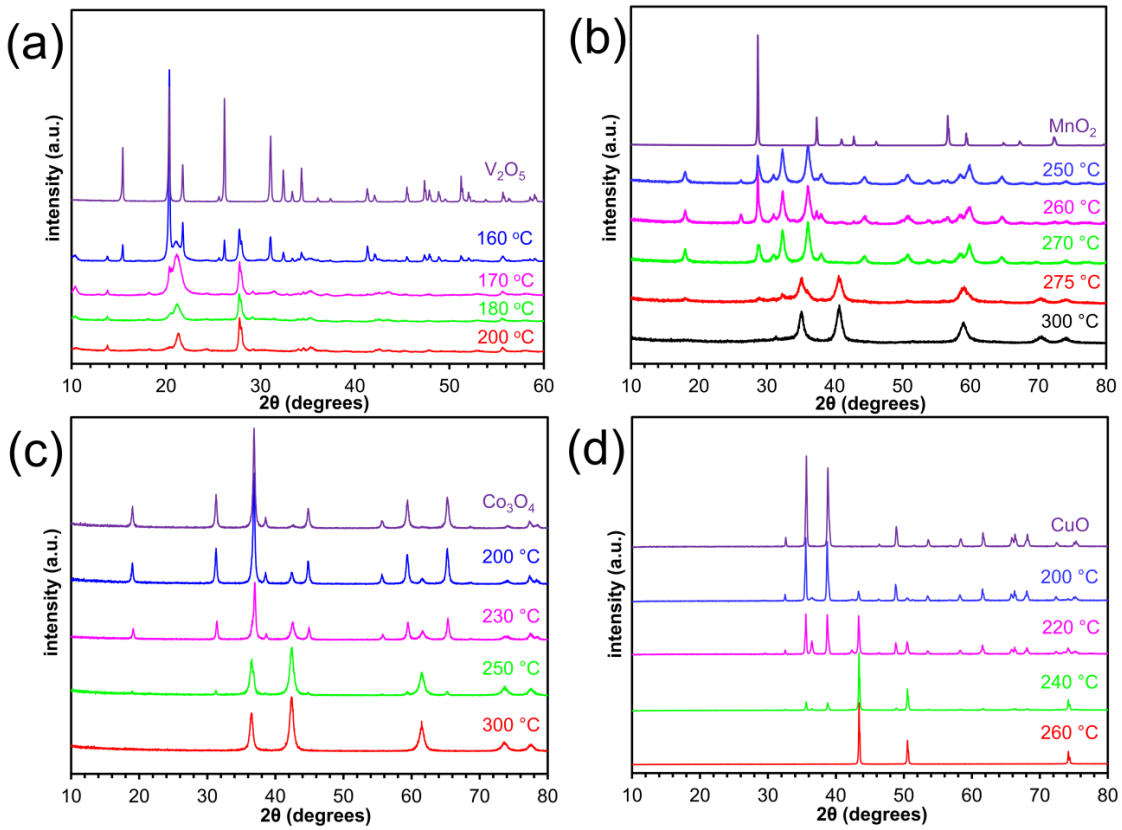

Figure 7.2 X-ray powder diffraction patterns of (a) V_2O_5, (b) MnO_2, (c) Co_3O_4, (d) CuO and the products formed from each with the microwave-assisted reduction process at the indicated temperatures. In each case the hold time was 30 min.

Table 7.1 Lattice parameters of V_4O_9

Reference:	Tilley & Hyde[178]	Grymonprez *et al.*[179]	Yamazaki *et al.*[176]	This Work
Method:	ED	ED	XRD	XRD
a (Å)	8.1	8.235	10.356 (2)	10.40 (1)
b (Å)	10.4	10.32	8.174 (1)	8.13 (1)
c (Å)	16.1	16.47	16.559 (3)	16.65 (1)

Note that *a* and *b* values are reversed for Tilley & Hyde[178] and Grymonprez *et al.*[179]

To further confirm the formation of V_4O_9, the product obtained from the reduction of V_2O_5 at 200 °C was examined by a SQUID magnetometer. The V^{4+}:$3d^1$ ion in V_4O_9 contains a single unpaired electron, so any reduction of V^{5+} to V^{4+} can be verified by examining the magnetic susceptibility behavior. V_2O_5 with V^{5+}:$3d^0$ ions having no unpaired electrons is diamagnetic. The variation of inverse molar magnetic susceptibility with temperature shown in Figure 7.3b indicates a linear Curie-Weiss paramagnetic behavior above 150 K with a Curie constant of 0.61. This corresponds to an effective magnetic moment μ_{eff} of 2.21 μ_B which is close to the theoretical spin-only value of 2.45 μ_B obtained by assuming 2 V^{4+} magnetic centers per formula unit.

X-ray diffraction patterns of MnO_2, Co_3O_4, CuO, and their respective reduced products can be seen, respectively, in Figure 7.2b, c, and d. The transformation of MnO_2 (pyrolusite) to MnOOH (manganite), Mn_3O_4 (hausmannite), and finally MnO (manganosite), via microwave-assisted reduction in TEG is detailed in Table 7.2. After a 270 °C run for 30 minutes, phase-pure Mn_3O_4 is formed. Likewise, phase-pure MnO can be obtained by microwaving the MnO_2 powder at 300 °C for 30 minutes. Co_3O_4 forms a cubic spinel structure, with Co^{2+} and Co^{3+} ions respectively occupying the 8a tetrahedral sites and 16d octahedral sites. At reaction temperatures between 200 °C and 250 °C, the

products formed are two-phase mixtures of Co_3O_4 and CoO. However, after 30 minutes under microwave radiation at 300 °C, pure CoO is formed. Among the 3d transition series oxides, CuO is the only one capable of being reduced to the metallic state by the method presented here. Cu is the last 3d transition metal element and possesses the lowest electron energies; consequently the Cu-oxides are the most easily reduced in TEG (At 300 °C in the microwave reactor, the conversion of CuO to Cu metal occurs in less than 5 minutes).

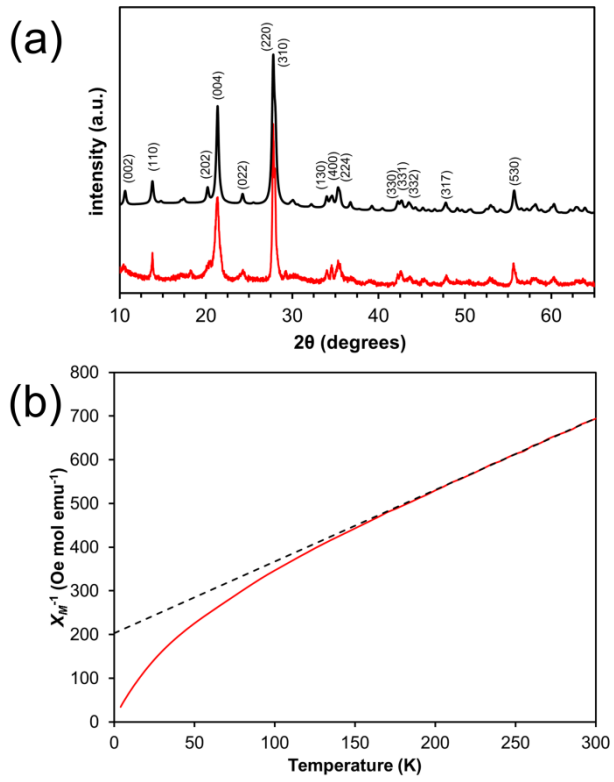

Figure 7.3 (a) the measured (red, bottom) and calculated (black, top) XRD patterns of V_4O_9 obtained at 200 °C according to the orthorhombic structure outlined by Yamazaki *et al.*[176] and (b) molar inverse magnetic susceptibility of V_4O_9. The dotted line represents the linear fit to the Curie-Weiss Law.

Table 7.2 Reduced binary oxides obtained by the microwave-assisted reduction process for 30 minutes

Starting Material	Hold Temperature	Product Formed
V_2O_5	180 °C	V_4O_9
V_2O_5	200 °C	V_4O_9
MnO_2	200 °C	MnO_2 (72%), MnO(OH) (28%)
MnO_2	260 °C	MnO_2 (33%), Mn_3O_4 (67%)
MnO_2	270 °C	Mn_3O_4
MnO_2	275 °C	Mn_3O_4 (49%), MnO (51%)
MnO_2	300 °C	MnO
Co_3O_4	200 °C	Co_3O_4 (84%), CoO (16%)
Co_3O_4	230 °C	Co_3O_4 (71%), CoO (29%)
Co_3O_4	250 °C	Co_3O_4 (9%), CoO (91%)
Co_3O_4	300 °C	CoO
CuO	200 °C	CuO (86%), Cu_2O (6%), Cu (8%)
CuO	220 °C	CuO (57%), Cu_2O (15%), Cu (28%)
CuO	240 °C	CuO (30%), Cu_2O (3%), Cu (67%)
CuO	260 °C	Cu

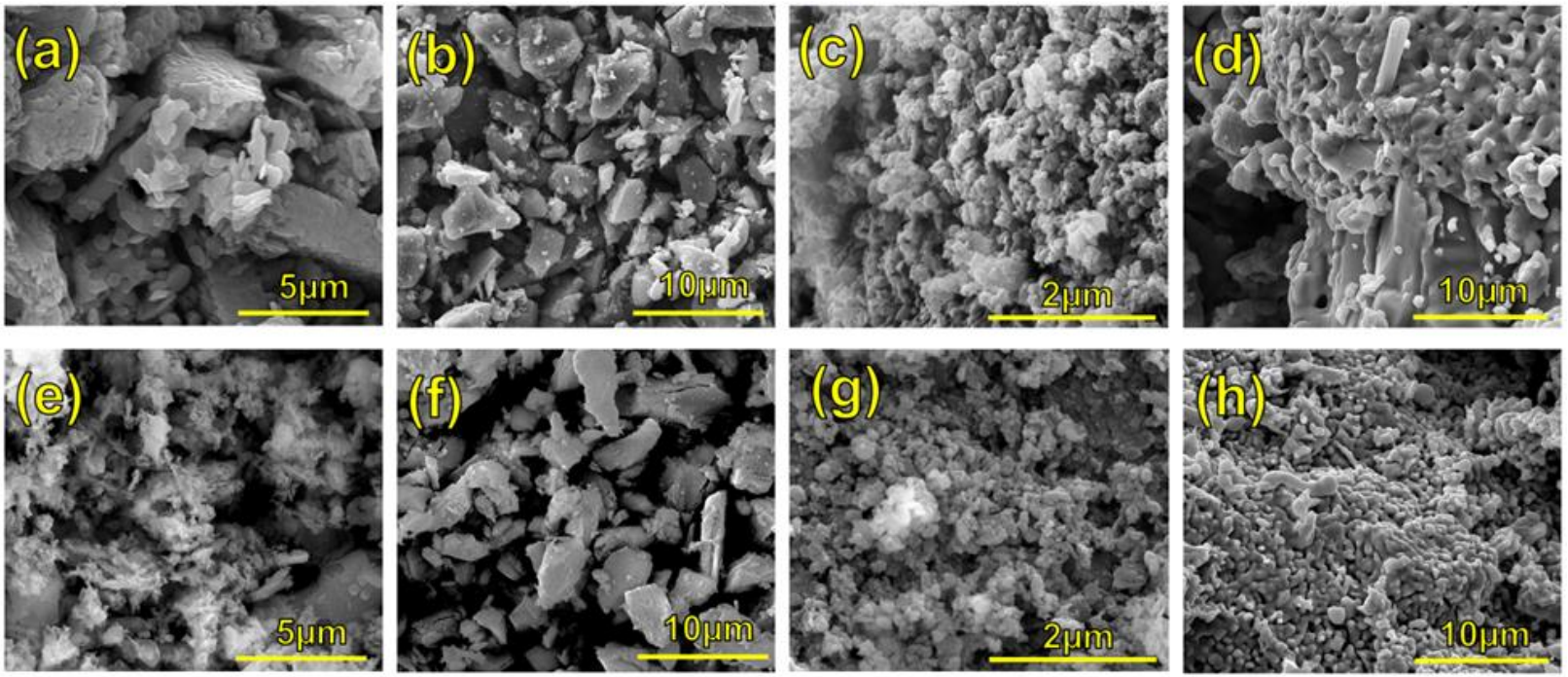

Figure 7.4 SEM images of the starting binary oxides: (a) V_2O_5, (b) MnO_2, (c) Co_3O_4, and (d) CuO; the reduced products at the most extreme microwave conditions listed in Table 7.2: (e) V_4O_9, (f) MnO, (g) CoO, (h) Cu.

SEM images of the binary oxides can be seen in Figure 7.4. It is interesting to note the morphology of the particles remains similar after the microwave reduction. This is because the reduction is a topotactic solid-state reaction rather than a dissolution-recrystallization reaction. However, some changes are visible, especially in the V and Cu samples, such as an apparent increase in surface roughness. The V_2O_5 to V_4O_9 transformation shows a noticeable change in particle size; the V_4O_9 particles are much smaller and have finer features than the starting material, V_2O_5. During the CuO to Cu transformation, the surface of the material also became much finer. Figure 7.4h displays some evidence of melting as small extruded or spherical droplets can be seen. This is expected for small powdered conductive materials which can absorb microwaves and achieve much higher temperatures than the bulk indicated temperature. Although it is more noticeable in the SEM micrographs of the Cu and V specimens, the surface area of all samples increased after the microwave reduction process according to BET measurements, displayed in table 7.3.

Table 7.3 BET surface area measurements

Starting Material	BET Surface Area (m^2/g)	Product after MW reduction	BET Surface Area (m^2/g)
V_2O_5	4.096	V_4O_9	9.449
MnO_2	2.121	MnO	18.366
Co_3O_4	23.258	CoO	25.288
CuO	0.332	Cu	4.711
$SrMnO_3$	1.66	$SrMnO_{2.61}$	5.704
$SrFeO_{2.73}$	1.121	$SrFeO_{2.48}$	2.948
$LaCoO_{2.97}$	4.14	$LaCoO_{2.63}$	7.523
$LaNiO_3$	6.268	$LaNiO_{2.53}$	7.203

7.3.2 Ternary Oxides

$SrMnO_3$ adopts a hexagonal 4H hexagonal perovskite structure unless it is slow cooled from high temperature in an inert atmosphere or rapidly quenched from the high-temperature perovskite phase.[180,181] The $SrMnO_3$ sample prepared for this study under ambient conditions in air had the hexagonal perovskite structure with face-shared octahedra as indicated by XRD. On the other hand, both $LaNiO_3$ and $SrFeO_{3-\delta}$ had the perovskite structures with corner-shared octahedra. The microwave-assisted solvothermal reductions of $SrMnO_3$, $LaCoO_3$, $LaNiO_3$, and $La_4Ni_3O_{10}$ were carried out at the indicated temperature for 30 minutes while those with $SrFeO_{3-\delta}$ were carried out for 10 minutes since the reduction reaction occurred rapidly with $SrFeO_{3-\delta}$.

According to iodometric titration, the as-prepared $SrMnO_3$ and $LaNiO_3$ samples are almost fully oxygenated with oxygen contents close to 3.0. The as-prepared $SrFeO_{3-\delta}$, on the other hand, is oxygen deficient with $\delta = 0.25$. Oxygen content values determined by the redox titration for each compound are given in Table 7.4.

When these materials are subjected to microwave irradiation in the TEG suspension, topotactic removal of oxygen from the lattice occurs with a concomitant reduction of the transition-metal ions. The redox couples present in the ternary oxides investigated here are Mn^{4+}/Mn^{3+}, Fe^{4+}/Fe^{3+}, Co^{3+}/Co^{2+}, and Ni^{3+}/Ni^{2+}. In the case of $SrFeO_{3-\delta}$ and $LaNiO_3$, the transition metals are completely reduced to their 3+ and 2+ oxidation states after being irradiated at 260 °C for 10 minutes and 240 °C for 30 minutes, respectively, to yield $Sr_2Fe_2O_5$ and $La_2Ni_2O_5$. The XRD patterns detailing the reductions of $SrMnO_{3-\delta}$, $SrFeO_{3-\delta}$, $LaCoO_{3-\delta}$, and $LaNiO_{3-\delta}$ can be seen in Figure 7.5.

Table 7.4 Reduced ternary oxides obtained by the microwave-assisted reduction

Starting Material	Hold Temperature	Oxygen Content (moles, 3-δ)	Oxidation State of the Transition Metal Ion
$SrMnO_{3-\delta}$	as-prepared	2.99	3.98
$SrMnO_{3-\delta}$	250 °C	2.71	3.62
$SrMnO_{3-\delta}$	270 °C	2.61	3.21
$SrFeO_{3-\delta}$	as-prepared	2.75	3.50
$SrFeO_{3-\delta}$	180 °C	2.73	3.46
$SrFeO_{3-\delta}$	200 °C	2.68	3.36
$SrFeO_{3-\delta}$	220 °C	2.62	3.24
$SrFeO_{3-\delta}$	240 °C	2.56	3.12
$SrFeO_{3-\delta}$	260 °C	2.48	2.95
$LaCoO_{3-\delta}$	as-prepared	2.97	2.95
$LaCoO_{3-\delta}$	240 °C	2.86	2.73
$LaCoO_{3-\delta}$	260 °C	2.79	2.57
$LaCoO_{3-\delta}$	280 °C	2.63	2.27
$LaCoO_{3-\delta}$	300 °C	2.63	2.26
$LaNiO_{3-\delta}$	as-prepared	3.00	3.00
$LaNiO_{3-\delta}$	200 °C	2.59	2.73
$LaNiO_{3-\delta}$	220 °C	2.76	2.49
$LaNiO_{3-\delta}$	240 °C	2.53	2.06
$LaNiO_{3-\delta}$	260 °C	2.53	2.06
$La_4Ni_3O_{10}$	as-prepared	10.0	2.67
$La_4Ni_3O_{10}$	300 °C	9.0	2.0

$SrFeO_{3-\delta}$ samples were held at the indicated temperature for 10 minutes while all other reactions were held for 30 minutes

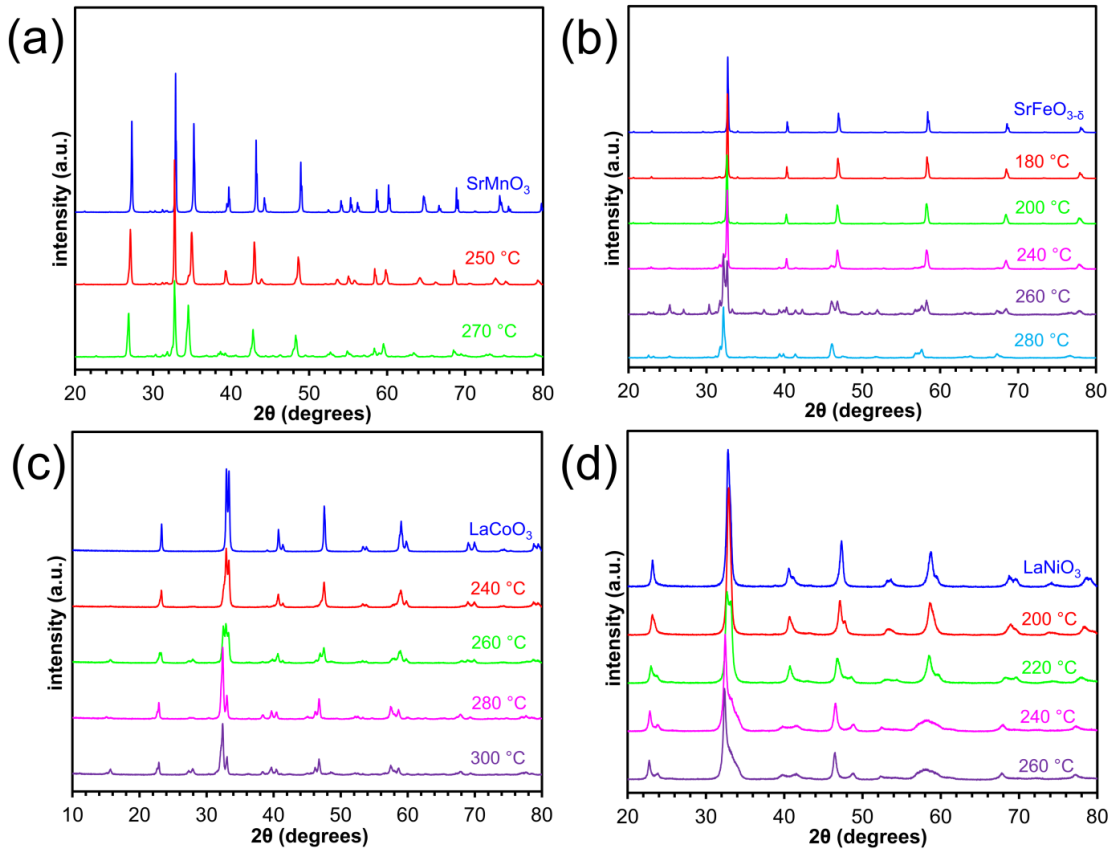

Figure 7.5 X-ray powder diffraction patterns of (a) $SrMnO_3$, (b) $SrFeO_{3-\delta}$, (c) $LaCoO_3$, (d) $LaNiO_3$ and the products formed from each with the microwave-assisted reduction process at the indicated temperatures. All hold times were 30 minutes except for the $SrFeO_{3-\delta}$ reduced products, in which case the hold time was 10 minutes.

$SrFeO_{2.5}$ is identified as brownmillerite phase based on the XRD data, while $LaNiO_{2.5}$ is identified as a monoclinic perovskite-like phase with ordered oxygen vacancies and both octahedral and square-coplanar coordinated Ni^{2+} ions. High-spin Fe^{3+} ions with a $3d^5$ configuration in $SrFeO_{2.5}$ have no particular preference for octahedral sites, so the brownmillerite phase with both tetrahedrally and octahedrally coordinated Fe^{3+} ions is formed. Ni^{2+} ions with a $3d^8$ configuration in $LaNiO_{2.5}$, on the other hand, do not prefer tetrahedral coordination, so the reduced Ni ions remain in octahedral

coordination or take on square-planar coordination. Compositions with oxygen contents above 2.5 were obtained at temperatures below 300 °C as shown by the chemical analysis data in Table 7.4.

According to XRD and titration data (within error), the most reduced phase of $LaCoO_3$ obtained was the intermediate phase $La_3Co_3O_8$ with an average Co oxidation state of +2.33. This product forms as a hybrid of the perovskite and brownmillerite structures with alternating layers of tetrahedrally coordinated Co ions separated by two perovskite layers along the c-axis.[182]

In the case of $SrMnO_3$,complete reduction of Mn^{4+} to Mn^{3+} was not attainable. At extended dwell times or temperatures higher than 270 °C, the $SrMnO_{3-\delta}$ composition broke down and formed various Sr and Mn-rich oxides. The lowest achieved oxygen content for $SrMnO_{3-\delta}$ according to the iodometric titration data was 2.63 after irradiation at 270 °C for 30 minutes, which corresponds to an average Mn oxidation state of +3.26.

SEM images of the ternary oxides can be seen in Figure 7.6. To a greater extent than the binary oxides, the morphology of the particles looks very similar after reduction, save for the $SrFeO_{3-\delta}$ oxides. The $SrFeO_{3-\delta}$ particles noticeably shrunk in size after the reaction according to the images, similar to the V_2O_5 to V_4O_9 transformation. Because the $SrFeO_{3-\delta}$ to $SrFeO_{2.5}$ reaction occurred quite rapidly compared to the others, it is possible that the grains were subjected to rapid strain and crumbled during the reduction process, producing much smaller product grains. Contrastingly, the Mn, Co, and Ni-based perovskites maintained their morphology after the reduction reaction although their surface area displayed a notable increase according to BET analysis (table 7.3).

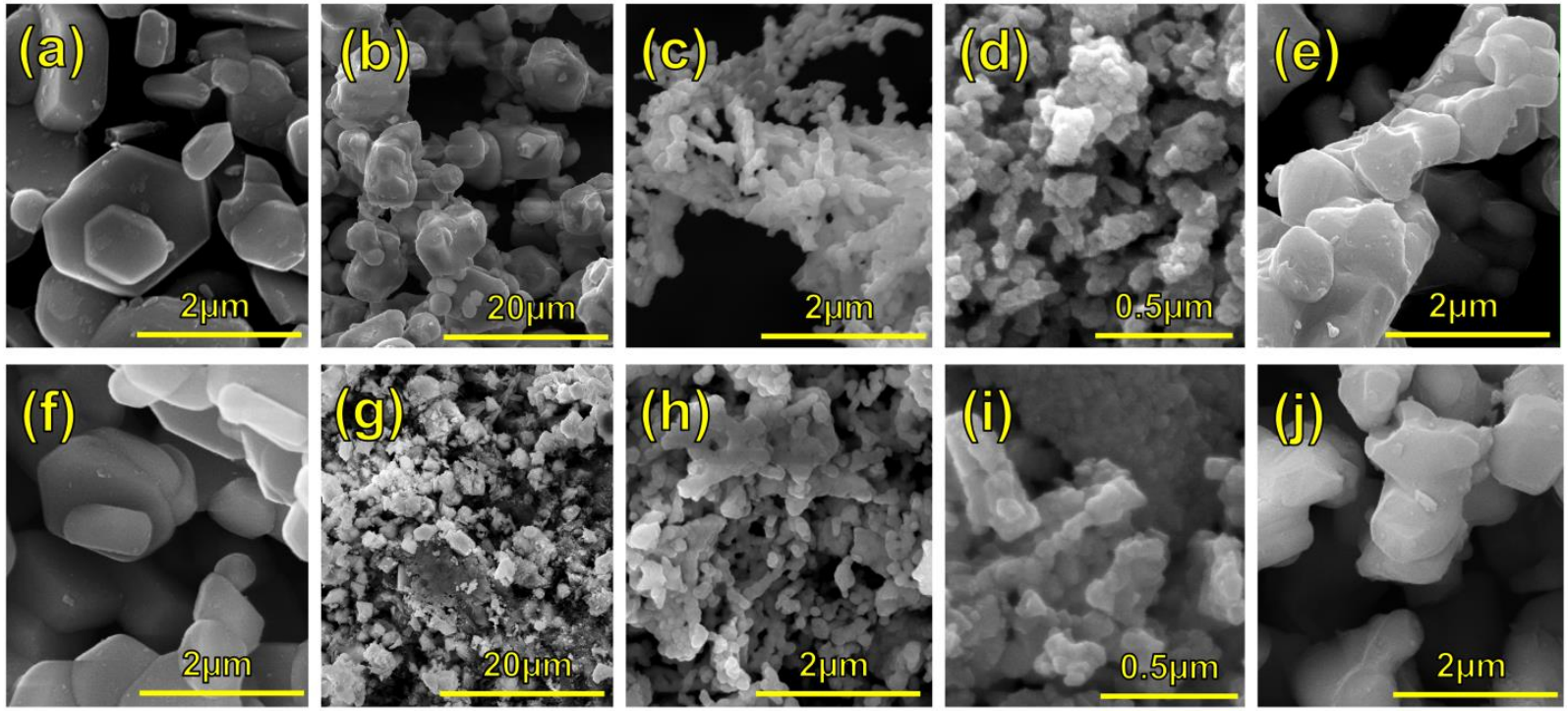

Figure 7.6 SEM images of the starting ternary oxides (a) $SrMnO_{2.99}$, (b) $SrFeO_{2.73}$, (c) $LaCoO_{2.97}$, (d) $LaNiO_{3.00}$, and (e) $La_4Ni_3O_{10}$ and the final products at the most extreme conditions listed in table 4: (f) $SrMnO_{2.61}$, (g) $SrFeO_{2.48}$, (h) $LaCoO_{2.63}$, (i) $LaNiO_{2.53}$, and (j) $La_4Ni_3O_9$.

In an effort to demonstrate the applicability of this microwave-assisted solvothermal reduction method to other crystal structures such as those of the Ruddleson-Popper series, $La_4Ni_3O_{10}$ was subjected to the microwave-assisted reduction process at 300 °C for 30 minutes. Materials of the Ruddleson-Popper series and other structures related to the perovskite family often possess interesting electronic properties that vary considerably with oxygen content; $La_4Ni_3O_{10}$ is one such material.[183] The XRD patterns of $La_4Ni_3O_{10}$ and the reduced product formed from it can be seen in Figure 7.7. The XRD data reveal that the product formed at 300 °C for 30 minutes is $La_4Ni_3O_9$ with an oxidation state of 2+ for Ni. A previous synthesis of the $La_4Ni_3O_{10-\delta}$ series involved a more complex electrochemical method to controllably extract oxygen.[183] The microwave-assisted reduction with TEG can quickly produce powdered oxides with easily controllable oxygen content by varying the synthesis temperature. This process will be useful for preparing other metal oxides with variable oxygen content for electronic, magnetic, and chemical studies.

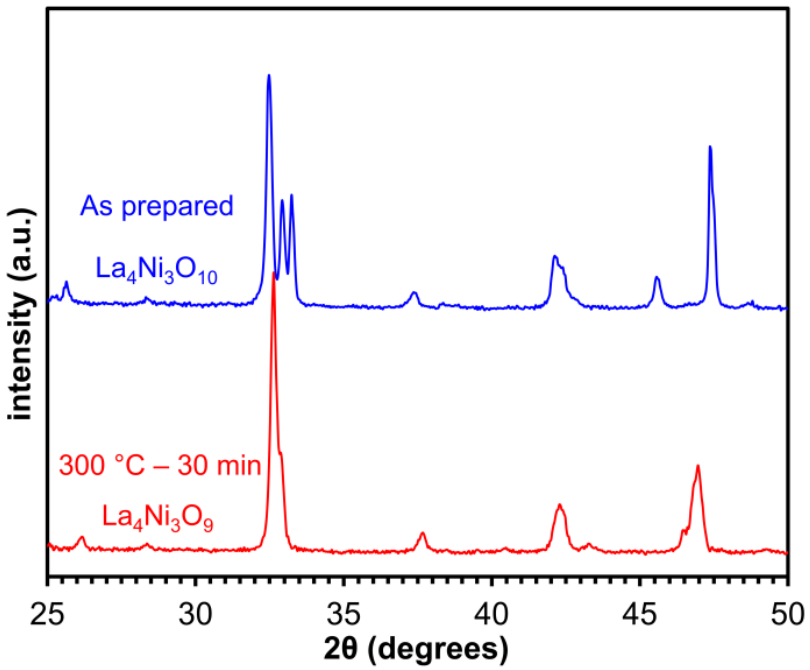

Figure 7.7 X-ray powder diffraction patterns of as-prepared $La_4Ni_3O_{10}$ and the reduced product, $La_4Ni_3O_9$, after microwave irradiation at 300 °C for 30 minutes.

7.4 Conclusion

A facile, microwave-assisted solvothermal technique for the reduction of solid transition-metal oxides utilizing tetraethylene glycol as a reducing agent was developed. The process presented here consumes only a fraction of the time and energy required by conventional high-temperature and alternative soft-chemistry methods. This is particularly enticing, considering the recent interest in green, energy-efficient synthesis procedures. Additionally, this technique provides a quick and highly-controllable way to extract oxygen from perovskite and perovskite-like powders with interesting physical properties that vary with oxidation state. Further work is in progress to extend this technique to pelletized and single-crystal specimens so that more precise physical property measurements could be carried out and correlated to oxygen content values.

Chapter 8: Summary

The aim of this dissertation was to examine the physical properties of high-voltage spinel as they relate to the performance in a lithium-ion electrochemical cell. High-voltage spinel possesses rich crystal chemistry and intriguing properties which made it an ideal cathode to study.

In Chapters 3 and 4, the magnetic properties of $LiMn_{1.5}Ni_{0.5}O_4$ (LMNO) were examined. A reliable, fast, and accurate method to determine the Mn^{3+} content was developed and applied to stoichiometric spinel and Ni-substituted spinel. Mn^{3+} content is important to electrochemical performance as it controls the shape of the cathode voltage profile during charge and discharge. The magnetic transition temperature was also examined as a measure of the degree of Mn-Ni long-range cation ordering.

In Chapter 5, the electronic conductivity, carrier activation energy, thermoelectric effect, and phase transformation mechanisms were methodically analyzed in four high-voltage spinel samples with varying degrees of cation order. These measurements were correlated to the power capability in lithium-ion half-cells. The long-standing belief that Mn^{3+} content is important to performance (as it increases the electronic conductivity in the as-prepared compound, $LiMn_{1.5}Ni_{0.5}O_4$) was challenged. An alternative theory was proposed: kinetically formed solid solutions below 50% state of charge ($Li_{0.5+x}Mn_{1.5}Ni_{0.5}O_4$) may be critical to rate performance.

Chapter 6 explored a new microwave-assisted chemical lithiation technique using common, non-toxic, inexpensive, and stable chemicals at moderate temperaturea (~ 200 ^oC) for the enhancement of capacity in lithium-ion full-cells utilizing high-voltage spinel as a cathode. Spinel was combined with a nanocomposite alloy anode, FeSb-TiC, to create a brand-new high rate cell chemistry. The first cycle irreversible consumption of lithium by nanocomposite anodes is high, and the lithium reservoir provided by the

chemical lithiation technique was able to fully compensate for this irreversibility. The energy density achieved in the LMNO//FeSb-TiC cell was higher than that of the LMNO//$Li_4Ti_5O_{12}$ (LTO) cells with comparable rate capability. The time-dependent capacity fade was also improved compared to LMNO//graphite cells by a factor of two. In Chapter 7, the microwave-assisted technique was extended to the reduction of binary and ternary first-row transition metal oxides. The elusive compound, V_4O_9, was successfully synthesized (confirmed by magnetic measurements and XRD) with this technique from V_2O_5 solid precursor. Other ternary oxides, mostly perovskites, were also reduced as confirmed by redox titrations.

The task of successfully implementing the high-voltage spinel in practical lithium-ion cells is challenging, but progress is being made each year towards its successful development. The data and techniques shared in this dissertation add to our knowledge of the mechanism at play in high-voltage spinel and how we can control them to make a better lithium-ion battery. While other cathodes and "beyond lithium-ion" chemistries may offer higher energy density in the future, high-voltage spinel may find a place as a niche cathode for super-high rate lithium-ion batteries.

Appendix A: List of Publications Related to this Work

1. Z. Moorhead-Rosenberg, D. Shin, K. Chemelewski, J.B. Goodenough, & A. Manthiram. Quantitative determination of Mn^{3+} content in $LiMn_{1.5}Ni_{0.5}O_4$ spinel cathodes by magnetic measurements. *Applied Physics Letters* 100, 213909 (2012).
2. Z. Moorhead-Rosenberg, K. Chemelewski, J.B. Goodenough, & A. Manthiram. Magnetic measurements as a viable tool to assess the relative degrees of cation ordering and Mn^{3+} content in doped $LiMn_{1.5}Ni_{0.5}O_4$ spinel cathodes. *Journal of Materials Chemistry A* 36, 10745-52 (2013).
3. Z. Moorhead-Rosenberg, K.L. Harrison, T. Turner, & A. Manthiram. A rapid microwave-assisted solvothermal approach to lower-valent transition metal oxides. *Inorganic Chemistry* 52(22) 13087-93 (2013).
4. Z. Moorhead-Rosenberg, E. Allcorn, & A. Manthiram. *In-situ* mitigation of first-cycle anode irreversibility in a new spinel / composite alloy lithium-ion battery enabled via a microwave-assisted chemical lithiation process. *Chemistry of Materials. DOI: 10.1021/cm5024426* (2014).
5. Z. Moorhead-Rosenberg, Ashfia Huq, John B. Goodenough, & A. Manthiram. Electronic and electrochemical properties of $Li_{1-x}Mn_{1.5}Ni_{0.5}O_4$ spinel cathodes as a function of lithium content and cation ordering. *(Submitted, Chemistry of Materials, 2015)*

Appendix B: Supporting Information for Chapter 5

Table B1 Neutron diffraction refinement parameters

Sample	χ^2	R_{wp} (histogram 1)	R_{wp} (histogram 2)
SC	24.57	0.0519	0.1038
A48	48.89	0.0581	0.1414
A240	26.36	0.0443	0.1097

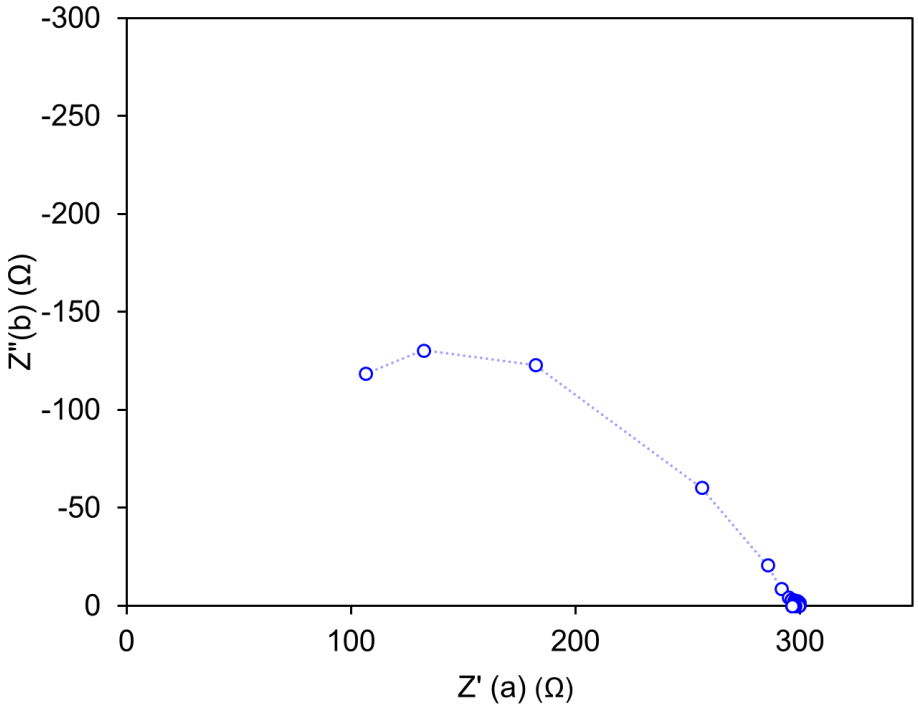

Figure B1 Impedance measurement of the delithiated SC sample to a lithium content of 0.21. Only one major impedance arc is observed (typical).

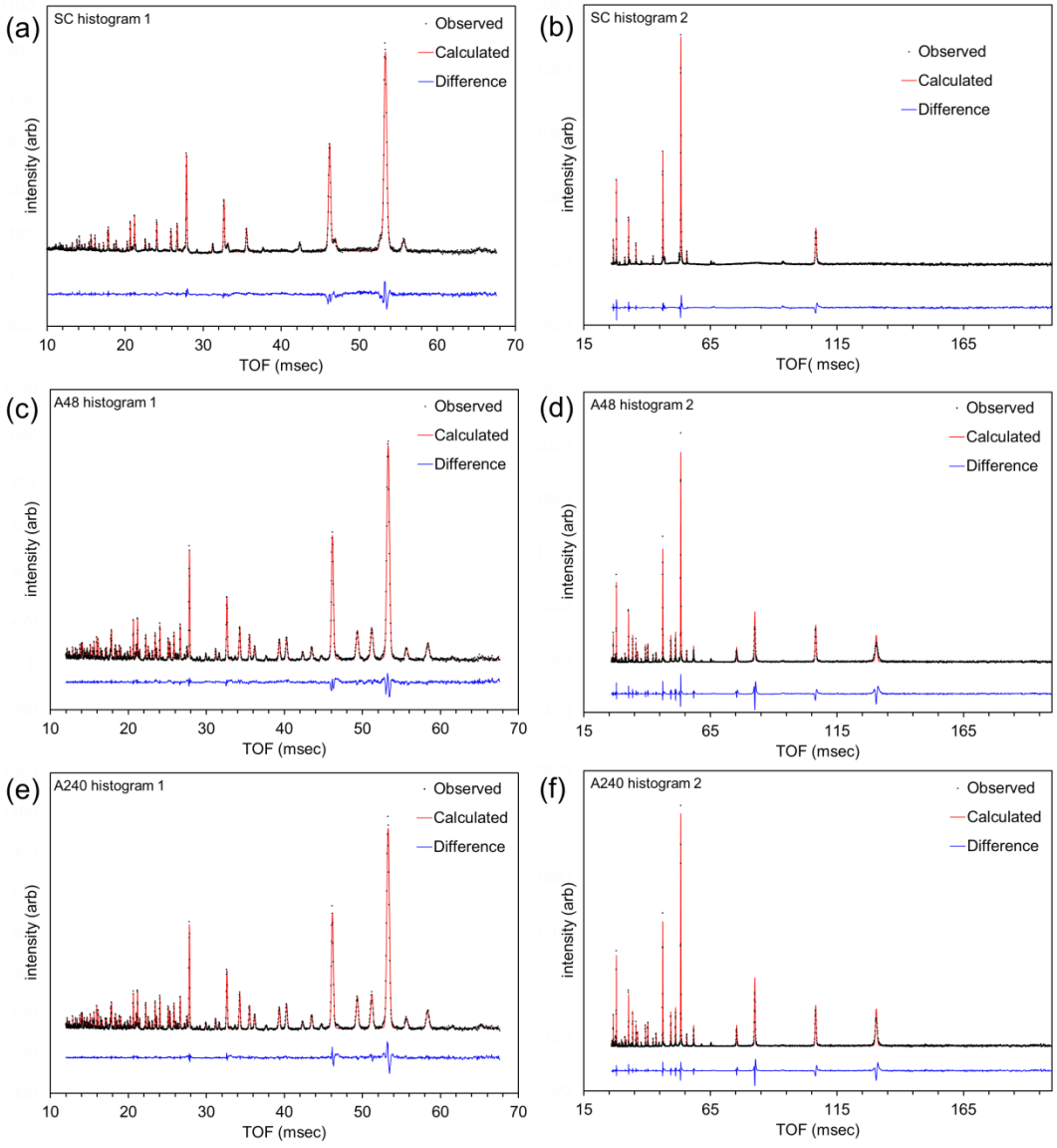

Figure B2 Neutron diffraction patterns and Rietveld refinements from GSAS.

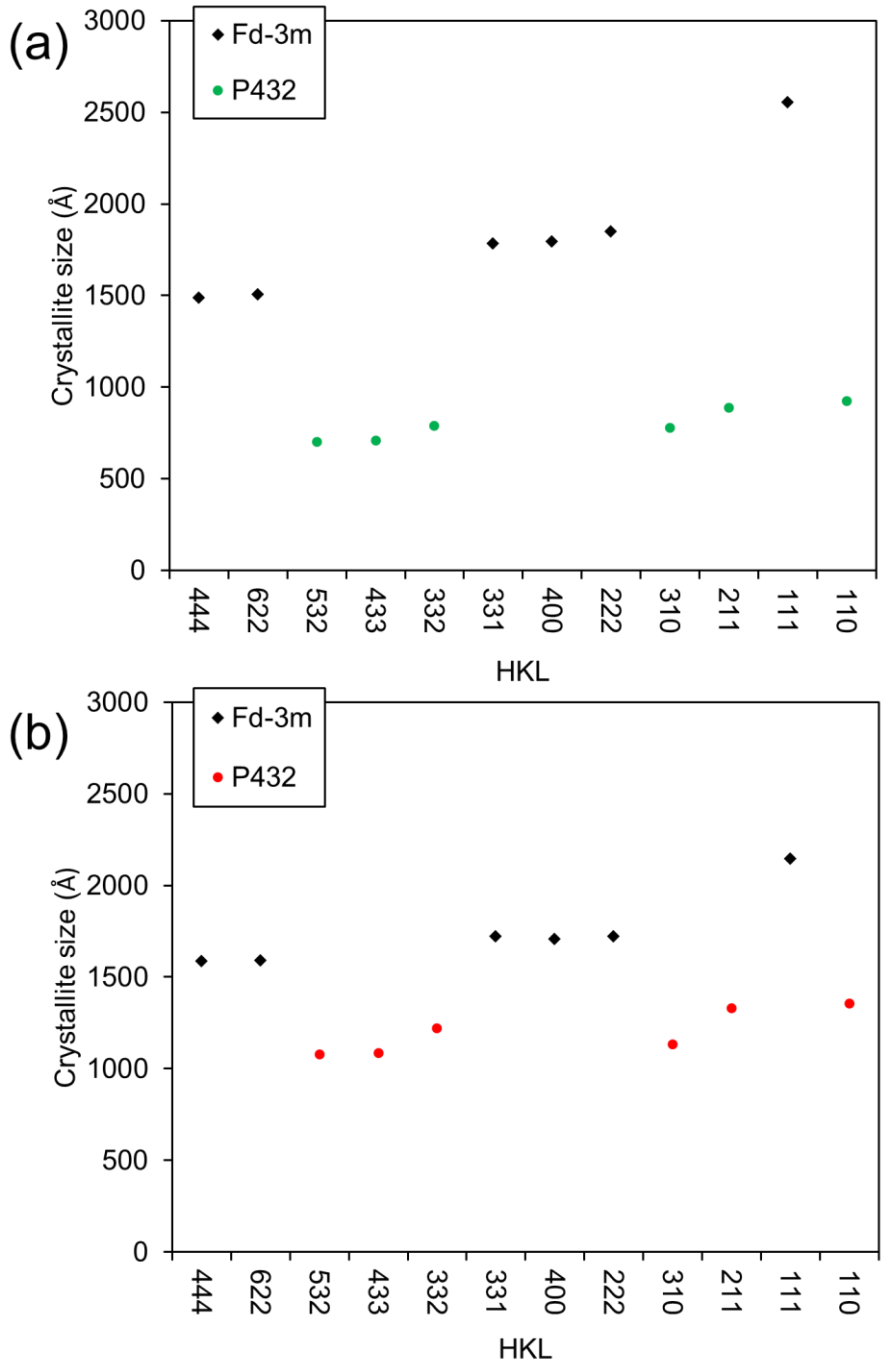

Figure B3 Instrument-broadening corrected FWHM for (a) A48 and (b) A240 from FullProf refinement data. The P4332 and Fd-3m peaks possess distinctly different broadening patterns.

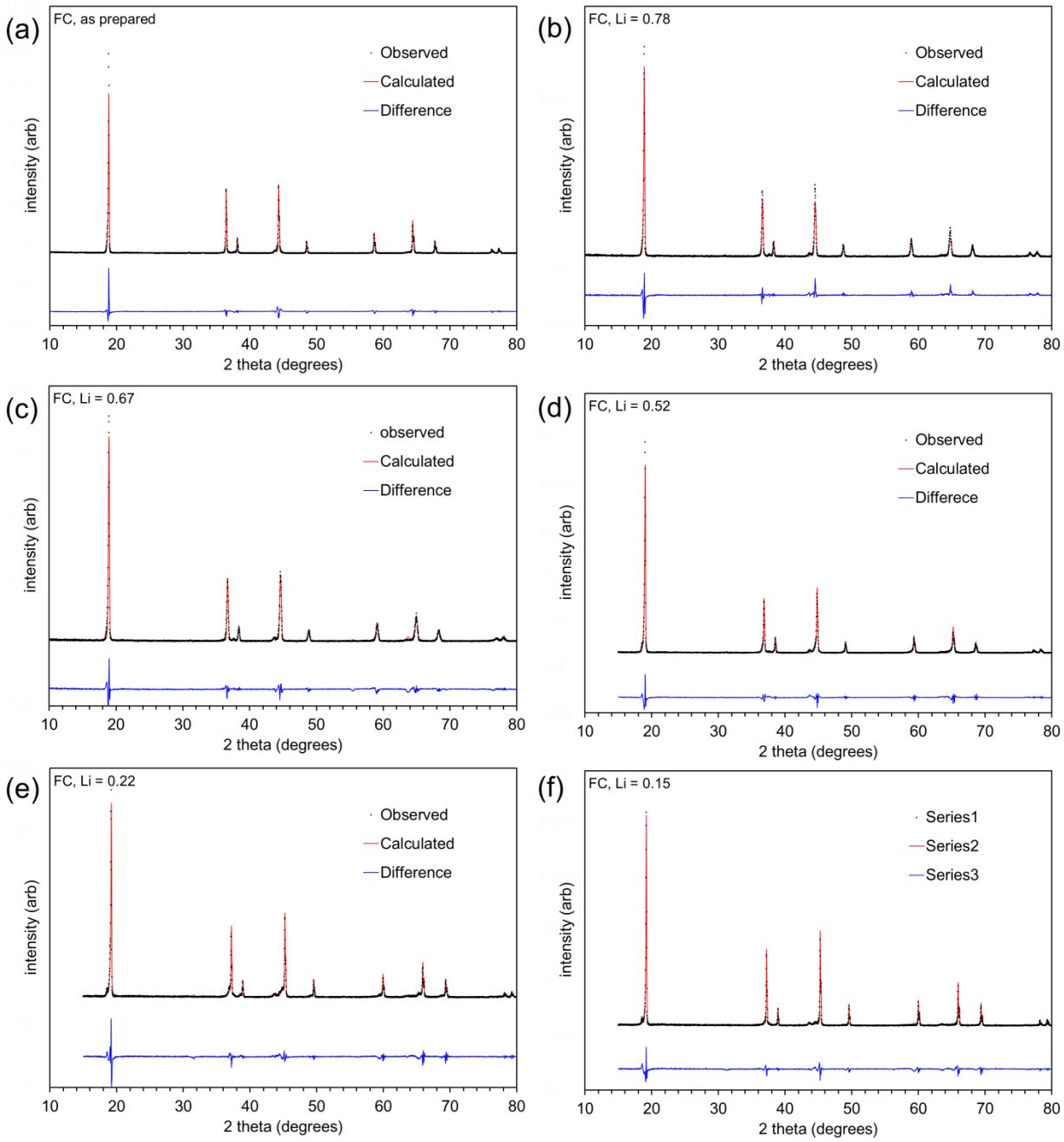

Figure B4 XRD Rietveld and LeBail refinement of delithiated FC spinels.

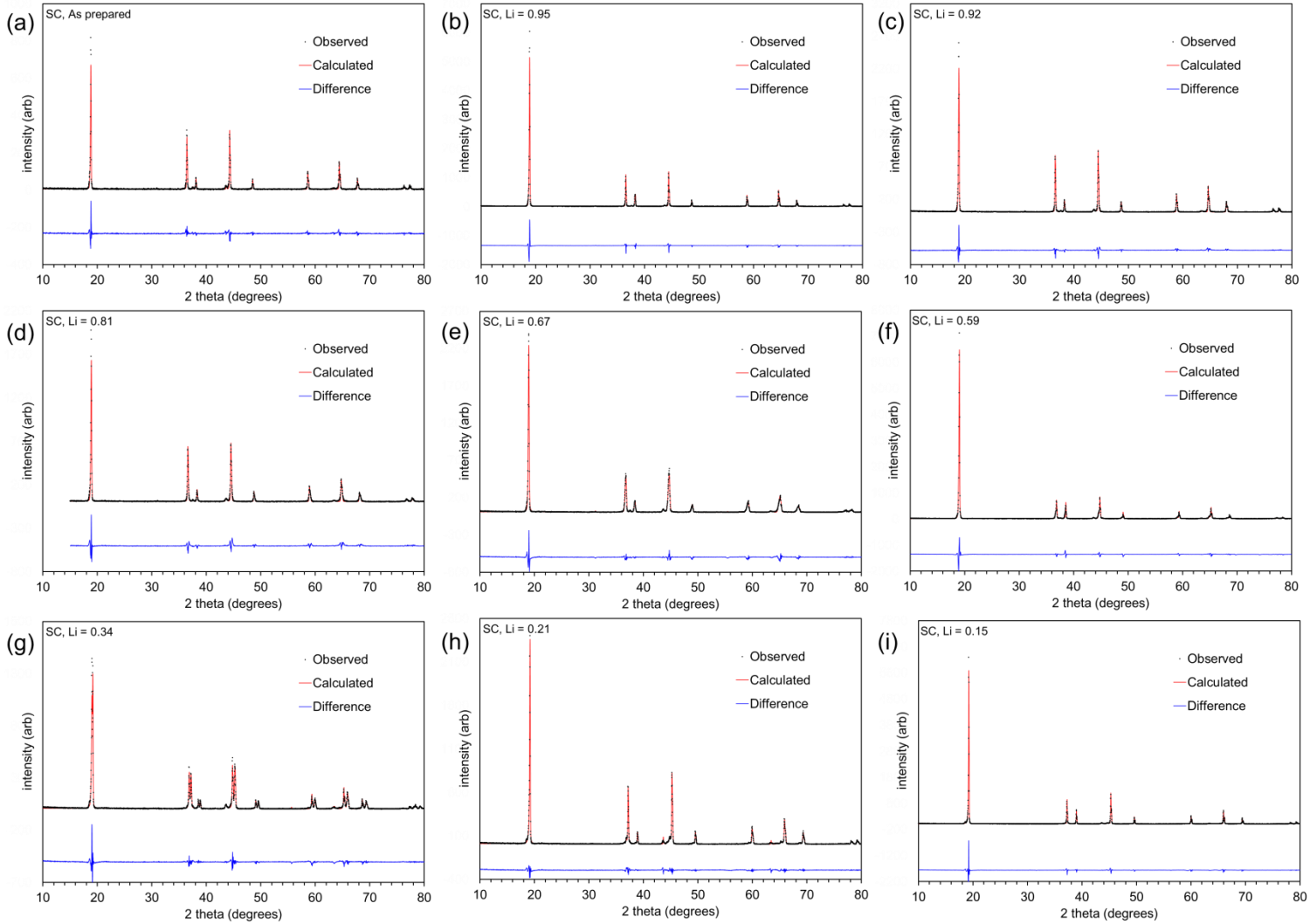

Figure B5 XRD Rietveld and LeBail refinement of delithiated SC spinels.

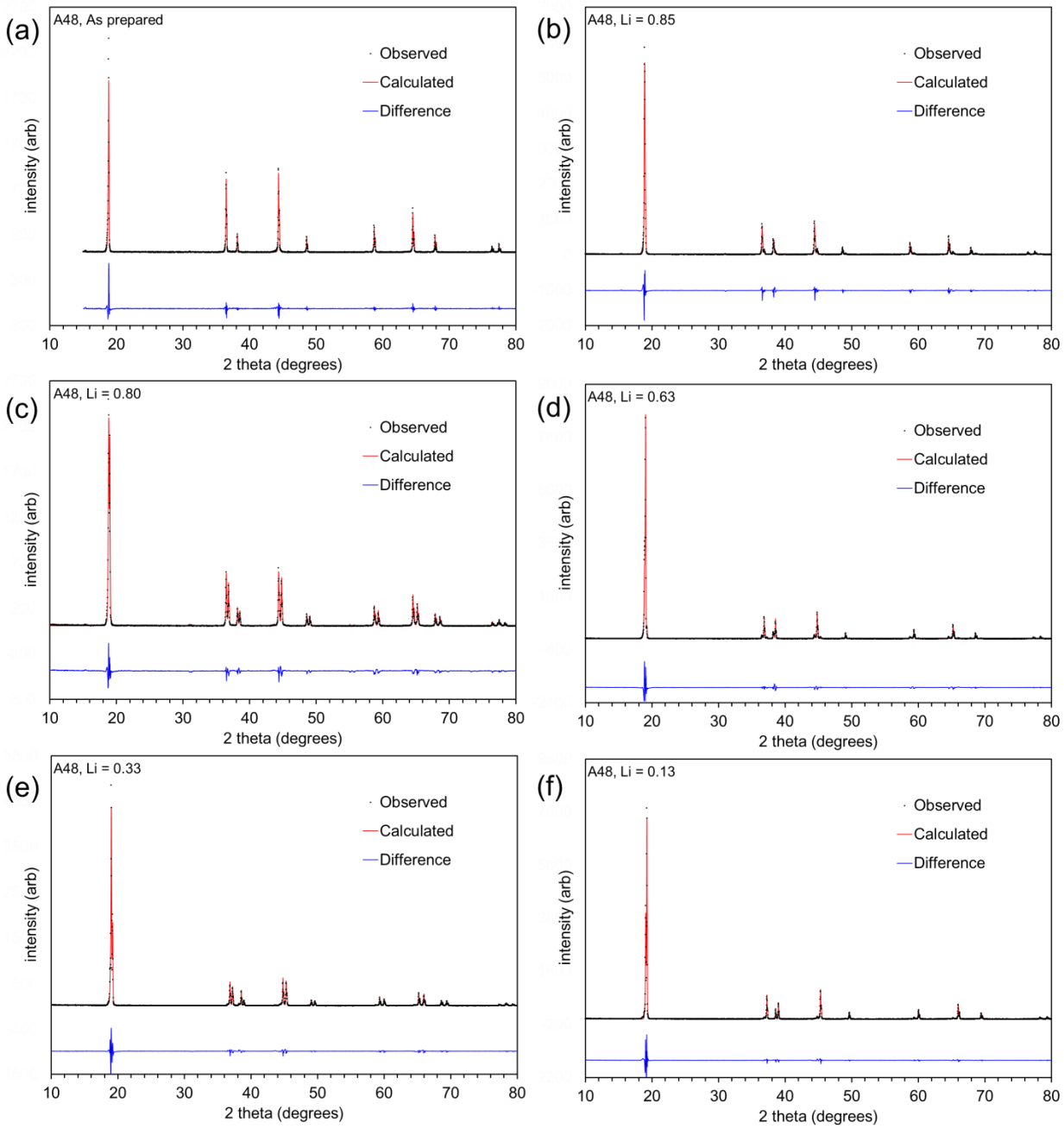

Figure B6 XRD Rietveld and LeBail refinement of delithiated A48 spinels.

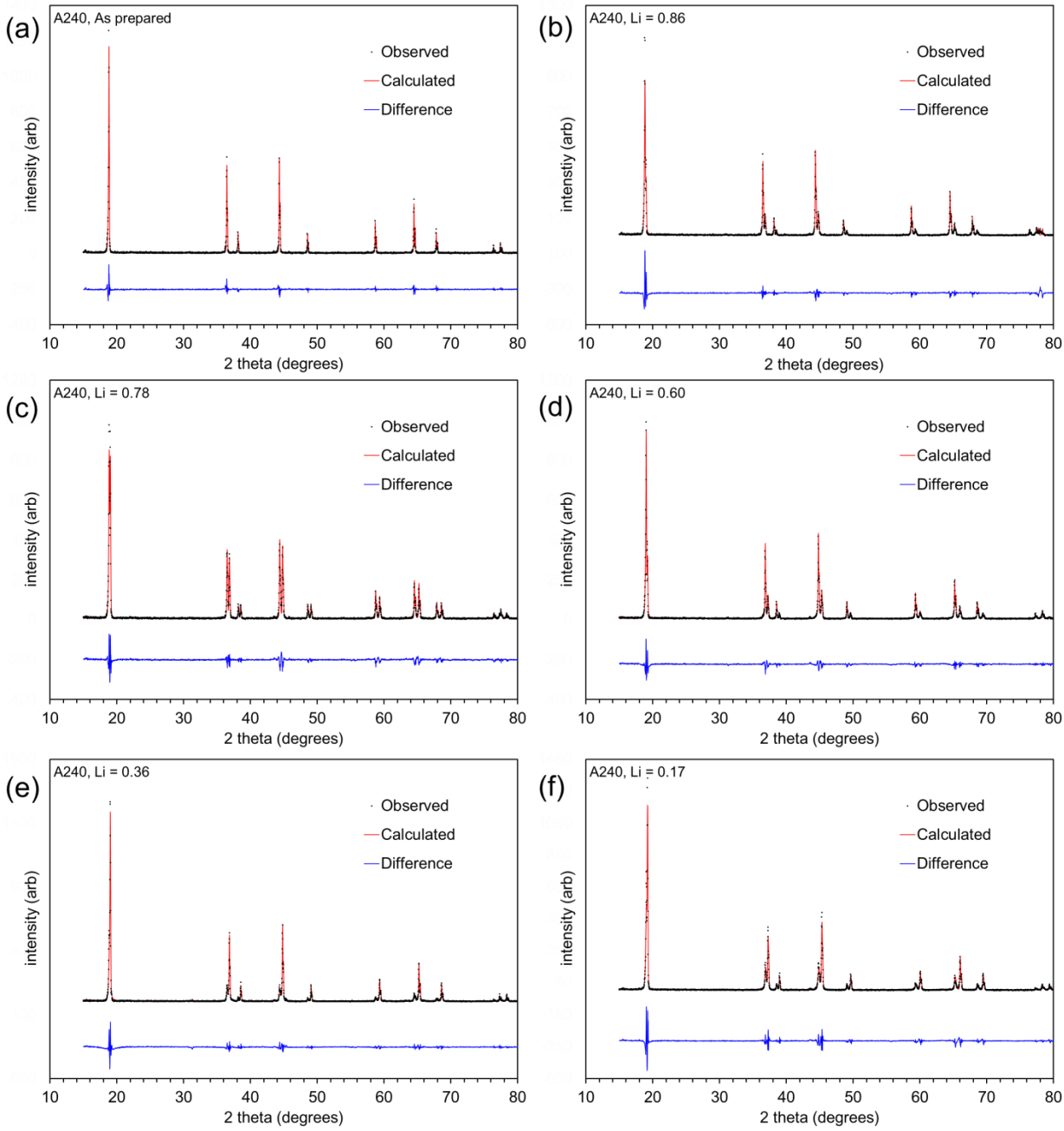

Figure B7 XRD Rietveld and LeBail refinement of delithiated A240 spinels.

Table B2 X-ray diffraction refinement parameters

Sample	Lithium content	Refinement type	χ^2	R_p
FC	As prepared	Rietveld	1.035	0.1718
	0.78	Rietveld	1.403	0.1957
	0.67	Von Dreele / LeBail	1.638	0.1888
	0.52	Von Dreele / LeBail	1.239	0.1744
	0.22	Von Dreele / LeBail	1.551	0.2001
	0.15	Von Dreele / LeBail	1.712	0.1952
SC	As prepared	Rietveld	0.6757	0.1993
	0.95	Von Dreele / LeBail	1.761	0.1825
	0.921	Rietveld	1.134	0.163
	0.81	Rietveld	1.511	0.1948
	0.67	Von Dreele / LeBail	1.431	0.167
	0.59	Von Dreele / LeBail	2.738	0.1852
	0.34	Von Dreele / LeBail	1.217	0.1621
	0.21	Von Dreele / LeBail	1.069	0.1329
	0.15	Von Dreele / LeBail	1.888	0.1739
A48	As prepared	Rietveld	1.008	0.1724
	0.85	Von Dreele / LeBail	2.137	0.1751
	0.8	Von Dreele / LeBail	1.684	0.1631
	0.63	Von Dreele / LeBail	2.26	0.1571
	0.332	Von Dreele / LeBail	1.218	0.1487
	0.133	Von Dreele / LeBail	2.123	0.161
A240	As prepared	Rietveld	0.7779	0.1786
	0.86	Von Dreele / LeBail	1.012	0.1856
	0.78	Von Dreele / LeBail	1.038	0.1784
	0.6	Von Dreele / LeBail	1.485	0.1896
	0.36	Von Dreele / LeBail	0.8347	0.1755
	0.17	Von Dreele / LeBail	0.9685	0.1855

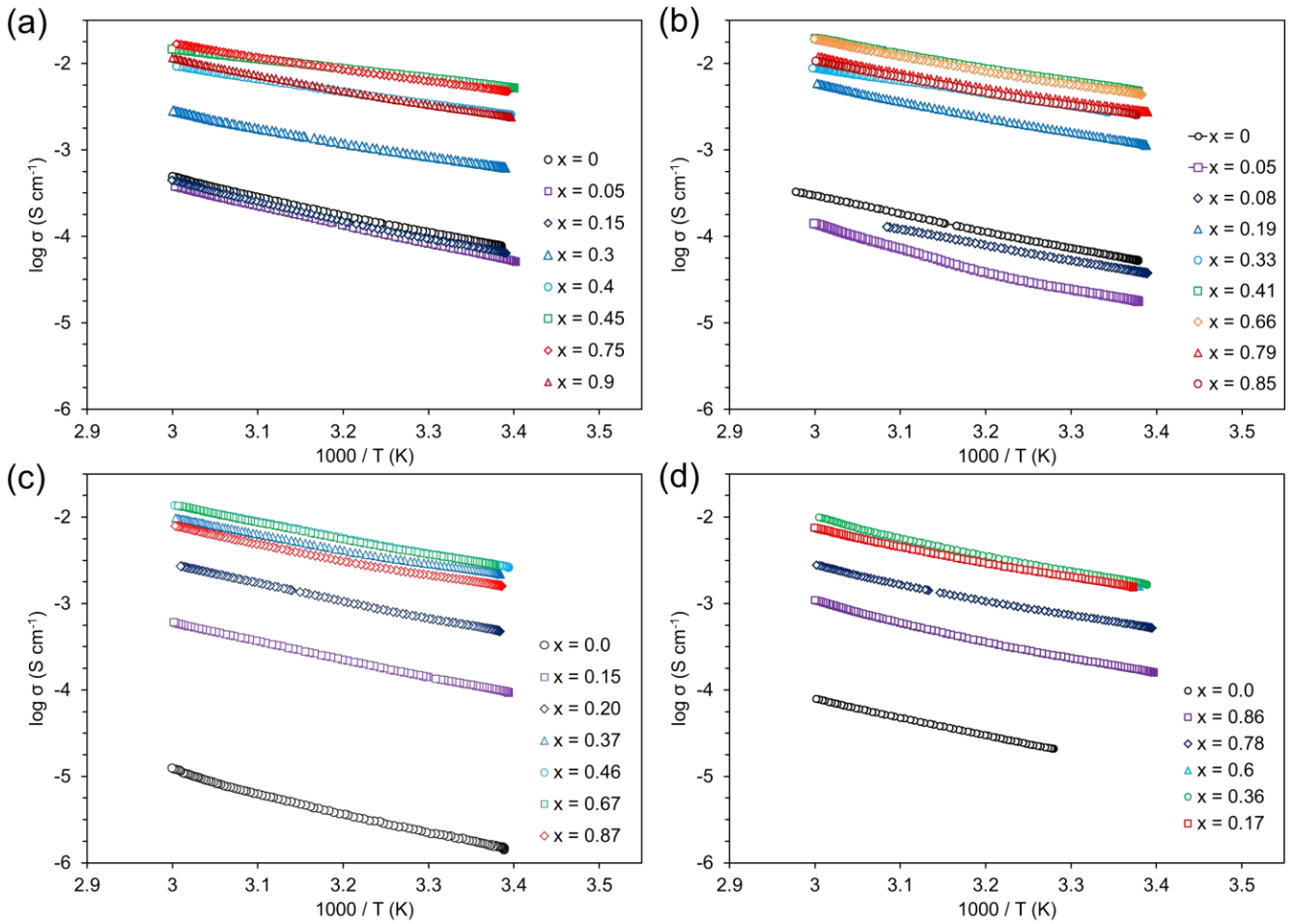

Figure B8 Arrhenius plots for as-prepared and delithiated (a) FC, (b) SC, (c) A48, and (d) A240 samples. The x corresponds to $Li_{1-x}Mn_{1.5}Ni_{0.5}O_4$.

Appendix C: Supporting Information for Chapter 6

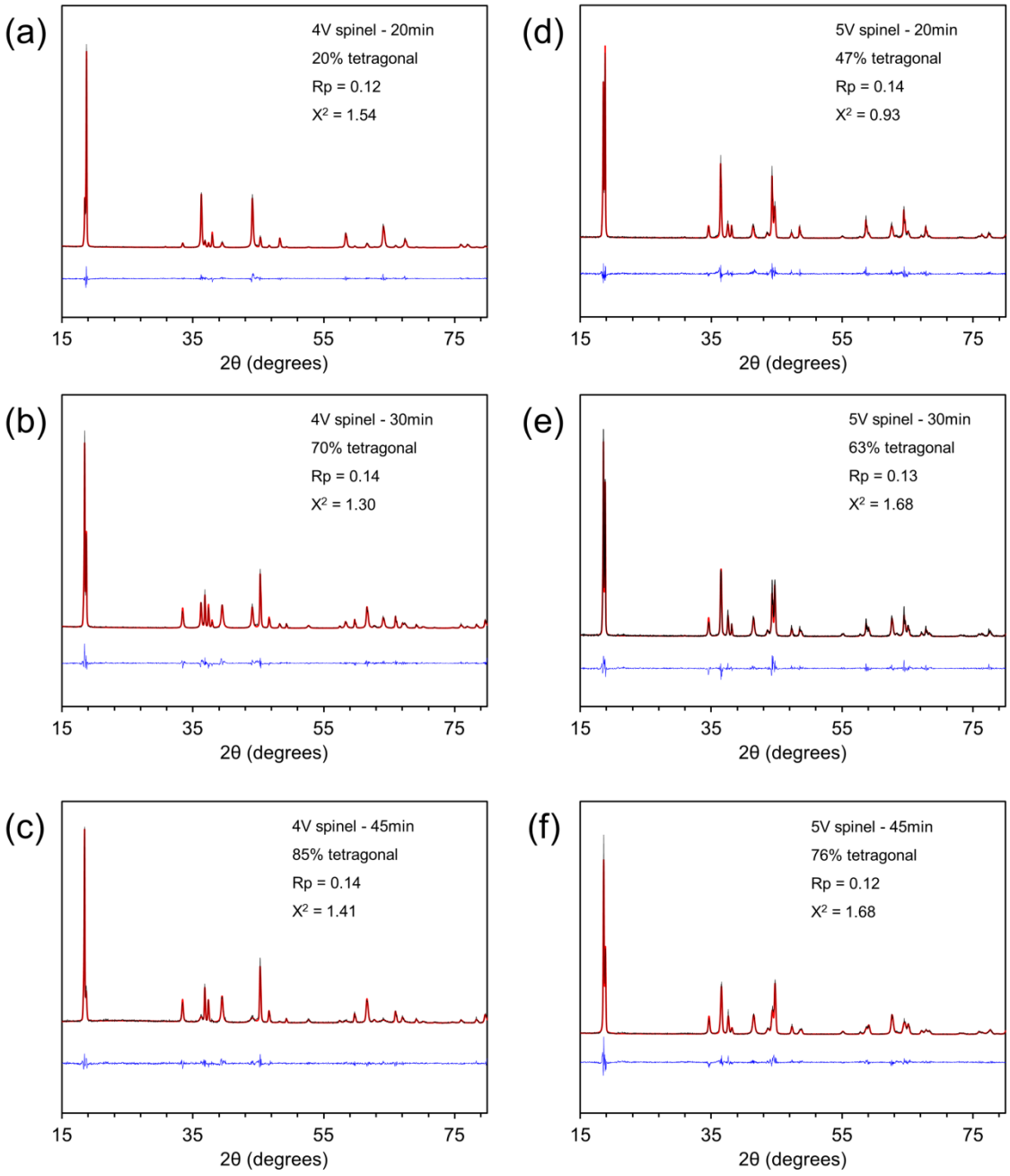

Figure C1 XRD Rietveld refinement of microwave-lithiated spinels.

References

(1) Gaines, L.; Cuenca, R. *Costs of Lithium-Ion Batteries for Vehicles*; 2000.

(2) Goodenough, J. B. *Energy & Environmental Science* **2013**, 14–18.

(3) Goodenough, J. B.; Kim, Y. *Journal of Power Sources* **2011**, *196*, 6688–6694.

(4) Manthiram, A. *The Journal of Physical Chemistry Letters* **2011**, *2*, 176–184.

(5) Scrosati, B.; Chimica, D.; La, R. *Journal of The Electrochemical Society* **1992**, *139*, 2776–2781.

(6) Guyomard, D.; Tarascon, J. M. *Journal of Power Sources* **1995**, *54*, 92–98.

(7) G. Bruce, P. *Chemical Communications* **1997**, *19*, 1817–1824.

(8) Thackeray, M. M.; Shao-horn, Y.; Kahaian, A. J.; Kepler, K. D.; Skinner, E.; Vaughey, J. T.; Hackney, S. A. *Electrochemical and Solid-State Letters* **1998**, *1*, 7–9.

(9) Goodenough, J. B.; Park, K. *Journal of the American Chemical Society* **2013**, *135*, 1167–1176.

(10) Doeff, M. M.; Hollingsworth, J.; Shim, J.; Lee, Y. J.; Striebel, K.; Reimer, J. A.; Cairns, E. J. *Journal of The Electrochemical Society* **2003**, *150*, A1060.

(11) Luo, Q.; Muraliganth, T.; Manthiram, A. *Solid State Ionics* **2009**, *180*, 703–707.

(12) Mizushima, K.; Jones, P. C.; Wiseman, P. J.; Goodenough, J. B. *Materials Research Bulletin* **1980**, *15*, 783–789.

(13) Thackeray, M. M.; David, W. I. F.; Bruce, P. G.; Goodenough, J. B. *Materials Research Bulletin* **1983**, *18*, 461–472.

(14) Padhi, A. K.; Nanjundaswamy, K. S.; Goodenough, J. B. *Journal of the Electrochemical Society* **1997**, *144*, 1188–1194.

(15) Yazami, R.; Touzain, P. *Journal of Power Sources* **1983**, *9*, 365–371.

(16) Monnierb, A. *Journal of the Electrochemical Society* **1998**, *145*, 428–436.

(17) Dimov, N.; Xia, Y.; Yoshio, M. *Journal of Power Sources* **2007**, *171*, 886–893.

(18) Kasavajjula, U.; Wang, C.; Appleby, A. J. *Journal of Power Sources* **2007**, *163*, 1003–1039.

(19) Dimov, N.; Kugino, S.; Yoshio, M. *Electrochimica Acta* **2003**, *48*, 1579–1587.

(20) Wang, G. X.; Bradhurst, D. H.; Dou, S. X.; Liu, H. K. *Journal of Power Sources* **1999**, *83*, 156–161.

(21) Jansen, A. .; Kahaian, A. .; Kepler, K. .; Nelson, P. .; Amine, K.; Dees, D. .; Vissers, D. .; Thackeray, M. . *Journal of Power Sources* **1999**, *81-82*, 902–905.

(22) Thackeray, M. M. *Journal of the Electrochemical Society* **1995**, *142*, 2558–2563.

(23) Woodford, W. H.; Chiang, Y.-M.; Carter, W. C. *Journal of the Electrochemical Society* **2013**, *160*, A1286–A1292.

(24) Tarascon, J. M.; Guyomard, D. *Journal of The Electrochemical Society* **1991**, *138*, 2864–2868.

(25) Moorhead-Rosenberg, Z.; Allcorn, E.; Manthiram, A. *Chemistry of Materials* **2014**, *26*, 5905–5913.

(26) Amine, K.; Tukamoto, H.; Yasuda, H.; Fuiita, Y. *Journal of The Electrochemical Society* **1996**, *143*, 1607–1613.

(27) Pasero, D.; Reeves, N.; Pralong, V.; West, A. R. *Journal of The Electrochemical Society* **2008**, *155*, A282.

(28) Manthiram, A.; Chemelewski, K.; Lee, E.-S. *Energy & Environmental Science* **2014**, *7*, 1339–1350.

(29) Moorhead-Rosenberg, Z.; Shin, D. W.; Chemelewski, K. R.; Goodenough, J. B.; Manthiram, A. *Applied Physics Letters* **2012**, *100*, 213909.

(30) Yang, L.; Ravdel, B.; Lucht, B. L. *Electrochemical and Solid-State Letters* **2010**, *13*, A95.

(31) Lu, D.; Xu, M.; Zhou, L.; Garsuch, a.; Lucht, B. L. *Journal of the Electrochemical Society* **2013**, *160*, A3138–A3143.

(32) Jang, D. H.; Oh, S. M. *Journal of the Electrochemical Society* **1997**, *144*, 3342–3348.

(33) Amine, K.; Liu, J.; Kang, S.; Belharouak, I.; Hyung, Y.; Vissers, D.; Henriksen, G. *Journal of Power Sources* **2004**, *129*, 14–19.

(34) Kim, J.-H.; Pieczonka, N. P. W.; Li, Z.; Wu, Y.; Harris, S.; Powell, B. R. *Electrochimica Acta* **2013**, *90*, 556–562.

(35) Wu, H. M.; Belharouak, I.; Deng, H.; Abouimrane, A.; Sun, Y.-K.; Amine, K. *Journal of The Electrochemical Society* **2009**, *156*, A1047–A1050.

(36) Jung, H.-G.; Jang, M. W.; Hassoun, J.; Sun, Y.-K.; Scrosati, B. *Nature Communications* **2011**, *2*, 1–5.

(37) Amdouni, N.; Zaghib, K.; Gendron, F.; Mauger, A.; Julien, C. M. *Ionics* **2006**, *12*, 117–126.

(38) Cabana, J.; Omenya, F. O.; Chernova, N. A.; Zeng, D.; Whittingham, M. S.; Grey, C. P. *Chemistry of Materials* **2012**, *24*, 2952–2964.

(39) Kim, J.-H.; Huq, A.; Chi, M.; Pieczonka, N. P. W.; Lee, E.; Bridges, C. A.; Tessema, M. M.; Manthiram, A.; Persson, K. A.; Powell, B. R. *Chemistry of Materials* **2014**, *25*, 4377–4386.

(40) Kunduraci, M.; Al-sharab, J. F.; Amatucci, G. G. *Chemistry of Materials* **2006**, *153*, 3585–3592.

(41) Mukai, K.; Sugiyama, J. *Journal of The Electrochemical Society* **2010**, *157*, A672.

(42) Moorhead-Rosenberg, Z.; Chemelewski, K. R.; Goodenough, J. B.; Manthiram, A. *Journal of Materials Chemistry A* **2013**, *1*, 10745–10752.

(43) Pasero, D.; Reeves, N.; Pralong, V.; West, A. R. *Journal of The Electrochemical Society* **2008**, *155*, A282.

(44) Wang, L.; Li, H.; Huang, X.; Baudrin, E. *Solid State Ionics* **2011**, *193*, 32–38.

(45) Herbst, J. F.; Croat, J. J. *Journal of Magnetism and Magnetic Materials* **1991**, *100*, 57–78.

(46) Walz, F. *Journal of Physics: Condensed Matter* **2002**, *14*, R285–R340.

(47) Goodenough, J. B. *Journal of Physics and Chemistry of Solids* **1958**, *6*, 287–297.

(48) Kanamori, J. *Journal of Physics and Chemistry of Solids* **1959**, *10*, 87–98.

(49) Kim, Y.; Hong, Y.; Kim, M. G.; Cho, J. *Electrochemistry Communications* **2007**, *9*, 1041–1046.

(50) Chemelewski, K. R.; Lee, E.-S.; Li, W.; Manthiram, A. *Chemistry of Materials* **2013**, *25*, 2890–2897.

(51) Roberts, B. A; Strauss, C. R. *Accounts of Chemical Research* **2005**, *38*, 653–61.

(52) Bilecka, I.; Niederberger, M. *Nanoscale* **2010**, *2*, 1358.

(53) Murugan, A. V.; Muraliganth, T.; Manthiram, A. *Journal of Physical Chemistry C* **2008**, *112*, 14665–14671.

(54) Murugan, A. V.; Muraliganth, T.; Ferreira, P. J.; Manthiram, A. *Inorganic Chemistry* **2009**, *48*, 946–952.

(55) Bridges, C. a.; Harrison, K. L.; Unocic, R. R.; Idrobo, J.-C.; Parans Paranthaman, M.; Manthiram, A. *Journal of Solid State Chemistry* **2013**, *205*, 197–204.

(56) Bilecka, I.; Niederberger, M. *Nanoscale* **2010**, *2*, 1358.

(57) Poul, L.; Ammar, S.; Jouini, N.; Fievet, F.; Chimie, L. De *Journal of Sol-Gel Science and Technology* **2003**, *26*, 261–265.

(58) Feldmann, C. *Advanced Functional Materials* **2003**, *13*, 101–107.

(59) Tüysüz, H.; Liu, Y.; Weidenthaler, C.; Schüth, F. *Journal of the American Chemical Society* **2008**, *130*, 14108–10.

(60) Sinha, N. N.; Munichandraiah, N. *Journal of The Electrochemical Society* **2010**, *157*, A824.

(61) Kim, J.-S.; Kim, K.; Cho, W.; Shin, W. H.; Kanno, R.; Choi, J. W. *Nano Letters* **2012**, *12*, 6358–65.

(62) Chen, Z.; Zhao, R.; Du, P.; Hu, H.; Wang, T.; Zhu, L.; Chen, H. *Journal of Materials Chemistry A* **2014**.

(63) Xiao, J.; Chen, X.; Sushko, P. V.; Sushko, M. L.; Kovarik, L.; Feng, J.; Deng, Z.; Zheng, J.; Graff, G. L.; Nie, Z.; Choi, D.; Liu, J.; Zhang, J.-G.; Whittingham, M. S. *Advanced Materials* **2012**, *24*, 2109–2116.

(64) Goodenough, J. B.; Kim, Y. *Chemistry of Materials* **2010**, *22*, 587–603.

(65) Nakamura, T.; Yamada, Y.; Tabuchi, M. *Journal of Applied Physics* **2005**, *98*, 093905.

(66) Hwang, B. J.; Wu, Y. W.; Venkateswarlu, M.; Cheng, M. Y.; Santhanam, R. *Journal of Power Sources* **2009**, *193*, 828–833.

(67) Kim, J.; Myung, S.; Yoon, C. S.; Kang, S. G.; Sun, Y. *Chemistry of Materials* **2004**, *16*, 906–914.

(68) Ohzuku, T.; Ariyoshi, K.; Yamamoto, S. *Journal of the Ceramic Society of Japan* **2002**, *110*, 501–505.

(69) Arunkumar, T. A.; Manthiram, A. *Electrochemical and Solid-State Letters* **2005**, *8*, A403.

(70) Shin, D. W.; Manthiram, A. *Electrochemistry Communications* **2011**, *13*, 1213–1216.

(71) Strobel, P.; Palos, A. I.; Anne, M.; Cras, F. Le *Journal of Materials Chemistry* **2000**, *10*, 429–436.

(72) Greedan, J. E.; Raju, N. P.; Wills, A. S.; Morin, C.; Shaw, S. M. *Chemistry of Materials* **1998**, *10*, 3058–3067.

(73) Dutta, G.; Manthiram, A.; Goodenough, J. B.; Grenier, J.-C. *Journal of Solid State Chemistry* **1992**, *96*, 123–131.

(74) Amdouni, N.; Zaghib, K.; Gendron, F.; Mauger, a.; Julien, C. M. *Journal of Magnetism and Magnetic Materials* **2007**, *309*, 100–105.

(75) Biškup, N.; Martínez, J. L.; Arroyo y de Dompablo, M. E.; Díaz-Carrasco, P.; Morales, J. *Journal of Applied Physics* **2006**, *100*, 093908.

(76) Wills, A. S.; Raju, N. P.; Greedan, J. E. *Chemistry of Materials* **1999**, *11*, 1510–1518.

(77) Azzoni, C.; Paleari, a; Massarotti, V.; Bini, M.; Capsoni, D. *Physical Review. B, Condensed Matter* **1996**, *53*, 703–709.

(78) Bajpai, A.; Banerjee, A. *Physical Review B* **1997**, *55*, 439–445.

(79) Makhlouf, S. a.; Parker, F. T.; Spada, F. E.; Berkowitz, a. E. *Journal of Applied Physics* **1997**, *81*, 5561.

(80) Thackeray, M. M.; Wolverton, C.; Isaacs, E. D. *Energy & Environmental Science* **2012**, *5*, 7854.

(81) Zheng, J.; Xiao, J.; Yu, X.; Kovarik, L.; Gu, M.; Omenya, F.; Chen, X.; Yang, X.-Q.; Liu, J.; Graff, G. L.; Whittingham, M. S.; Zhang, J.-G. *Physical Chemistry Chemical Physics : PCCP* **2012**, *14*, 13515–13521.

(82) Shin, D. W.; Bridges, C. A.; Huq, A.; Paranthaman, M. P.; Manthiram, A. *Chemistry of Materials* **2012**, *24*, 3720–3731.

(83) Chemelewski, K. R.; Shin, D. W.; Li, W.; Manthiram, A. *Journal of Materials Chemistry A* **2013**, *1*, 3347–3354.

(84) Patoux, S.; Sannier, L.; Lignier, H.; Reynier, Y.; Bourbon, C.; Jouanneau, S.; Le Cras, F.; Martinet, S. *Electrochimica Acta* **2008**, *53*, 4137–4145.

(85) Zhong, G. B.; Wang, Y. Y.; Zhao, X. J.; Wang, Q. S.; Yu, Y.; Chen, C. H. *Journal of Power Sources* **2012**, *216*, 368.

(86) Molenda, J. *Solid State Ionics* **2004**, *171*, 215–227.

(87) Liu, J.; Manthiram, A. *Journal of Physical Chemistry C* **2009**, *113*, 15073–15079.

(88) Kadoma, Y.; Sato, S.; Ui, K.; Kumagai, N. *Electrochemistry* **2010**, *8*, 658.

(89) Song, J.; Shin, D. W.; Lu, Y.; Amos, C. D.; Manthiram, A.; Goodenough, J. B. *Chemistry of Materials* **2012**, *24*, 3103.

(90) Kawai, N.; Nakamura, T.; Yamada, Y.; Tabuchi, M. *Journal of Power Sources* **2011**, *196*, 6969–6973.

(91) Ariyoshi, K.; Iwakoshi, Y.; Nakayama, N.; Ohzuku, T. *Journal of The Electrochemical Society* **2004**, *151*, A296.

(92) Lee, E.; Nam, K.; Hu, E.; Manthiram, A. *Chemistry of Materials* **2012**, *24*, 3610.

(93) Lee, E.-S.; Manthiram, A. *Journal of Materials Chemistry A* **2013**, *1*, 3118.

(94) Paulsen, J. A.; Lo, C. C. H.; Snyder, J. E.; Member, S.; Ring, A. P.; Jones, L. L.; Jiles, D. C. *IEEE Transaction on Magnetics* **2003**, *39*, 3316–3318.

(95) Wiebe, C. R.; Russo, P. L.; Savici, a T.; Uemura, Y. J.; MacDougall, G. J.; Luke, G. M.; Kuchta, S.; Greedan, J. E. *Journal of Physics: Condensed Matter* **2005**, *17*, 6469–6482.

(96) Yang, J.; Han, X.; Zhang, X.; Cheng, F.; Chen, J. *Nano Research* **2013**, *6*, 679–687.

(97) Xiao, J.; Yu, X.; Zheng, J.; Zhou, Y.; Gao, F.; Chen, X.; Bai, J.; Yang, X.-Q.; Zhang, J.-G. *Journal of Power Sources* **2013**, *242*, 736–741.

(98) Lee, E.; Persson, K. A. *Chemistry of Materials* **2013**, *25*, 2885–2889.

(99) Kunduraci, M.; Amatucci, G. G. *Journal of The Electrochemical Society* **2006**, *153*, A1345.

(100) Duncan, H.; Hai, B.; Leskes, M.; Grey, C. P.; Chen, G. *Chemistry of Materials* **2014**, *26*, 5374.

(101) Saravanan, K.; Jarry, A.; Kostecki, R.; Chen, G. *Scientific Reports* **2015**, *5*, 8027.

(102) Ransil, A. P. Electronic Transport in Lithium Nickel Manganese Oxide, a High-Voltage Cathode Material for Lithium-Ion Batteries, 2013.

(103) Chemelewski, K. R.; Li, W.; Gutierrez, A.; Manthiram, A. *Journal of Materials Chemistry A* **2013**, *1*, 15334–15341.

(104) Clarke, P. S.; Orton, J. W.; Guest, A. J. *Physical Review B* **1978**, *18*, 1813–1817.

(105) Wang, R.; Sleight, A. W.; Cleary, D. *Chemistry of Materials* **1996**, *8*, 433–439.

(106) Maier, J.; Festko, M. *Journal of the European Ceramic Society* **1999**, *19*, 675–681.

(107) Fleig, J. *Solid State Ionics* **2002**, *150*, 181–193.

(108) Delmas, C.; Maccario, M.; Croguennec, L.; Le Cras, F.; Weill, F. *Nature Materials* **2008**, *7*, 665–71.

(109) Liu, H.; Strobridge, F. C.; Borkiewicz, O. J.; Wiaderek, K. M.; Chapman, K. W.; Chupas, P. J.; Grey, C. P. *Science* **2014**, *344*, 1480.

(110) Padhi, A. K.; Nanjundaswamy, K. S.; Goodenough, J. B. *Journal of The Electrochemical Society* **1997**, *144*, 1188–1194.

(111) Xu, X. Q.; Peng, J. L.; Li, Z. Y.; Ju, H. L.; Greene, R. L. *Physical Review B* **1993**, *48*, 1112–1118.

(112) Marzec, J.; Swierczek, K.; Przewoznik, J.; Molenda, J.; Simon, D. R.; Kelder, E. M.; Schoonman, J. *Solid State Ionics* **2002**, *146*, 225–237.

(113) Tateishi, K.; du Boulay, D.; Ishizawa, N. *Applied Physics Letters* **2004**, *84*, 529.

(114) Iguchi, E.; Nakamura, N.; Aoki, a. *Philosophical Magazine Part B* **1998**, *78*, 65–77.

(115) Iguchi, E.; Tokuda, Y.; Nakatsugawa, H.; Munakata, F. *Journal of Applied Physics* **2002**, *91*, 2149–2153.

(116) Austin, I. G.; Mott, N. F. *Advances in Physics* **2001**, *50*, 757–812.

(117) Emin, D. *Physics Today* **1982**, *35*, 34.

(118) Ouyang, C.; Du, Y.; Shi, S.; Lei, M. *Physics Letters A* **2009**, *373*, 2796–2799.

(119) Kunduraci, M.; Amatucci, G. G. *Electrochimica Acta* **2008**, *53*, 4193–4199.

(120) Jin, Y.-C.; Lin, C.-Y.; Duh, J.-G. *Electrochimica Acta* **2012**, *69*, 45–50.

(121) Jafta, C. J.; Mathe, M. K.; Manyala, N.; Roos, W. D.; Ozoemena, K. I. *Applied Materials & Interfaces* **2013**, 7592–7598.

(122) Lu, L.; Han, X.; Li, J.; Hua, J.; Ouyang, M. *Journal of Power Sources* **2013**, *226*, 272–288.

(123) Nishi, Y.; Azuma, H.; Omaru, A. Non Aqueous Electrolyte Cell **1990**.

(124) Buqa, H.; Goers, D.; Holzapfel, M.; Spahr, M. E.; Novák, P. *Journal of The Electrochemical Society* **2005**, *152*, A474–A481.

(125) Goodenough, J. B. *Energy & Environmental Science* **2014**, *7*, 14–18.

(126) Zaghib, K.; Mauger, A.; Groult, H.; Goodenough, J.; Julien, C. *Materials* **2013**, *6*, 1028–1049.

(127) Poizot, P.; Laruelle, S.; Grugeon, S.; Dupont, L.; Tarascon, J. M. *Nature* **2000**, *407*, 496–9.

(128) Pfanzelt, M.; Kubiak, P.; Fleischhammer, M.; Wohlfahrt-Mehrens, M. *Journal of Power Sources* **2011**, *196*, 6815–6821.

(129) Deng, D.; Kim, M. G.; Lee, J. Y.; Cho, J. *Energy & Environmental Science* **2009**, *2*, 818–837.

(130) Ferg, E.; Gummow, R. J.; Kock, A. De; Thackeray, M. *Journal of The Electrochemical Society* **1994**, *141*, L147–L150.

(131) Wachtler, M.; Besenhard, J. O.; Winter, M. *Journal of Power Sources* **2001**, *94*, 189–193.

(132) Fransson, L. M. L.; Vaughey, J. T.; Benedek, R.; Edstrom, K.; Thomas, J. O.; Thackeray, M. M. *Electrochemistry Communications* **2001**, *3*, 317–323.

(133) Applestone, D.; Yoon, S.; Manthiram, A. *Journal of Materials Chemistry* **2012**, *22*, 3242.

(134) Allcorn, E.; Manthiram, A. *Journal of Physical Chemistry C* **2014**, *118*, 811–822.

(135) Yoon, S.; Manthiram, A. *Journal of Materials Chemistry* **2010**, *20*, 236–239.

(136) Yoon, S.; Manthiram, A. *Electrochemical and Solid-State Letters* **2009**, *12*, A190.

(137) Zhang, W.-J. *Journal of Power Sources* **2011**, *196*, 13–24.

(138) Brutti, S.; Gentili, V.; Reale, P.; Carbone, L.; Panero, S. *Journal of Power Sources* **2011**, *196*, 9792–9799.

(139) Fridman, K.; Sharabi, R.; Elazari, R.; Gershinsky, G.; Markevich, E.; Salitra, G.; Aurbach, D. *Electrochemistry Communications* **2013**, *33*, 31–34.

(140) Manthiram, A.; Chemelewski, K.; Lee, E.-S. *Energy & Environmental Science* **2014**, *7*, 1339–1350.

(141) Peramunage, D.; Abraham, K. M. *Journal of The Electrochemical Society* **1998**, *145*, 1131–1136.

(142) Koksbang, R. Method Of Making Lithium-Vanadium-Oxide Active Material **1996**.

(143) Bourbon, C.; LeCras, F.; Rouppert, F.; Bloch, D. Process For Preparation Ofa Lithiated Or Overlithiated Transition Metal Oxide, Active Positive Electrode Materials Containing This Oxide, And A Battery **2003**, *1*.

(144) Brousseley, M. In *Lithium Batteries: Science and Technology*; Nazri, G. A.; Pistoria, G., Eds.; Springer: New York, 2003; p. 649.

(145) Sun, Y.; Jeon, Y. *Journal of Materials Chemistry* **1999**, *9*, 3147–3150.

(146) Kang, S.; Goodenough, J. B.; Rabenberg, L. K. *Chemistry of Materials* **2001**, *13*, 1758–1764.

(147) Besenhard, J. O.; Yang, J.; Winter, M. *Journal of Power Sources* **1997**, *68*, 87–90.

(148) Hai, B.; Shukla, A. K.; Duncan, H.; Chen, G. *Journal of Materials Chemistry A* **2013**, *1*, 759–769.

(149) Moorhead-Rosenberg, Z.; Harrison, K. L.; Turner, T.; Manthiram, A. *Inorganic Chemistry* **2013**, *52*, 13087–13093.

(150) Kuo, H. T.; Bagkar, N. C.; Liu, R. S.; Shen, C. H.; Shy, D. S.; Xing, X. K.; Lee, J.-F.; Chen, J. M. *Journal of Physical Chemistry B* **2008**, *112*, 11250–11257.

(151) Allcorn, E.; Manthiram, A. *Journal of Materials Chemistry A* **2015**, *3*, 3891–3900.

(152) Smart, M. C.; Ratnakumar, B. V; Surampudi, S. *Journal of The Electrochemical Society* **1999**, *146*, 486–492.

(153) Inaba, M.; Siroma, Z.; Kawatate, Y.; Funabiki, A.; Ogumi, Z. *Journal of Power Sources* **1997**, *68*, 221–226.

(154) Lee, H.; Choi, S.; Choi, S.; Kim, H.-J.; Choi, Y.; Yoon, S.; Cho, J.-J. *Electrochemistry Communications* **2007**, *9*, 801–806.

(155) Chong, J.; Xun, S.; Zhang, J.; Song, X.; Xie, H.; Battaglia, V.; Wang, R. *Chemistry, a European Journal* **2014**, *20*, 7479–7485.

(156) Arbizzani, C.; De Giorgio, F.; Mastragostino, M. *Journal of Power Sources* **2014**, *266*, 170–174.

(157) Aklalouch, M.; Rojas, R. M.; Rojo, J. M.; Saadoune, I.; Amarilla, J. M. *Electrochimica Acta* **2009**, *54*, 7542–7550.

(158) Poliakoff, M.; Fitzpatrick, J. M.; Farren, T. R.; Anastas, P. T. *Science* **2002**, *297*, 807–10.

(159) Manthiram, A.; Dananjay, A.; Zhu, Y. T. *Chemistry of Materials* **1994**, *6*, 1601–1602.

(160) Chandler, C. D.; Roger, C.; Hampden-smith, M. J. *Chemical Review* **1993**, *93*, 1205–1241.

(161) He, W.; Zhang, Y.; Zhang, X.; Wang, H.; Yan, H. *Journal of Crystal Growth* **2003**, *252*, 285–288.

(162) Kou, J.; Bennett-stamper, C.; Varma, R. S. *Sustainable Chemistry & Engineering* **2013**, *1*, 810–816.

(163) Polshettiwar, V.; Nadagouda, M. N.; Varma, R. S. *Australian Journal of Chemistry* **2009**, *62*, 16.

(164) Zhu, X. H.; Hang, Q. M. *Micron* **2012**, *44*, 21–44.

(165) Zhao, Y.; Zhu, J.-J.; Hong, J.-M.; Bian, N.; Chen, H.-Y. *European Journal of Inorganic Chemistry* **2004**, *20*, 4072–4080.

(166) Kawasaki, H.; Kosaka, Y.; Myoujin, Y.; Narushima, T.; Yonezawa, T.; Arakawa, R. *Chemical Communications* **2011**, *47*, 7740–7742.

(167) Komarneni, S.; Pidugu, R.; Li, Q. H.; Roy, R. *Journal of Materials Research* **2000**, *10*, 1687–1692.

(168) Komarneni, S. *Current Science* **2003**, *85*, 1730–1734.

(169) Blosi, M.; Albonetti, S.; Dondi, M.; Martelli, C.; Baldi, G. *Journal of Nanoparticle Research* **2010**, *13*, 127–138.

(170) Blakely, C. K.; Bruno, S. R.; Poltavets, V. V *Inorganic Chemistry* **2011**, *50*, 6696–700.

(171) Gayathri, N.; Raychaudhuri, A. K.; Xu, X. Q.; Peng, J. L.; Greene, R. L. *Journal of Physics: Condensed Matter* **1998**, *10*, 1323–1338.

(172) Gopalan, P.; McElfresh, M. W.; Kakol, Z.; Spalek, J.; Honig, J. M. *Physical Review B* **1992**, *45*, 249–255.

(173) Lebon, A.; Adler, P.; Bernhard, C.; Boris, A.; Pimenov, A.; Maljuk, A.; Lin, C.; Ulrich, C.; Keimer, B. *Physical Review Letters* **2004**, *92*, 037202.

(174) Diodati, S.; Nodari, L.; Natile, M. M.; Russo, U.; Tondello, E.; Lutterotti, L.; Gross, S. *Dalton transactions (Cambridge, England : 2003)* **2012**, *41*, 5517–25.

(175) Manthiram, A.; Tang, J. P.; Manivannan, V. *Journal of Solid State Chemistry* **1999**, *148*, 499–507.

(176) Yamazaki, S.; Li, C.; Ohoyama, K.; Nishi, M.; Ichihara, M.; Ueda, H.; Ueda, Y. *Journal of Solid State Chemistry* **2010**, *183*, 1496–1503.

(177) Theobald, F.; Cabala, R.; Bernard, J. *C.R. Academy of Sciences Paris, Ser.C* **1969**, *269*, 1209–1212.

(178) Tilley, R. J.; Hyde, B. J. *Journal of Physical Chemistry of Solids* **1970**, *31*, 1613–1619.

(179) Grymonprez, G.; Fiermans, L.; Vennik, J. *Acta Crystallographica* **1977**, *A33*, 834–837.

(180) Tichy, R. S.; Goodenough, J. B. *Solid State Sciences* **2002**, *4*, 661–664.

(181) Stølen, S.; Bakken, E.; Mohn, C. E. *Physical Chemistry Chemical Physics : PCCP* **2006**, *8*, 429–47.

(182) Hansteen, O. H.; Fjellvag, H.; Hauback, B. C. *Journal of Materials Chemistry* **1998**, *8*, 2081–2088.

(183) Carvalho, M. D.; Cruz, M. M.; Wattiaux, A.; Bassat, J. M.; Costa, F. M. A.; Godinho, M. *Journal of Applied Physics* **2000**, *88*, 544.